School of Mathematics, Computer Science and Engineering
Department of Mechanical Engineering and Aeronautics

Development of a Micro Gas Turbine for Concentrated Solar Power Applications

Mahmoud Khader

Submitted for the degree of Doctor of Philosophy
City, University of London
July 2017

Declaration

I hereby declare that, I'm the soul author of this thesis and the work presented in it is original. This thesis has not been and will not be submitted in whole or in part to another University for the award of any other degree.

Signature:

Mahmoud Khader

Abstract

The main objective of this research is to enhance the performance of a solar powered Micro Gas Turbine (MGT) by exploring suitable methods to be applied to the turbomachinery components to increase their efficiency and improve the predictability of their performance over the operating range of the MGT.

A novel idea of reducing turbine rotor friction losses through adding riblets to the rotor hub was explored thoroughly. Computational Fluid Dynamics (CFD) has been used to study the effects of those features at design point conditions of the MGT. Riblets with different height and spacing have been examined to determine the riblet geometry where the maximum drag reduction is achieved. To improve the predictability of performance of the turbomachinery components of the MGT over the operating envelope, a prediction methodology was developed during this research which used a combination of CFD and empirical correlations to account for losses that are not included in the CFD model.

It was found that riblets reduce the cross-stream motion of the low momentum fluid flow near the hub surface of the rotor passage, and separate the streamwise vortex from interaction with the hub surface. The maximum drag reduction was found to occur with riblets of a relative height of 2.5% with respect to the rotor inlet blade height.

The performance prediction method was successfully applied to a radial turbine and centrifugal compressor designed for a 6 kWe solar powered MGT. A purpose-built test rig was built and the actual performance map for the turbine was achieved while running it using warm compressed air from an external air supply. The comparison between the actual and the predicted data revealed a good match between both results, which indicates the validity of the demonstrated performance prediction method.

Acknowledgements

Table of Contents

List of figures

List of tables

Nomenclature:

A	Area
b	Rotor inlet blade height
C	Flow absolute velocity, Chord length
Cl	Tip clearance at rotor inlet.
c_p	Specific heat at constant pressure for air
D	Diameter
h_v	Nozzle guide vane height
h	Enthalpy
Ig	Interspace geometry parameter
$\dot{m}$	Mass flow rate
N_s	Specific speed
N_b	Number of rotor blades
N_{gv}	Number of nozzle guide vanes
P	Pressure
PR	Pressure ratio
$\dot{Q}$	Rotor outlet volume flow rate
R	Universal gas constant, Radius
Re	Reynolds number
S_v	Guide vanes pitch
T	Temperature
t	Thickness
U	Blade speed
W	Flow relative velocity
$\dot{W}$	Specific power
Z	Rotor or impeller axial length
Δh_o	Enthalpy change

Greek Letters

ρ	Density

ζ	Rotor meridional velocity ratio
β	Relative flow angle
α	Absolute flow angle
ψ	Blade loading coefficient
ω	Rotational speed
ϕ	Flow coefficient
η	Efficiency
ν	Velocity ratio
γ	Specific heat ratio
σ	Slip factor
τ	Shear stress, Torque
ε	Clearance gap
δx	Uncertainty in measuring the quantity x

Subscripts

0-6	stage number for turbine and compressor
amb	Ambient
$comp$	Compressor
e	Electrical
h	Hub
inc	Incidence
le	Leading edge
m	Meridional component
max	Maximum
$mech$	Mechanical
o	Total thermodynamic condition
opt	Optimum
pas	Passage
r	Recuperator
st	Stator
t	Tip
te	Trailing edge

$turb$	Turbine
ts	Total to static
tt	Total to total
vld	Vaneless Space
θ	Tangential component, Guide vane angle
v	Nozzle guide vane

Abbreviations

CFD	Computational Fluid Dynamics
MGT	Micro Gas Turbine
FEA	Finite Element Analysis
HSG	High Speed Generator
NGV	Nozzle Guide Vanes
FEM	Finite Element Analysis

Chapter 1

1. Introduction

1.1 Background

Solar energy provides a feasible and clean solution for power generation in areas that have a high solar irradiation. The existing solar power generation systems are divided into two categories: solar cells (photovoltaic cells) and concentrated solar power systems. The concentrated solar power systems are able to meet a wide range of power requirements, parabolic troughs and solar tower technologies can provide power for large capacity plants and dish-sterling engine systems can be employed in the small capacity plants. In the last two decades, the European Commission has funded a number of projects in an attempt to utilise concentrated solar power in conjunction with gas turbines to generate electricity. Between 2000 and 2005, SOLGATE [1] was one of the projects aimed at studying the economic and technical feasibility of using concentrated solar power in conjunction with fossil fuels to operate a 30 MW gas turbine. In 2006 SOLHYCO project [2] was initiated to develop and test a reliable solar hybrid power generation system using a commercially available gas turbine of 100 kW. More recently the SOLUGAS project [3] used a commercial 5 MW gas turbine to demonstrate the ability to build a solar heated power system which is cost effective and has the flexibility to move to different

sites. Despite the progress in the development of such systems using relatively large scale gas turbines, no attempts have been made to explore both the techno-economic feasibility and the potential market for small scale solar dish-gas turbine systems. Optimised Microturbine for Solar Power OMSoP (see section 1.2) initiated this research targeting a cost-effective and reliable system with higher efficiency than conventional dish-sterling engines. Higher efficiency means a smaller dish, less land occupancy and lower cost as the major cost for such systems is the solar dish. In addition, the replacement of the sterling engine by a micro-gas turbine appears to have particular advantages. One of which is that a micro-gas turbine is easier to maintain than a sterling engine. Furthermore, the hot exhaust gas of the micro gas turbine can be utilised in fuel cells or one of the water treatment technologies to attain a higher efficiency for the system.

The success in achieving high performance solar dish gas turbine system will allow such a system to compete with the Photo Voltaic PV cells despite their cheaper price. The main reason for that is the less land occupancy requirement for the same power output and the possibility to recover the exhaust heat power which results in much higher efficiency system.

1.2 OMSoP Project Scope and Objectives

Optimised Microturbine Solar Power "OMSoP" is a project funded by the European Commission 7th Framework Programme. The overall objective of this project is to demonstrate an integrated solar dish-gas turbine system that can potentially compete with the conventional dish sterling engines. The system to be built, should be able to produce 6 kWe that is able to provide energy for small commercial business and domestic applications. The development of such small system that is economically viable, efficient, reliable and easy to maintain includes different challenges related to the optical system,

micro gas turbine design, thermal storage and the control procedure. Eight partners have been involved in this project, where the responsibilities allocated for each one are:

- City, University of London: is the coordinator of the project and responsible for design and build of an optimised Micro Gas Turbine (MGT) for the solar application in addition to participation in the design of the control system for the plant and taking part in the system modelling, integration and demonstration. Within City, the author is responsible for designing the turbomachinery components of the MGT and contributing towards the overall commissioning and testing of the MGT. Three other researchers have the responsibility for the thermodynamic cycle optimisation, mechanical design and rotor dynamic stability of the MGT, the development of the control method to implemented within the plant and contributing towards the commissioning and testing of the MGT.

- Roma Tre University: is involved in the design of a short-term thermal storage to be integrated to the solar receiver. The thermal storage is a promising solution to improve the operational capability of the system under solar irradiation fluctuation. In addition, Roma Tre University is involved with other partners in the system testing and the techno-economic optimisation of the plant.

- The Italian National Agency for New Technologies, Energy and Sustainable Economic Development (ENEA): is responsible of modeling and simulating the solar unit and plays a role in the design of the integrated plant. ENEA will be involved in the realization of the demonstration plant, which will be assembled at their site and they are responsible for running the system and demonstrating its functionality and controllability.

- Innova: is responsible for building an optimised solar dish with the tracking system.

- Compower: Compower alongside City is involved in constructing the control system for the demonstration plant, cost analysis and cycle optimisation.

- Royal Institute of Technology (KTH): The development and testing of the solar receiver.

- University of Seville: performs market and cost analysis of the solar MGT to find and identify the best size of the system, and to find a potential market for it.

- European Turbine Network (ETN): ETN is responsible for dissemination activities.

1.3 Micro-Gas Turbines

The use of gas turbines as electrical generators started in 1939 [4]. Gas turbines are internal combustion engines which operate on Brayton thermodynamic cycle. Referring to figure 1.1 (simple gas turbine cycle), air from the ambient firstly enters the compressor to be compressed (1-2). The high pressure air then enters the combustion chamber where it mixes with the fuel and then burned at constant pressure (2-3). From the combustion chamber the burned gases leave at high pressure and temperature.

These hot gases then enter the turbine, where they expand and energy is extracted in the form of kinetic energy used to spin the rotating part of the turbine (3-4). In the last stage, the exhaust gases leave the expander either to the ambient (4-1). In the solar powered gas turbines; the solar receiver replaces the combustion chamber, so that the compressed air from the compressor enters into the receiver to be heated from the solar energy collected in the solar receiver.
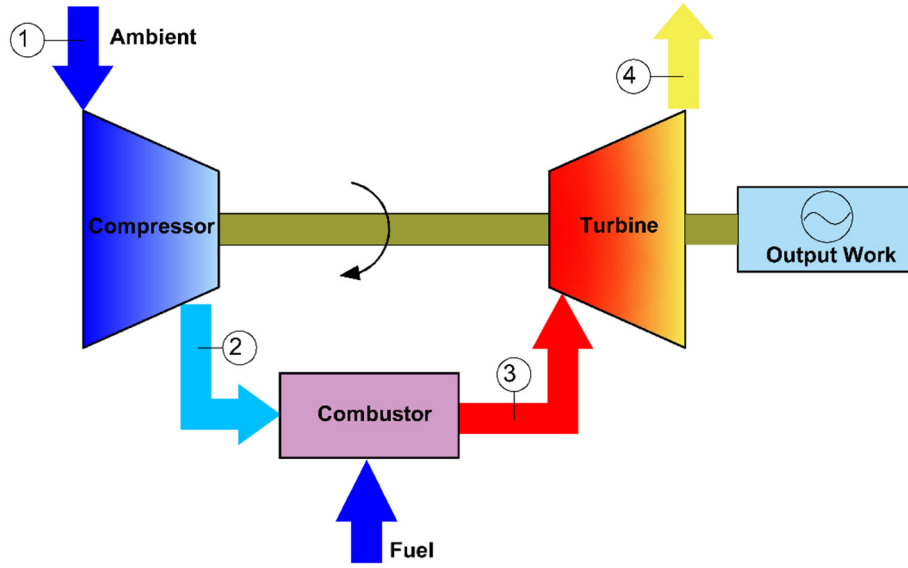
Figure 1.1: Schematic for a simple gas turbine cycle

Temperature-entropy (T-s) diagram for an open cycle gas turbine is plotted in figure 1.2, where the stages 1-4 are identical in figures 1.1 and 1.2. The ideal efficiency for Brayton cycle is given as:

$$\eta_{ideal} = \frac{\text{specific work output } (W_s)}{\text{specific input power}} = \frac{W_{turb} - W_{comp}}{q_{in}} \qquad (1.1)$$

Where q_{in} is the total input thermal power per unit mass, W_{turb} specific power generated by the turbine and W_{comp} is the specific power consumed by the compressor which can be written as:

$$q_{in} = c_p(T_3 - T_2) \qquad (1.2)$$

$$W_{turb} = c_p(T_3 - T_4) \qquad (1.3)$$

$$W_{comp} = c_p(T_2 - T_1) \qquad (1.4)$$

By substituting 2, 3 and 4 in 1 and using the isentropic relations between the stages 1-2 and 3-4, the efficiency of the ideal Brayton cycle would be:

$$\eta_{ideal} = 1 - \frac{1}{PR^{(\gamma-1/\gamma)}} \qquad (1.5)$$

5
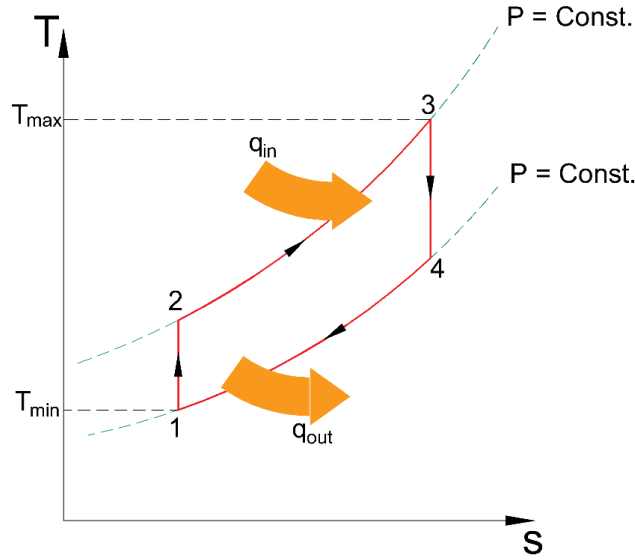
Figure 1.2: T-s diagram for ideal Brayton cycle

Where *PR* is the compressor pressure ratio, which in the ideal case equals the turbine expansion ratio ($PR = P_2/P_1 = P_3/P_4$) and γ is the specific heat ratio of the working fluid. Referring to equation 1.5, the main parameters that affect the cycle and hence the MGT efficiency are: the operating pressure ratio and the working fluid specific heat ratio. By considering the specific power output of the gas turbine (refer to equation 1.6), the efficiency will not be a function of the pressure ratio and the specific heat only, additionally, it depends on the ratio of the maximum temperature to the minimum temperature of the operating fluid T_3 and T_1 respectively.

$$\frac{W_s}{c_p T_1} = \frac{T_3}{T_1}\left(1 - \frac{1}{PR^{(\gamma-1/\gamma)}}\right) - \left(PR^{(\gamma-1/\gamma)} - 1\right) \qquad (1.6)$$

With air breathing turbines, the specific heat temperature is determined by the ambient temperature at the compressor inlet, therefore it cannot be modified to enhance the gas turbine performance. Meanwhile increasing the pressure ratio and the turbine entry temperature are achievable with some limitations. In the absence of the cooling mechanisms for the small radial turbomachines, the turbine entry temperature is limited by the maximum allowable temperature for the rotor blades material. To increase the pressure ratio of the MGT, careful attention is needed when designing the compressor.

6

Increasing the pressure ratio could lead to supersonic inlet, which in turn cause shock

losses which deteriorate the compressor efficiency leading to worse MGT performance.

In addition, the pressure ratio is linked with the turbine entry temperature, when operating

the MGT at a specific temperature, increasing the pressure ratio will enhance the MGT

performance till reaching the maximum efficiency and thereafter the performance will

drop down again. By differentiating equation 1.6 with respect to $PR^{(\gamma-1/\gamma)}$ and equate it

to zero, the maximum specific power that can be achieved using pressure ratio $(PR) =$

$T_3/T_1^{\gamma/2(\gamma-1)}$.

In the actual gas turbines, the compression and expansion processes do not occur

isentropically because of the irreversibility that combine each process. Less importantly,

the slight drop in pressure during both the heat addition in the combustor and the heat

rejection from the exhaust gases. Hence figure 1.2 requires modifications to describe the

actual process. Figure 1.3 shows the temperature-entropy (T-s) diagram for the actual gas

turbine, where the compressor operates between the states 1 and 2a, and the turbine

between 3 and 4a.
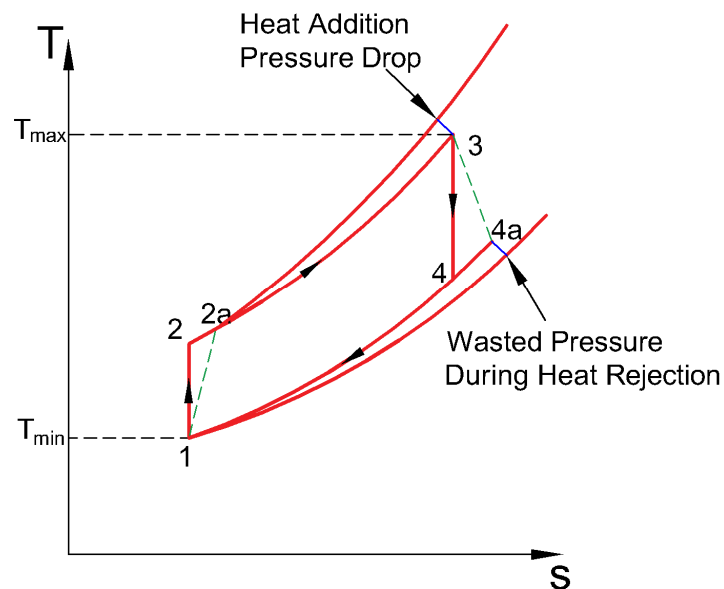
Figure 1.3: T-s diagram for real gas turbine

Equation 1.7 gives the cycle efficiency for the actual gas turbine.

$$\eta_{actual} = \frac{\text{specific work output}}{\text{specific input power}} = \frac{(T_3 - T_{4a}) - (T_{2a} - T_1)}{(T_3 - T_{2a})} \qquad (1.7)$$

To measure the deviation between the ideal and the real turbine and compressor, the isentropic efficiency has been defined for them as follows (see sections 2.1.1 & 2.2.1).

$$\eta_{comp} = \frac{T_2 - T_1}{T_{2a} - T_1} \qquad (1.8)$$

$$\eta_{turb} = \frac{T_3 - T_{4a}}{T_3 - T_4} \qquad (1.9)$$

Based on this definition, equation 1.7 becomes

$$\eta_{actual} = \frac{\eta_{turb}(T_3 - T_4) - \frac{1}{\eta_{comp}}(T_2 - T_1)}{(T_3 - T_{2a})} \qquad (1.10)$$

Equation 1.10 indicates that the gas turbine efficiency is strongly related to the efficiency of the turbomachinery components and not only on the cycle pressure ratio and maximum cycle temperature as the ideal machine.

1.4 MGT Development

MGTs are usually identified by their output power rating, which is usually defined in the range between 2-200 kWe [5]. Most of those machines employ radial turbines and centrifugal compressors in their design instead of axial machines as they are more beneficial. Radial turbines are preferred over axial ones in small engines because they have lower blockage and tip clearance losses, offer more compact design and they produce higher specific work because of the radius change along the impeller [6]. Also, the compactness, the ability to operate over wide range of mass flows and the ability to accommodate small flows make the centrifugal compressors more suitable for small engines than axial compressors. Table 1 shows a survey for the available MGTs available in the market which use radial turbomachines.

Table 1-1: The specification of some commercial micro gas turbines

Manufacturer	Model	Power output	Rotational speed	Recuperation	Efficiency (%)
Capstone Turbine [7]	M330	30KWe	96 krpm	Yes	28
Nissan [8]	IHI Dynajet (2.6 KW)	2.6 KWe	100 krpm	Yes	12
Honeywell Power systems [7]	Parallon (75KW)	75KWe	65 krpm	Yes	27.5
Ingersoll-Rand [9]	Power Works (70kW)	70 kWe	44 krpm	Yes	25.7
Turbec [10]	T100P	100 kWe	70 krpm	Yes	30
MTT [11]	EnerTwin	3 kWe	240 krpm	Yes	12

As can be observed, the low capacity MGTs of less than 10 kWe output are suffering from low efficiency, therefore City University is targeting to develop an MGT with a total efficiency greater than 25%. To achieve this goal, City followed the subsequent routes:

- Amending the MGT cycle:

  The efficiency of a gas turbine can be doubled by introducing a recuperator to recover part of the dissipated heat from the turbine exhaust. Therefore, City modified the simple MGT cycle by adding a regenerator to enhance the system performance. Although adding a recuperator will increase the initial cost of the MGT, increasing the solar cycle performance causes a significant drop in the size and the cost of the solar dish which forms two thirds of total system cost [12]. Figure 1.4 shows City solar MGT cycle schematic and the T-s diagram for it which can show the effect of adding the recuperator in recovering part of the exhaust energy to heat up the gas before entering the solar receiver.

- Improving the turbomachinery performance:

At City, the intention is to improve the performance of the turbine and the compressor of the MGT using the available design and Computational Fluid Dynamics tools to suite the solar application. In addition, City studying the feasibility of introducing engineered features to the turbine rotor walls to improve its aerodynamic characteristics. This development will not add any extra cost to the system but it has a great effect in enhancing the MGT performance and therefore cutting some of the cost and size of the dish.
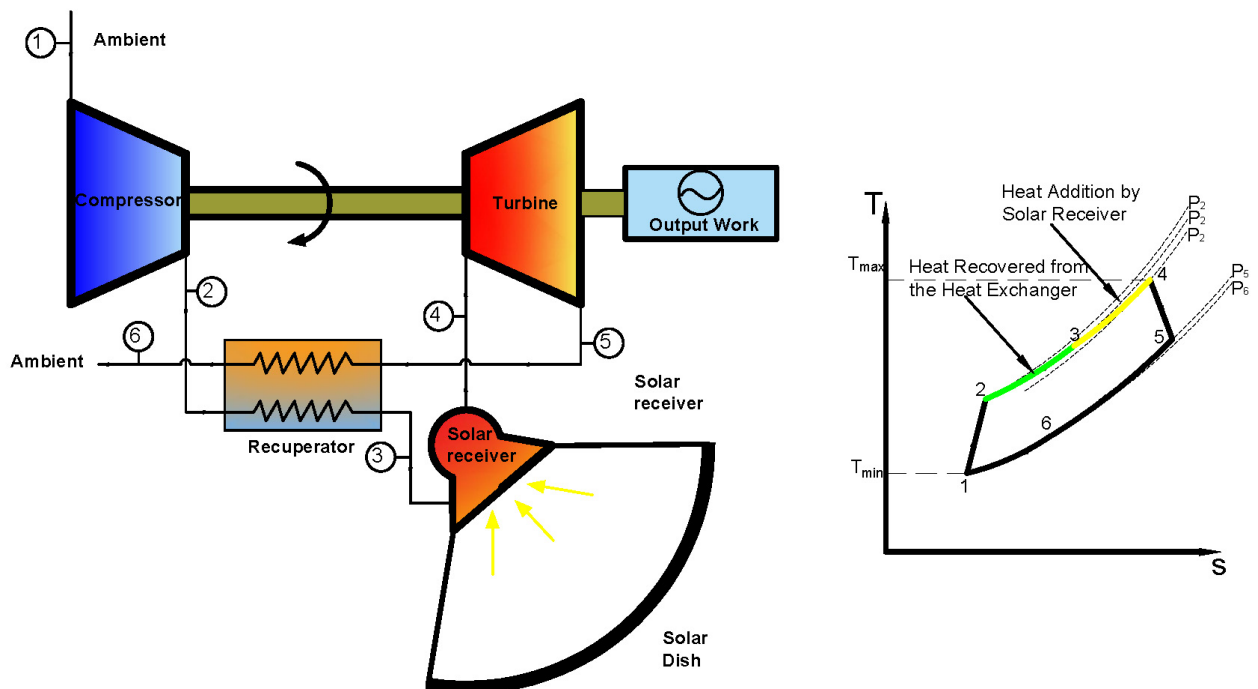
Figure 1.4: Schematic for the recuperated solar powered gas turbine cycle

1.5 Research Objectives

This research is part of City University's contribution towards improving the solar dish-micro gas turbine system within the OMSoP project. The main objective of this research, is to explore suitable methods to be applied to the turbomachinery components in order to enhance their efficiency and the predictability of their performance over the operating range of the solar-dish MGT system.

The specific objectives of this research are:

- To understand the effects of implementing engineered features to the turbine rotor hub on the flow characteristics within the rotor passage. For this purpose, cusp shaped riblets will be considered as they are practically achievable.

- To determine the best size and arrangement of the riblets which maximize the efficiency of the turbine.

- To develop an accurate and fast method to predict the performance of the radial turbines and the centrifugal compressors allowing for efficient design process.

- To contribute to the overall design and testing of the solar dish micro gas turbine system.

1.6 Thesis Outline

This thesis consists of seven chapters starting with this introduction. The second chapter contains theoretical background of the micro gas turbine system components addressed in this thesis as well as a critical review of previous related research. A particular literature review related to detailed aspects of the turbine are outlined in the related chapters to allow a more convenient link to the discussion.

Chapters 3 presents a full description for a methodology for designing and performance predictions for a centrifugal compressor for a 6 kWe solar powered MGT. The preliminary design parameters were obtained from the overall system specifications and detailed cycle analysis and practical constraints. A meanline methodology was then used to calculate the main geometric parameters for the compressor components. These were subsequently used to generate a three-dimensional geometry of the impeller and diffuser

vanes, and the volute. In addition, the compressor performance estimated using Computational Fluid Dynamics (CFD) results combined with the one-dimensional correlations.

Chapter 4, is similar to chapter 3 in its structure with application to the radial turbine where a full description for a methodology for designing and performance prediction for a turbine to match the compressor characteristics for the same MGT. At the end of the chapter, the proposed performance prediction and design methods were validated against the experimental data for the actual turbine.

In chapter 5, a novel idea of reducing the turbine rotor friction losses by adding riblets to the rotor hub is explored thoroughly. Numerical simulations have been used to study the effects of those features at design point conditions of the MGT. Riblets with different height and spacing have been examined to determine the riblet geometry where the maximum drag reduction is achieved. The relative height of the riblets to rotor inlet blade height was introduced to generalise the results. At the end of the chapter, the results of the study were compared with the available data in literature.

In the Chapter 6, the contribution towards building the MGT is presented. This chapter also includes the details of the MGT components design and arrangement. To evaluate the accuracy of the design and performance prediction procedures, the designed turbine was tested in a purpose built test rig. Within this chapter, the test rig description, instrumentation used and the uncertainty analysis are presented. Finally, the test rig performance maps were compared with the predicted ones.

The final conclusions of this research and recommendations for the future work are presented in chapter 7.

1.7 Contributions

The main contributions of this research are:

- The effect of rotor hub surface riblets on the aerodynamic performance of the turbine has been investigated thoroughly and explained.

- The geometrical parameters of the riblets at which the maximum turbine performance occurs were determined.

- A method for predicting radial turbines' performance has been developed within this research. This method was applied to an existing machine to generate it's performance maps. The generated results were the validated against the experimental tests for the turbine.

- Similar to the turbine a method for predicting the centrifugal compressors' performance has been developed, and applied to an existing compressor. However, the compressor was not tested to validate the predictions.

- As part of team work, a solar powered MGT of power output of 6 kWe has been designed and manufactured. The development of such small machine will help in understanding their behaviour and the problems that limits their existence as reliable machines. Future tests will focus on the rotordynamics' stability and the thermal management within the machine.

The following publication arose from this research:

M. Khader and A. I. Sayma, "Effect of End-Wall Riblets on radial Turbine Performance," in *10th International Conference on Compressors and their Systems*, London, 2017.

D. Iaria, M. Khader, A. I. Sayma and J. Alzaili, "Parametric Multi-Objective Optimisation of A Centrifugal Compressor for A Micro Gas Turbine Operated by Concentrated Solar Power," in *Global Power and Propulsion Society,* Zurich, 2017.

Chapter 2

2. Literature Review

2.1 Centrifugal Compressors

A centrifugal compressor is a turbomachine that increases the pressure of the gas by converting the shaft work into a kinetic energy conserved within the flow. Figure 2.1 shows components of a centrifugal compressor. This machine has rotating and stationary components. The rotating component is called the impeller and the stationary parts are mainly; the inducer, diffuser and the volute.

Compressor impeller is the rotating component of the compressor. There are two types of impellers commonly used, shrouded and unshrouded. For gas-turbines and turbochargers the impeller is usually unshrouded (the impeller is uncovered) because of high stresses on the compressor wheel. For small compressors, partial or splitter blades are usually used to increase the number of blades without increasing the blockage at the inducer section.

The inducer is simply the inlet duct, which could be a straight or a curved passage of multistage compressor or the final stage of an axial compressor. The diffuser collects the discharge flow from the compressor impeller and increases the static pressure of the flow by reducing its' kinetic energy. The diffuser may be vaned or vaneless, and good diffuser performance is also very important [6]. The volute is a duct that collects the compressed fluid from the diffuser and directs it to a single passage that can be connected to the system, where the compressed air is needed.
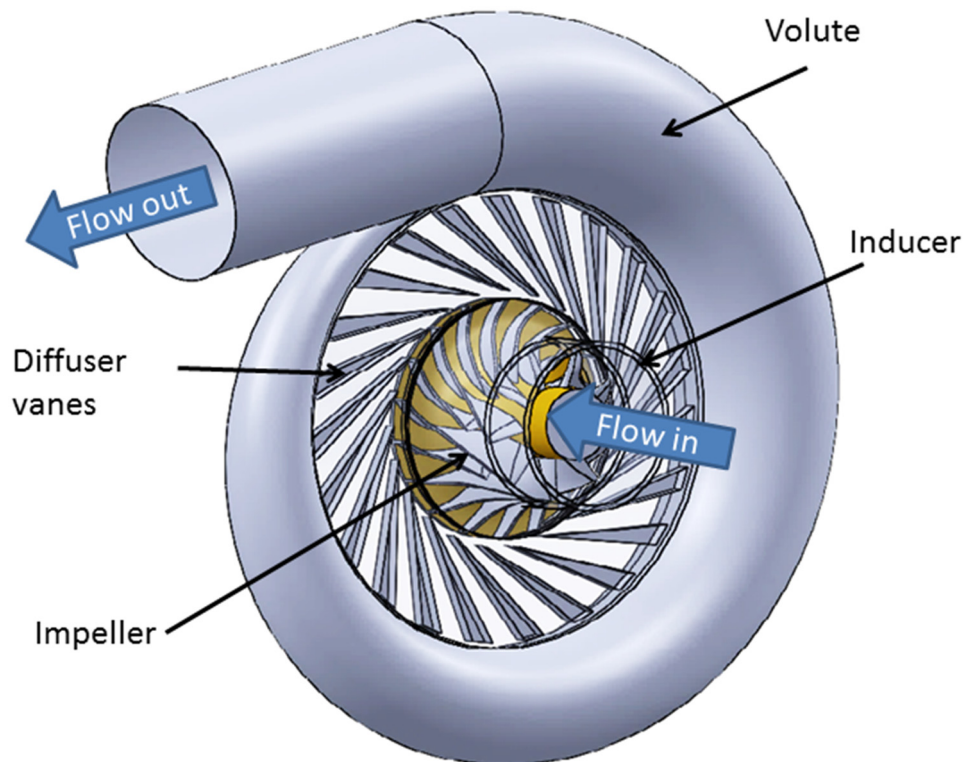
Figure 2.1: Components of a traditional centrifugal-compressor stage

2.2.1 Compressor Stage Basics

The interaction between the fluid and the compressor's components, causes the pressure of the fluid to increases. Referring to figure 2.2, initially, the fluid inters to the inducer with total pressure P_{o0} and total temperature T_{o0} and exit from the inducer with the same temperature and pressure as there is no work added or extracted from the fluid. After passing through the inducer, fluid enters the impeller with total pressure P_{o1} which equals P_{o0} and total temperature T_{o1} which equals T_{o0}. Across the impeller; shaft work is done on the fluid causing the total pressure and temperature of the fluid to increase to P_{o2} and T_{o2} respectively. The fluid exits from the impeller entering the diffuser with total pressure and temperature P_{o3} and T_{o3} respectively, which equal to P_{o2} and T_{o2}. Through the diffuser, the fluid discharge area increases which causes a drop in the flow velocity, thus increasing its static pressure.
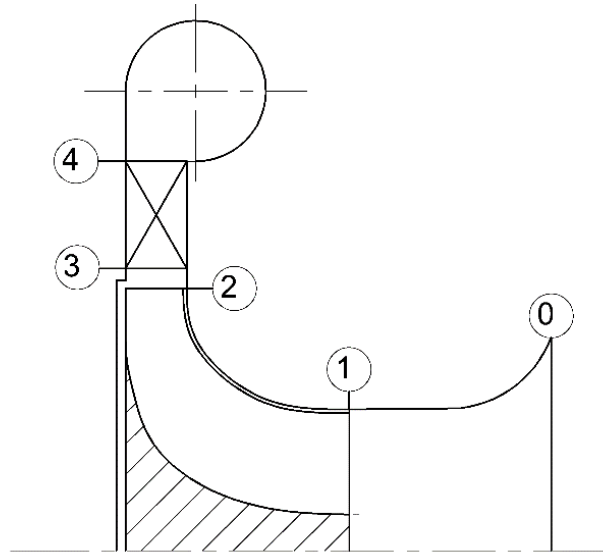
Figure 2.2: Centrifugal compressor schematic

The focus now will be directed towards analysing the fluid along the impeller, which is

the most important part of the compressor as the work is added there. Figure (2.3a) shows

the velocity triangle of the fluid at the impeller exit and figure (2.3b) shows the velocity

triangle at impeller inlet. Based on Euler turbomachinery equation; the torque and the

specific power added by the impeller can be calculated as follows:

$$\tau = \dot{m}(r_2 C_{\theta 2} - r_1 C_{\theta 1}) \qquad (2.1)$$

$$\dot{W} = \dot{m}(U_2 C_{\theta 2} - U_3 C_{\theta 3}) \qquad (2.2)$$

| (a) | (b) |
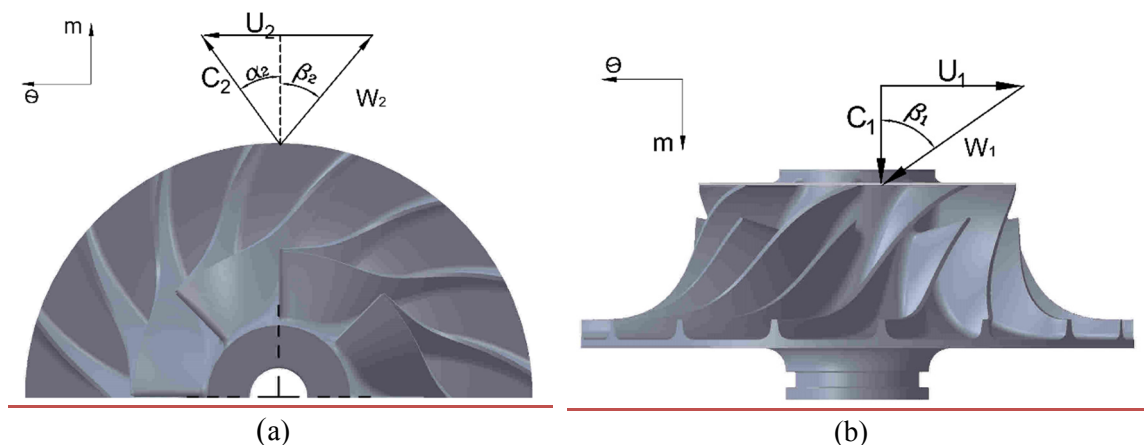
Figure 2.3: (a) Velocity triangle at impeller discharge, (b) Mean velocity triangle at impeller inlet

By applying the energy equation on the adiabatic flow through the impeller the specific

power can be written in terms of the total enthalpy change.

16

$$\dot{W} = \dot{m}(h_{02} - h_{01}) \tag{2.3}$$

And by combining the equations 2.23 and 2.24, the temperature ratio across the rotor can be given by:

$$\frac{T_{02}}{T_{01}} = 1 + \frac{1}{c_p T_{01}}(U_2 C_{\theta 2} - U_1 C_{\theta 1}) \tag{2.4}$$

To calculate the pressure ratio across the impeller, the losses which occur in the impeller must be known. A simpler way to calculate the pressure ratio is to assume an efficiency for the impeller η_{tt}, and then from the definition of the efficiency, determine the pressure ratio as follows.

$$\left(\frac{P_{02}}{P_{01}}\right)^{\frac{\gamma-1}{\gamma}} = 1 + \frac{1}{c_p T_{01}}\eta_{tt}(U_2 C_{\theta 2} - U_1 C_{\theta 1}) \tag{2.5}$$

To calculate the pressure ratio for the whole stage, equation 2.5 can be used by replacing the stage total efficiency instead of defining impeller efficiency [13].

Thermodynamically, the compressor efficiency is defined as actual shaft work consumed to the ideal work that needed using an ideal machine. Two definitions of the isentropic efficiency are available, one of which, is based on the discharge total thermodynamic state and the other uses the exit static condition. Equation 2.6 represents the total to total isentropic efficiency, which is usually used when the exit kinetic energy of the compressor is utilised.

$$\eta_{tt} = \frac{h_{o4s} - h_{o0}}{h_{o4} - h_{o0}} \tag{2.6}$$

Wherever the exit kinetic energy is wasted the total to static definition in equation 2.7 is used to describe the compressor efficiency.

$$\eta_{ts} = \frac{h_{4s} - h_{o0}}{h_{o4} - h_{o0}} \tag{2.7}$$

2.2.2 Compressor Performance Prediction

Loss prediction is an important tool for the compressor design process as it helps to predict the centrifugal compressor performance and understand its' operational characteristics before building the actual machine. Many one-dimensional loss models have been proposed to predict losses in centrifugal compressors. Those models estimate the losses within the compressor at different operating condition using the loss correlations for each source of loss. Therefore, this section highlights the loss sources within the compressor and describes the correlations developed to predict their contribution to the compressor performance drop. Building on this understanding of the different loss sources, an improved performance prediction tools was developed within chapter four which is believed to give more realistic predictions for the compressor performance.

Losses in centrifugal compressors mainly occur at the impeller, and this section will be employed to discuss these loss models. Losses in centrifugal compressor are divided into two groups; the first group, which is related to the main flow called internal losses, which include blade loading, tip clearance, skin friction and mixing losses. The second group are called parasitic losses which are caused from the flows leaks from the main flow stream; these losses are the windage (disc friction), recirculation and leakage losses.

Incidence Loss

Incidence loss is the amount of work dissipated to turn the fluid from its direction to the blades direction. A zero or near zero incidence angle considered to be the optimum to reduce the incidence loss. Oh *et al*. [14] found that the model developed by Conrad *et al*. [15] gives the most accurate estimate for the incidence loss compared to the experimental

results. According to this model incidence loss can be calculated as an enthalpy change using the following formula:

$$\Delta h_{inc} = f_{inc} \frac{W_{\theta 1}^2}{2} \tag{2.8}$$

Where f_{inc} is the energy loss coefficient, where a value between $0.5 - 0.7$ was found to give the best results.

Blade Loading Loss

Blade loading loss is the loss that occurs due to the secondary flows generated within the impeller passage due to the pressure gradient between pressure and suction surfaces of the blades. It can be calculated using Coppage *et al.* [16] formula:

$$\Delta h_{bld} = 0.05 D_f^2 U_2^2 \tag{2.9}$$

Where D_f is the diffusion factor, this factor indicates the flow deceleration within the impeller passage which can be calculated using equation 2.10.

$$D_f = 1 - \frac{W_2}{W_{1t}} + \frac{\left(0.75 \frac{C_{\theta 2} U_2 - C_{\theta 1} U_1}{U_2^2}\right)}{\left(\frac{W_{1t}}{W_2}\right)\left[\frac{N_b}{\pi}\left(1 - \frac{D_{1t}}{D_2}\right) + 2\frac{D_{1t}}{D_2}\right]} \tag{2.10}$$

Skin Friction Loss

Skin friction loss occurs due to the viscous shear forces between the impeller passage surface and the fluid. Assuming the flow inside the impeller passage as a flow inside a circular cross section pipe, then skin friction loss can be calculated using Jansen's [17] formula as follows:

$$\Delta h_{skin} = 2 C_f \frac{L_H}{D_H}\left[\frac{C_{t1} + C_2 + W_{1t} + 2W_{1h} + 3W_2}{8}\right] \tag{2.11}$$

The hydraulic length and the hydraulic diameter can be calculated as in equations 2.30 and 2.31 respectively; C_f is the skin friction coefficient for the impeller surface.

Tip Clearance Loss

Tip clearance for a centrifugal compressor is the gap that exists between the compressor impeller and the casing in the unshrouded compressor. The tip gap in centrifugal compressors could reach 7% of the local span height [18] depending on the FEA results. Xi *et al*. [19], studied the tip clearance effect on flow field for NASA LSCC. The study found that the tip clearance height affects the size and the location of the wake at the impeller discharge.

 It was also found that zero tip clearance is not the optimum for the performance of the centrifugal compressor and better performance could be achieved with a small tip clearance. Wang *et al*. [20] studied the effect of the tip clearance height on a high-pressure ratio centrifugal compressor experimentally. The results identified that increasing the tip clearance heights leads to an increase in the secondary flow region in the flow channel which affects the main flow in the impeller passage. Abhari *et al*. [21] found from his Laser Doppler Anemometry (LDA) at the centrifugal compressor impeller discharge, that the tip clearance flow affects the flow in the diffuser mainly the size and the location of the wake. Jung *et al*. [22] analysed the effect of the non-uniformity in the tip clearance heights numerically. In this study, six impellers were tested with different tip clearance distributions. The study found that reducing the tip clearance height enhance the efficiency of the compressor, and also found that reducing the clearance height at the impeller exit has a greater effect on the performance. According to this study, reducing tip clearance at the impeller exit reduces the mixing loss caused from the interference between the flow leaking from the tip gap and the main flow. Jaatinen *et al*. [23] performed an experiment to test the effect of the tip clearance on the performance of the centrifugal compressor. The experiment shows that increasing the tip clearance heights reduces the performance of the compressor. Also, they found that the effect of tip

clearance depends on the operating point of the compressor, as the decrement in the performance become larger for higher mass flow rates and it reduces for smaller mass flows. Hong *et al.* [21] found that for three percentage points increment in the tip clearance height the efficiency of the compressor would be decreased by one percent. Kang *et al.* [24] found from his literature survey that approximate 20-40% of the total loss are due to tip clearance loss. Jansen [17] in equation 2.12 evaluates the tip clearance losses due to the mixing of the flow that passes the gap with low momentum flow in suction side of the impeller blade.

$$\Delta h_{cl} = 0.6 \frac{\varepsilon_c}{b_2} \left[\frac{4\pi}{b_2 N_b} \left(\frac{r_{t1}{}^2 - r_{h1}{}^2}{(r_2 - r_{t1})(1 + \frac{\rho_2}{\rho_1})} \right) C_{t2}{}^2 C_{m1} \right] \qquad (2.12)$$

Where ε_c is the clearance distance between the blades tip and the casing.

Windage (Disc Friction) Loss

Like radial turbine the viscous forces of fluid between the back face of the impeller and the casing cause a friction loss. One of the most famous formulas used to account for this loss is Whitefield and Baines [6] which is derived from Daily and Nece [25]. This formula expresses the friction loss as a dissipated power. Dividing the power consumed by friction by the mass flow rate enthalpy loss can be found as follows:

$$\Delta h_w = \frac{\Delta P_w}{\dot{m}} = \frac{\frac{1}{4} K_f \bar{\rho} \omega^2 r_2{}^2}{\dot{m}} \qquad (2.13)$$

Where, $\bar{\rho}$ is the average density between impeller inlet and exit, K_f is a coefficient that can be determined based on Reynolds number at impeller discharge, so for $R_e < 3 \times 10^5$ it can be calculated using the flowing formula:

$$K_f = \frac{2.67}{R_e{}^{0.5}} \qquad (2.14)$$

And for $R_e > 3 \times 10^5$ K_f can be calculated as follows:

$$K_f = \frac{0.0622}{R_e^{0.2}}$$

(2.15)

Where: ε is the distance between the back face of the rotor and the casing. Reynolds number can be calculated at the impeller discharge using equation 2.16.

$$R_e = \frac{\rho_2 r_2 U_2}{\mu}$$

(2.16)

Vaneless Diffuser Loss

Following the compressor impeller there is a vaneless space separating the impeller from the diffuser vanes, this space must be sufficient so the separated flow from the diffuser doesn't affect the impeller exit flow causing more losses. Figure 2.4a shows the effect of the small vaneless gap on the impeller exit flow, as the separated flow from the diffuser suction surface pushes the impeller exit flow causing losses. Figure 2.4b shows a larger vaneless gap where the impeller exit flow is less affected by the diffuse, which means lower losses.
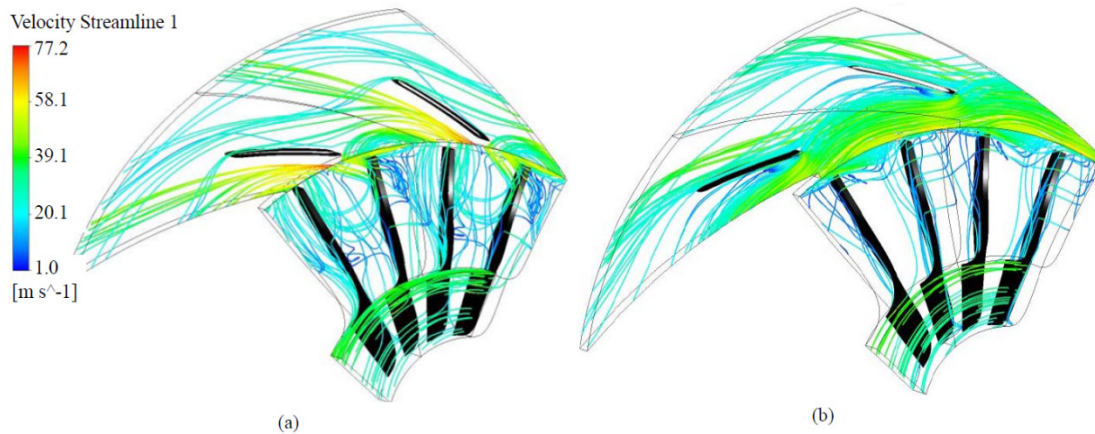
Figure 2.4: Flow within the vaneless space of a centrifugal compressor (a) small gap (b) large gap [26]

Equation 2.17 presents Stanitz [27] model for calculating the vaneless loss for centrifugal compressors.

$$\Delta h_{vld} = cT_{02}\left[\left(\frac{P_3}{P_{03}}\right)^{\frac{\gamma-1}{\gamma}} - \left(\frac{P_3}{P_{02}}\right)^{\frac{\gamma-1}{\gamma}}\right] \tag{2.17}$$

Recirculation Loss

The high-pressure fluid exiting from the impeller pressure surface side moves toward the low pressure side of the blade, pushing the low momentum fluid back toward the impeller causing recirculation losses. Oh *et al.* [14] developed a model to predict the effect of these losses as an enthalpy drop as shown in equation 2.18.

$$\Delta h_{rc} = 8\times 10^{-5}sinh(3.5\alpha_2{}^3)U_2{}^2D_f{}^2 \tag{2.18}$$

Where D_f is the diffusion factor defined in equation 2.10.

Mixing Loss

The flow that leaves the impeller has a high momentum region which is called the jet region, and a low momentum region called the wake region. This definition for these two zones was originally adopted by Dean and Senoo [28]. Later, Johnston and Dean [29] developed a two-dimensional mixing loss model assuming constant relative velocity in the axial direction at the impeller exit. Also, they have assumed a zero relative flow velocity in the wake region and a constant static pressure around the impeller. According to their model mixing loss occurs due the sudden expansion of the flow when the high jet flow mixes with low velocity flow. Equation 3.18 shows the final form of this model.

$$\Delta h_{mix} = \frac{1}{1+tan^2(\alpha 2)}\left(\frac{1-\varepsilon-b^*}{1-\varepsilon}\right)\frac{C_2{}^2}{2} \tag{2.19}$$

Where: $b^*$is the ratio of the vaneless diffuser depth to the impeller exit width, which must be 1 or greater for this model to be valid. ε is the space occupied by the wake to the blades passage spacing.

2.2.3 Flow in Centrifugal Compressors

Analysing the flow in the centrifugal compressors using experimental measurements and CFD simulations started long time ago because of the wide spread use of those machines in different applications. This section describes the main flow characteristics within the impeller passages based on the available literature.

The flow entering the compressor impeller can be introduced by considering the velocity triangle shown in figure 2.3b. The incidence angle can be defined as difference between blade angle and relative velocity angle. Optimum incidence according to Japikse [18] is zero or around zero from either the negative and positive direction. Figure 2.5 shows the effect of increasing the incidence angle on the flow at impeller inlet. Referring to the velocity triangle at the impeller's inducer in figure 2.3b, reducing the mass flow through the compressor while maintain a constant rotational speed will cause a drop in the axial component of the absolute flow velocity. Hence the relative flow angle will increase which means higher incidence angle at the blades leading edge which causes the boundary layer to separate. This phenomenon is called the inducer stall in centrifugal compressor.
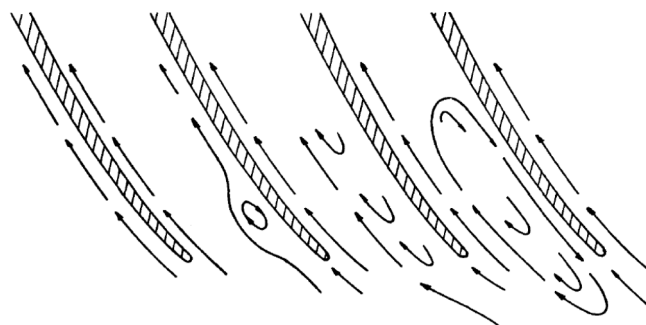
Figure 2.5: Effect of increasing incidence angle on impeller inducer flow (incidence increases from left to right [18]

Returning to figure 2.3b, the flow usually enters axially to the impeller; however, pre-swirl is sometimes added to reduce the input power to the compressor. This pre-swirl can be achieved by using inlet guide vanes before the impeller inlet.

As the flow enters the impeller, a viscous boundary layer starts to develop along the passage walls. If no distortion happens to the flow at the impeller inlet, the flow will tend to move in the same direction of the passage. After the flow proceeds, centrifugal force, cross passage forces due to pressure difference, geometry curvature and the flow leakage from tip clearance gap, cause a development of complex flow patterns along the impeller passage. Eckardt [30] studied the flow within a centrifugal compressor impeller by using laser velocity-meter readings at six different stages along the impeller passage. Figure 2.6 shows Eckardt's results, where, he generated drawings for the non-dimensional meridional velocity for the flow across the impeller passage.
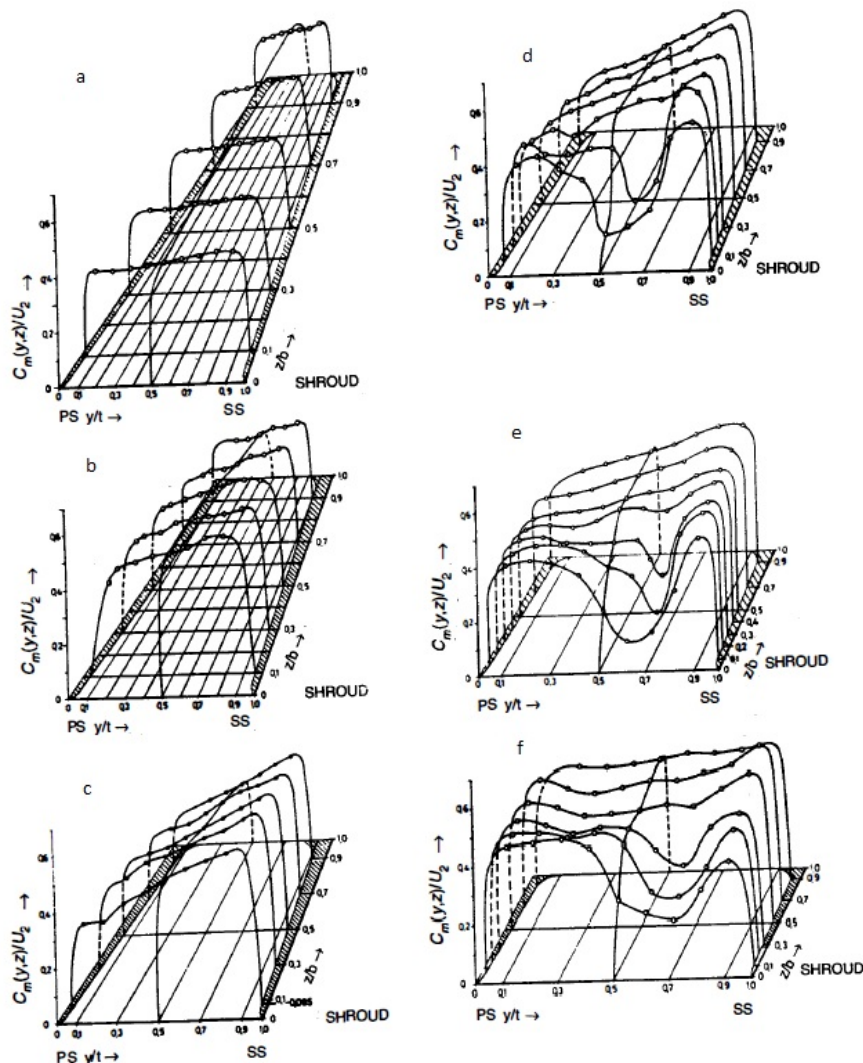
Figure 2.6: Flow velocity distribution at various station for Eckardt impeller [30]

The first two drawings (a and b) show the velocity distribution at the inducer part of the impeller where the velocity distribution is uniform. Drawings (c and d) show the flow velocity within the bend from axial to radial; at this region a low momentum region (secondary flows) starts to appear at the shroud suction corner. These secondary flows continue to appear at the shroud suction corner until the flow discharges from the impeller, which appears in drawings (e and f). Kang *et al*. [31] investigated the flow inside NASA Large Scale Centrifugal Compressor (LSCC) impeller. Figure 2.7 shows his schematic drawing for the centrifugal impeller passage vortices. As shown in this figure vortices are generated at the suction and pressure surfaces also at the hub and shroud surfaces.
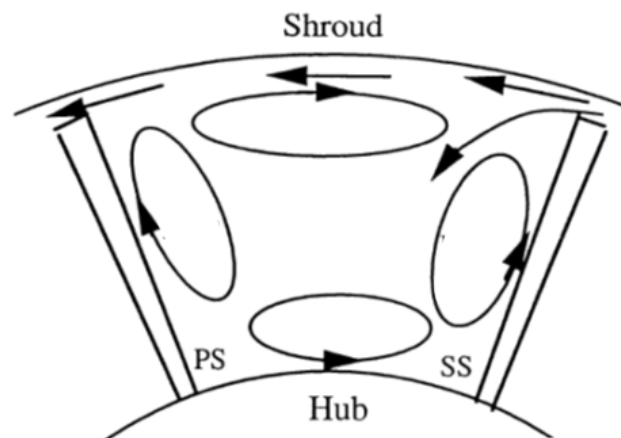
Figure 2.7: Impeller passage vortices [31]

Figure 2.8 shows static pressure contours on the suction and pressure surfaces for NASA LSCC. These contours describe the creation of the vortices inside the impeller passage. For both the suction and pressure surfaces of the blade it can be noticed that the pressure gradient points from hub to shroud; this pressure difference drives the low energy fluid from hub to shroud to generate the blade vortices as shown in figure 2.7.
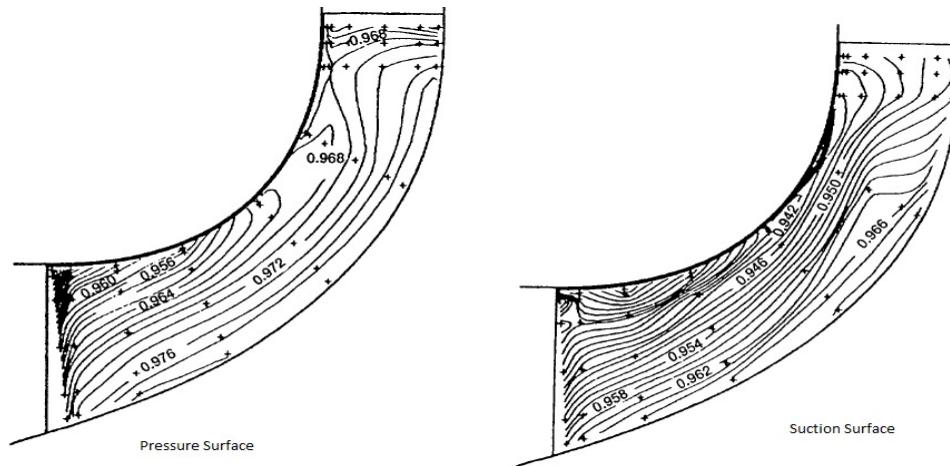
Figure 2.8: Experimental static pressure contours on blade pressure and suction surfaces for NASA LSCC operating at design point [31]

It can also be noticed that the pressure gradient at the suction surface is greater than the pressure gradient at the pressure surface, which indicates that the vortices at the suction surface are stronger than those at the pressure surface; however the tip leakage flow from the pressure surface toward suction the surface energise the suction surface vortices. Figure 2.8 indicates that there is a pressure gradient along the hub and shroud surfaces pointing toward the suction surface, and this pressure gradient with the help of the centrifugal force creates the hub and shroud vortices shown in figure 2.7.

Anish *et al*. [26] explored the flow inside a centrifugal compressor impeller numerically. Figure 2.9 shows the stream lines in his impeller passage. From the figure one can notice the movement of the fluid from hub to shroud on the suction and pressure surfaces. Fluid leaks from pressure side of the blade to the suction side through the tip clearance gap, and the flow that passes through the gap has a high velocity. The leaked flow interacts with the low momentum fluid coming from the hub which reinforces the suction vortices. Because of the pressure difference between the suction and pressure surfaces, a pressure equalization flow moves from pressure side towards the suction side, which pushes the low momentum fluid back to the impeller causing loss called the recirculation loss.

27
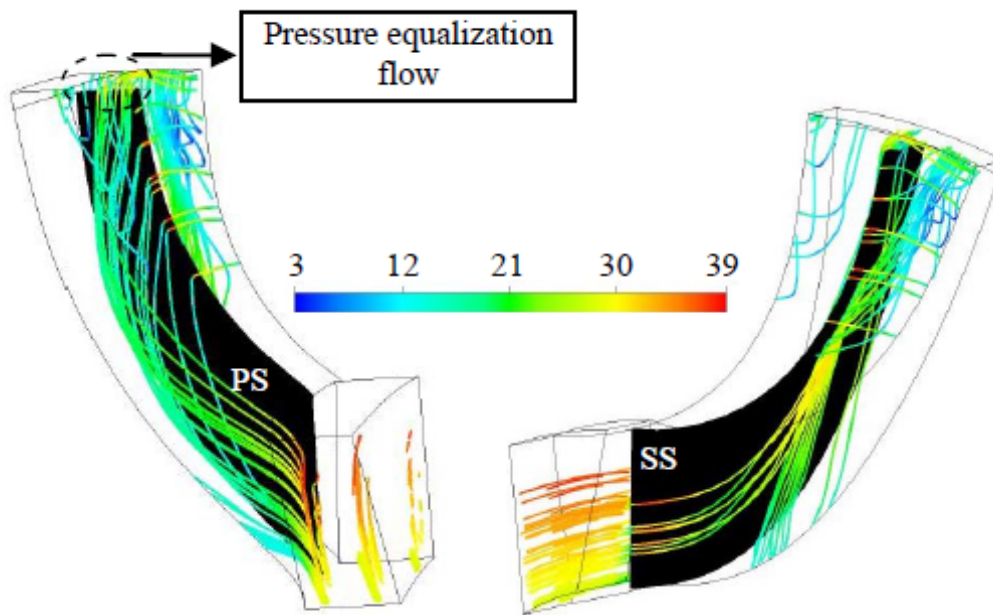
Figure 2.9: Streamlines inside centrifugal compressor impeller [26]

2.2 Radial Inflow Turbines

A radial inflow turbine is a work producing machine that consists of moving and stationary parts namely: stator and rotor (figure 2.10). The stator normally consists of a volute and Nozzle Guide Vanes (NGVs). The volute receives the hot gas from the burner (or the receiver in the solar MGT), distributes the flow uniformly around the rotor and gives it some swirl before it enters the rotor. To accelerate the flow after the volute and maintain the right incidence angle at the rotor inlet, NGVs may be added after the volute. [32]. It is worth to mention here that in turbocharger turbines the pressure ratio is relatively low and the capital cost, weight and size are the highest priorities, therefore the vanes are usually omitted; however, this reduces the design point efficiency conditions but gives better off-design performance. In recent turbochargers, variable angle vanes have been employed and the vanes angle changes following load variations so that better efficiency can be achieved at both design and off-design conditions [6] [33].

The rotor is the beating heart of the turbine, where the energy stored in the flow is converted to mechanical work that can be utilised. Adding a diffuser after the rotor stage, recovers part of the kinetic energy of the exhaust flow, however this increases the size and weight of the machine. Diffusers increase the expansion ratio for turbines that are working over a fixed pressure ratio. However, the diffuser adds a significant portion to the overall size of the turbine which causes difficulties in installation [34].

2.1.1 Turbines Stage Basics

The fluid expands through the turbine components, which occurs ideally in an isentropic process; however, this process cannot be isentropic as result of losses in turbine components. Referring to figure 2.11, the fluid initially enters the volute with total
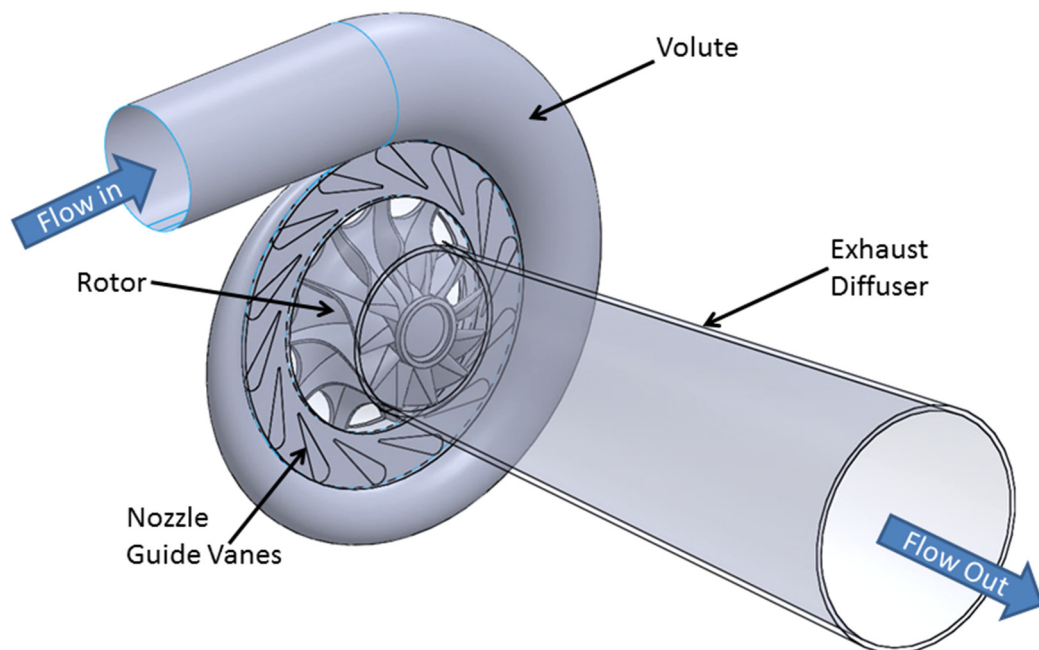
Figure 2.10: Radial turbine components

pressure P_{o0} and total temperature T_{o0} and exits from volute with total pressure P_{o1} and total temperature T_{o1}. The fluid accelerates along the NGVs passages but no work is being transferred so the total temperature at the guide vanes exit, T_{o2} is still the same

as T_{o1}. For ideal nozzle guide vanes, the total pressure at vanes' exit P_{o2} would equal P_{o1}; but for real guide vanes there would be a small pressure drop across the vanes and it can be calculated empirically using stator loss coefficient or by assuming nozzle efficiency.
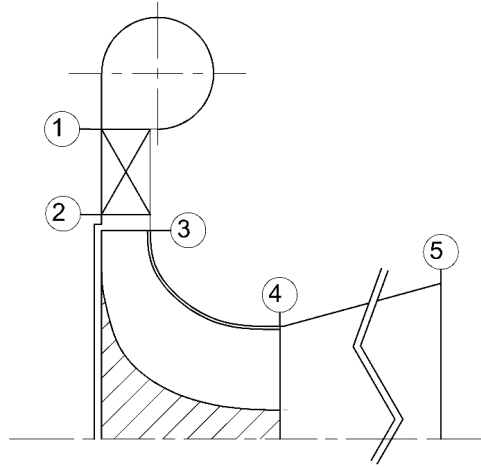
Figure 2.11: Radial turbine schematic

The focus now will be directed towards analysing the rotor stage which is the most important part of the turbine as the work is extracted there. Figure (2.12a) shows the velocity triangle of the fluid at the rotor inlet and figure (2.12b) shows the velocity triangle at rotor exit. Based on Euler turbomachinery equation; the torque and the specific power output from the rotor can be calculated as follows:

$$\tau = \dot{m}(r_3 C_{\theta 3} - r_4 C_{\theta 4}) \qquad (2.20)$$

$$\dot{W} = \dot{m}(U_3 C_{\theta 3} - U_4 C_{\theta 4}) \qquad (2.21)$$
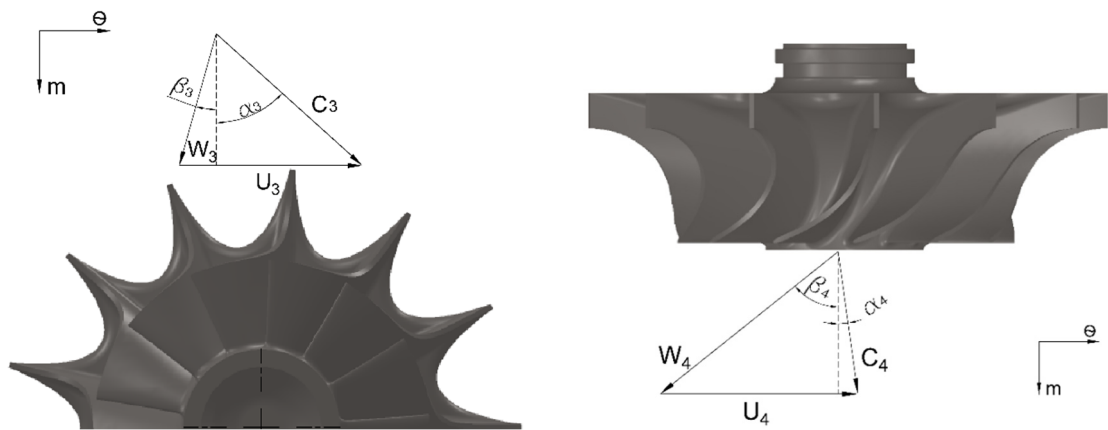
Figure 2.12: (a) Velocity triangle at rotor inlet, (b) Mean velocity triangle at rotor exit.

The symbols C_θ stands for the tangential component of the absolute flow velocity, r_3 is the rotor inlet radius and r_4 is the rotor exit radius defined at the root mean square (rms) value of the tip and the hub radii of the blades. By applying the energy equation on the adiabatic flow through the rotor the specific power can be written in terms of total enthalpy change.

$$\dot{W} = \dot{m}(h_{o3} - h_{o4}) \tag{2.22}$$

Where: h_{o3} and h_{o4} are the total enthalpies of the flow at rotor inlet and exit respectively. And by combining the equations 2.21 and 2.22 the temperature ratio across the rotor can be written as:

$$\frac{T_{o3}}{T_{o4}} = 1 + \frac{1}{c_p T_{o4}}(U_3 C_{\theta 3} - U_4 C_{\theta 4}) \tag{2.23}$$

To calculate the pressure ratio across the rotor the losses that occur in the rotor must be known, a simpler way to calculate the pressure ratio is to assume an efficiency for the rotor, then the pressure ratio can be calculated as follows:

$$\left(\frac{P_{o3}}{P_{o4}}\right)^{\frac{\gamma-1}{\gamma}} = 1 + \frac{1}{c_p T_{o4}}\eta_{tt}(U_3 C_{\theta 3} - U_4 C_{\theta 4}) \tag{2.24}$$

To calculate the pressure ratio for the whole stage, equation 2.24 can be used by replacing the stage total efficiency instead of defining rotor efficiency.

Thermodynamically, turbine efficiency is defined as the output shaft work to the ideal work that can be extracted using an ideal machine. For radial turbines without exhaust gas recovery, like turbocharger turbines, the exit static state is used to calculate the ideal work in the efficiency. This is known as total to static efficiency, which is described in equation 2.25 in terms of enthalpy change across the turbine stage.

$$\eta_{ts} = \frac{h_{o0} - h_{o4}}{h_{o0} - h_{4s}} \tag{2.25}$$

The total state was not used in this case because the exhaust gas from the turbine is still containing some kinetic energy which would be wasted, therefore using the static state would be more realistic in describing the turbine efficiency. However, adding an exhaust diffuser recovers some this wasted energy, in this case, the total to total efficiency is used to describe the machine performance, where the turbine discharge total state is used to calculate isentropic work as shown in equation 2.26.

$$\eta_{tt} = \frac{h_{o0} - h_{o5}}{h_{o0} - h_{o5s}} \qquad (2.26)$$

2.1.2 Turbine Performance Prediction

To predict the design and off-design performance of the radial turbine, an estimate of the losses must be available. Many one-dimensional loss models have been proposed to predict losses in radial turbines in a similar manner to the centrifugal compressor. This section highlights the loss sources within the radial turbine and describes the correlations developed to predict their contribution to the drop in its performance. Building on this understanding of the different loss sources, an improved performance prediction tools was developed within chapter three which is believed to give more realistic predictions for the turbine performance.

Loss models are one-dimensional correlations based on test data which give an estimate for the losses occurring within the turbine stage. The accuracy of these correlations depends on the test data that these correlations are based on. Loss correlations attempt to break down the losses into categories with each one calculated separately. Separating the losses is not the perfect method as all loss mechanisms are strongly related to each other. NASA has formed basis for loss modelling in radial turbines through the work of Rohlik [35], Wasserbauer and Glassman [36], and Rodgers [37]. Meitner *et al.* [38], Futral *et al.* [39] and Dadone *et al.* [40] who all used different loss models within one dimensional

performance prediction codes, where they compared the results with experimental data for actual machines. Whitefield and Baines [6] surveyed the loss models available for radial turbines and implemented these models in their turbine design code. Baines [41] reviewed NASA loss models and suggested modifications to these models based on test data set for 30 turbines for different applications. Losses in radial turbines mainly related to rotor flow, so, this section describe these losses and the correlations developed to predict their contribution in reducing the turbine efficiency.

Incidence Loss

The flow coming from the stator hits the rotor blades at an angle called the incidence angle, where the optimum performance of the turbine is achieved using a negative angle which will be discussed in the next section. Running the turbine away from the design point causes a deviation in the incidence angle, thus the consumed work to turn the flow from its direction to the optimum angle ($\beta_{3,opt}$) is called the incidence loss. Incidence loss can be simply calculated as an enthalpy change using Glassman and Wasserbauer [36] formula.

$$\Delta h_{inc} = \frac{1}{2} W_3{}^2 \sin^2(\beta_3 - \beta_{3,opt}) \qquad (2.27)$$

Passage Loss

Passage losses accounts for all the losses occurring within the rotor passage. According to Mustafa *et al*. [32] the proper passage loss model should account for losses generated due:

- Secondary flow losses occur due flow complexity in rotor passage.
- Blockage, kinetic energy loss resulting from boundary layer growth and losses caused by flow separation if occurs.
- Friction losses along the rotor passage due fluid viscous force.

33

Wasserbauer and Glassman [36] has proposed a formula to calculate the passage losses based on the kinetic energy of the flow at rotor inlet and exit:

$$\Delta h_{pas} = \frac{1}{2} K (W_3{}^2 \cos^2 \beta_3 + W_4{}^2) \tag{2.28}$$

Where K is a factor that can be determined experimentally, where they claimed getting good results when using K value of 0.3. Baines [41] evaluated this model and showed that it is not adequate to model the losses that occur within the rotor passage. Moreover, he suggested a modified formula that takes into account the friction loss and secondary flow losses. Equation 29 shows his final formula which is based on test data of thirty turbines for different applications.

$$\Delta h_{pas} = K_p \left\{ \left(\frac{L_H}{D_H}\right) + 0.68 \left(1 - \left[\frac{\bar{r_4}}{r_3}\right]^2\right) \frac{\cos \beta_4}{b_4/c} \right\} \frac{1}{2} (W_3{}^2 + W_4{}^2) \tag{2.29}$$

Referring to equation 2.29, there are two terms inside the curly brackets; the first one accounts for friction losses and the second term accounts for secondary losses. Here $\bar{r_4}$ stands for the mean radius at rotor exit and c is the chord length of the blade and can be calculated as follows:

$$c = \frac{Z}{\frac{1}{2}(\tan \beta_3 + \tan \beta_4)} \tag{2.30}$$

L_H is the hydraulic diameter of the rotor passage which can be calculated using equation 2.30.

$$L_H = \frac{\pi}{4} \left\{ \left(Z - \frac{b_3}{2}\right) + \left(r_3 - r_{4t} - \frac{b_4}{2}\right) \right\} \tag{2.31}$$

D_H stands for the hydraulic diameter of the rotor passage and can be calculated using the following relation:

$$D_H = \frac{1}{2} \left\{ \left(\frac{4\pi r_3 b_3}{4\pi r_3 + N_b b_3}\right) + \left(\frac{2\pi (r_{4t}{}^2 - r_{4h}{}^2)}{\pi(r_{4t} - r_{4h}) + N_b b_4}\right) \right\} \tag{2.32}$$

The factor K_p has a value of 0.11 for $\left(\frac{r_3 - r_{4t}}{b_4} > 0.2\right)$ and 0.22 for $\left(\frac{r_3 - r_{4t}}{b_4} < 0.2\right)$.

Tip Clearance Loss

Tip clearance is the gap that exists between the turbine rotor and the casing. This gap is left between the rotor and the casing so that the rotor will not interfere with the casing, as it expands at a faster rate than the casing before reaching the steady state. The recommended tip clearance height is 2-5 % of the local span height, which can be determined by FEM results by applying a thermal load and calculating the expansion of the blades [6].

To study the flow in the tip clearance, Huntsman *et al.* [42] run an experiment to visualise the tip clearance flow for turbine rotor of 1.2m diameter, and rotational speed of 450 rpm. The study divided the flow in the tip gap into three regions; the first region is inducer region (from rotor inlet till 20% blade meridional length), the second one is at the mid passage (from 20-60% of the blade meridional length) and the third one is at the rotor exducer (from 60 until end of the blade) as shown in figure 2.13. From that experiment, it was shown that the flow in the first part was dominated by the scraping fluid which reduces the mass flow at this region.
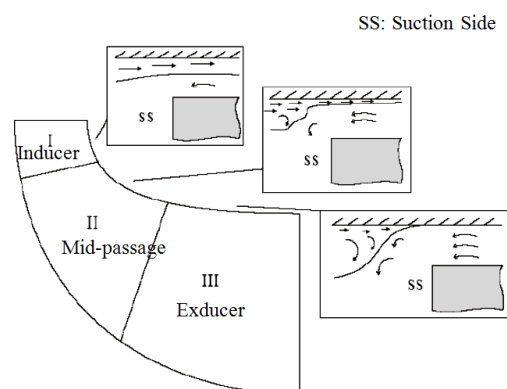
Figure 2.13: Schematic of flow in the tip clearance [43]

Simon [44] has studied the flow through the tip gab numerically and found that the fluid from the rotor inlet till 6% of the blade length moves from suction to pressure side of the blade. In the mid passage, little scraping fluid is dragged through the tip clearance and at

the exducer the dragging effect of the scraping fluid disappears. Deng *et al*. [43] [45] studied the tip clearance flow with different gap heights for 100 kW microturbine numerically. They found that the tip leakage flow is controlled by the pressure difference between the pressure and suction side and the scraping flow driven by the relative motion of the casing. They also, analysed the off-design characteristics of the tip clearance flow and found that reducing the rotational speed and increasing the stage pressure ratio weakening the scraping flow at the inducer and the mid passage but the tip clearance flow at exducer region is less sensitive to these changes in rotational speed and pressure ratio. Tip clearance loss in radial turbines has been studied for long time. People who tried to model the clearance loss have distinguished between the axial clearance which is at the rotor inlet and the radial clearance at rotor exit as shown in figure 2.14. Most studies reveal that the radial clearance plays a larger role in the rotor losses than the axial clearance. Baines [32] provides a comparison for the effect of increasing the clearance gap on the total performance of the turbine between four authors.
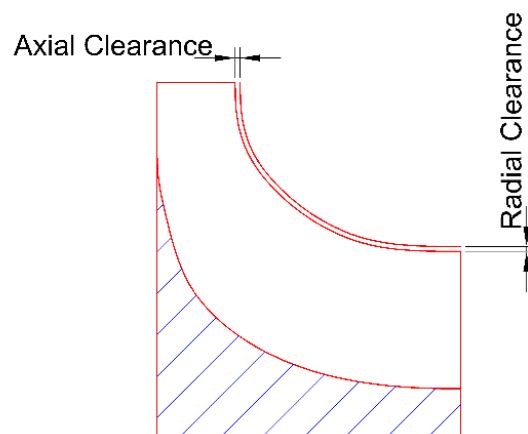
Figure 2.14: Axial and radial clearance terminology

Table 2.1 shows the comparison of these results and it is clear that the radial clearance has a larger effect on the turbine efficiency. Deng *et al*. [45] stated that for each percentage of axial clearance increment will cause an efficiency drop of 0.15% and a drop in the mass flow rate of 0.06%, meanwhile each percentage increase in the radial

clearance reduces the efficiency by 1.27% and 0.24% increment in mass flow rate. Jacob *et al*. [46] showed that the tip clearance contributes in 6-12% of the total turbine loss.

Table 2-1: Comparison between the effects of increasing the tip clearance gap on the total to total efficiency [32]

Percentage change in	Total to total efficiency	
Due to	1% increment in axial clearance gap	1% increment in radial clearance gap
Futural and Holeski (1970)	0.15	1.6
Ricardo (1957)	0.2	0.5
Ishimo *et al.* (1991)	0.2	1.2
Krylov and Spunde (1963)	0.1	0.6

An early model for the clearance loss was set by Rodgers [47], this model expresses the effect of tip clearance as a deficiency in the turbine performance. Based on the radial clearance ε_r the decrement in total to total efficiency can be calculated according to Rodgers as follows:

$$\Delta\eta_{tt} = 0.1 \frac{\varepsilon_r}{b_3} \tag{2.33}$$
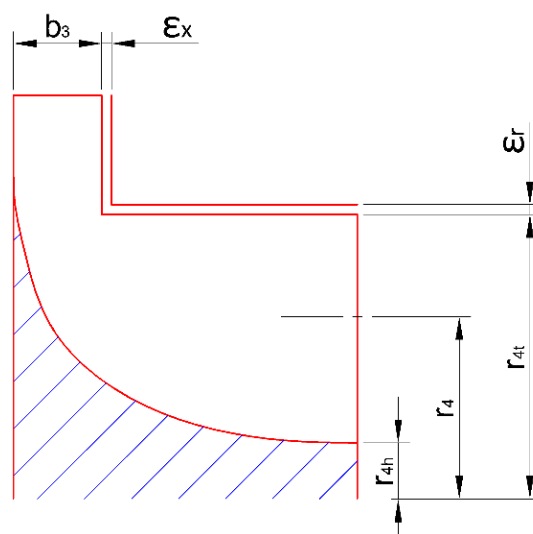
Figure 2.15: Simplified tip clearance model

Later Baines [41] developed a model for tip clearance losses which includes the effect of axial clearance. In this model, he assumed a simplified model for tip clearance as shown in figure 2.15. The enthalpy drop according to his model can be calculated as follows:

$$\Delta h_{cl} = \frac{U_3{}^2 N_b}{8\pi} \left[K_x \varepsilon_x C_x + K_r \varepsilon_r C_r + K_{xr} \sqrt{\varepsilon_r \varepsilon_x C_r C_x} \right] \qquad (2.34)$$

Where K_r and K_x are the discharge coefficients for the radial and axial parts of the rotor and coefficients C_x and C_r can be gained from equations 2.35 and 2.36.

$$C_x = \frac{1 - \left(\frac{r_{4t}}{r_3}\right)}{C_{m3} b_3} \qquad (2.35)$$

$$C_r = \left(\frac{r_{4t}}{r_3}\right) \frac{Z - b_3}{C_{m4} r_4 b_4} \qquad (2.36)$$

Because of the strong interaction between the effects of the radial and the axial clearance, Baines added a cross coupling factor K_{xr} to account for this interaction in the loss formula. This form showed a good agreement with test data for $K_x = 0.4$, $K_r = 0.75$ and $K_{xr} = -0.3$.

All the suggested models account for kinetic energy loss from the leaked fluid across the tip clearance gap. However, the friction along the blades tips and the contribution in the secondary flow generation within the rotor passage have not been modelled yet within the available clearance loss models.

Windage (Disk Friction) Loss

Part of the fluid that enter the turbine leaks into the space between the back face of the rotor and the turbine casing. Because of the viscous forces of the fluid between the rotor back face and the casing this causes a friction loss. One of the most widely used formulas to account for this loss was derived by Whitefield and Baines [6] (equation 2.13) where Reynolds number used in the equation can be determined using equation 2.16.

Scalloping loss

Scalloping is a method used to reduce the mass and the inertia of the turbine rotor, as well as reducing the stresses at the point of contact between the back face of the rotor and the rotating shaft. Scalloping is the operation of removing material between the rotor blades at rotor inlet as shown in figure 2.16. The degree of removing material depends on the Finite Element Analysis (FEA) results.
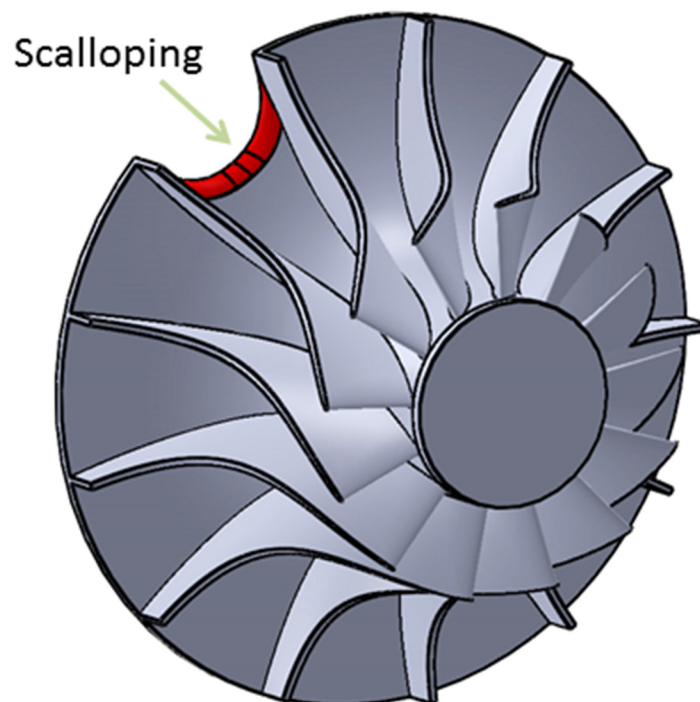
Figure 2.16: Rotor scalloping

Hiett *et al*. [48] studied the effect of four different types of scalloping on the performance of the radial turbine performance. Figure 2.17 shows rotors used in the test. The research results revealed that scalloping of rotors (a) and (b) had no effect on the performance of the turbine. However, scalloping the rotor (c) caused a drop in the performance of the turbine of 4 percent and the scalloping of the rotor (d) has decreased the efficiency by 2 percent. This study related the drop in the efficiency to the degree at which scalloping affects the flow path, thus, in rotor (a) and (b), scalloping hasn't affected the flow path but in case (c) and d the flow path was affected by the scalloping.
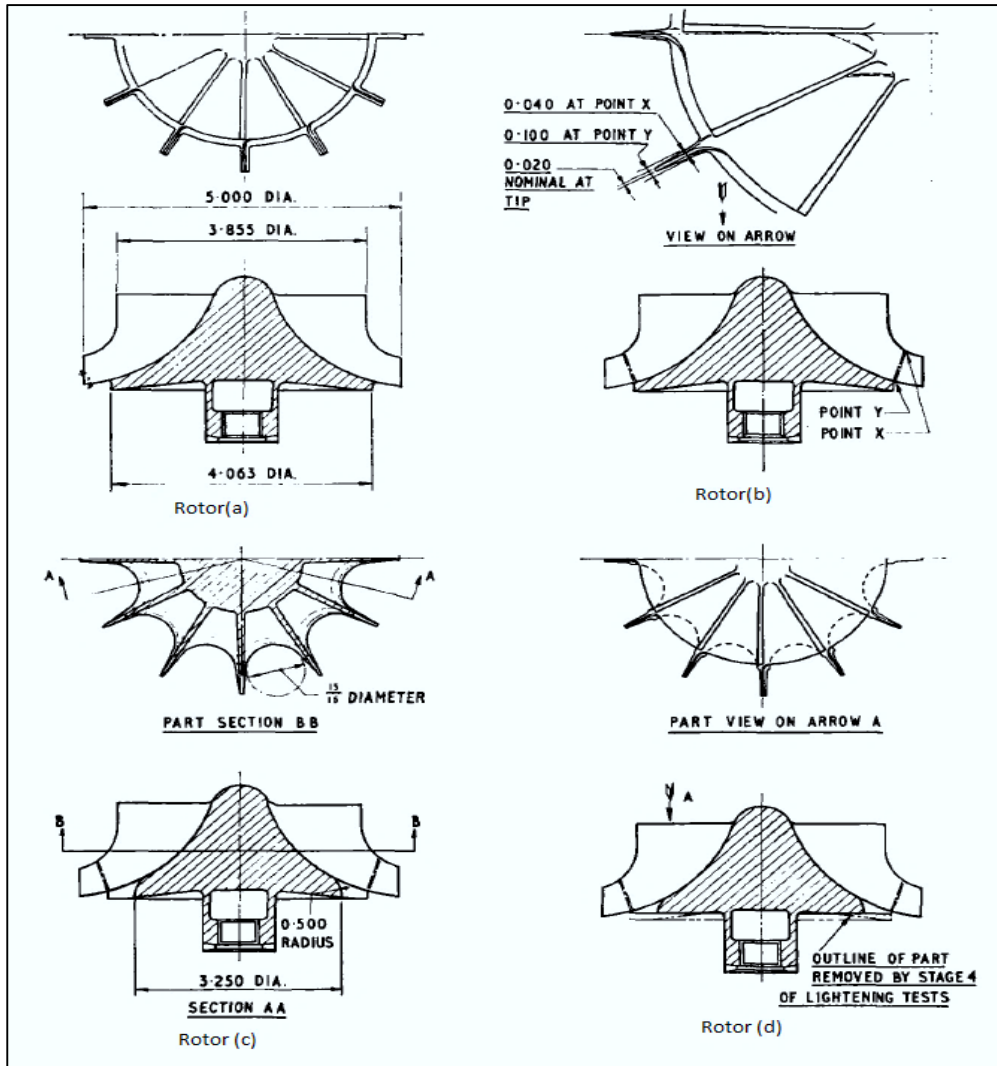
Figure 2.17: Different types of scalloping from Hiett and Johnston experiment [48]

Tamaki *et al.* [49] studied the effect of scalloping on the turbine performance experimentally and numerically using CFD. This study showed that the efficiency drop due to a shallow scalloping for the turbine shown in figure 2.18, was about one percent.
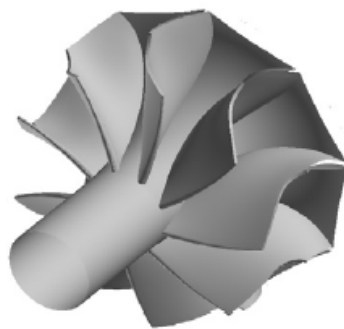
Figure 2.18: Shallow scalloping from Tamaki *et al.* experiment [49]

2.1.3 Flow Features within the Rotor Passages

Studying the flow in radial turbines started in the middle of the 20th century [33], in which it was hoped that an improved understanding of the flow process in these machines will lead to a better design for them. The flow within the rotor passages has been studied using experimental measurements and CFD simulations. However, the experimental studies for the flow within small machines are scarce as the measuring instruments are of low response and can only provide a circumferentially average data which cannot describe the flow variations in these high-speed turbines properly. The size of these small machines is another obstacle for experiments. The use of Laser Doppler Velocity meter (LDV) is more complicated in radial turbines because of the high temperature inlet flow and the difficulty of introducing optical access [50]. This section provides a description of the flow within the rotor passages based on the previous work available in literature.

The flow leaves the NGVs with both radial and tangential components. Some earlier designs used a pure radial flow at the rotor inlet to achieve the best performance. However, more recent studies showed that the optimum incidence angle lies in the range between -20∘ to -40∘ [6]. Experiments completed by Yeo and Baines [51] showed that an incidence angle of -30∘ is the optimum angle, where the turbine efficiency is the maximum. Woolley and Hatton [52] studied the effect of changing the incidence angle using radial inflow turbine with water as fluid. Figure 2.19 shows results gained from their experiments which show that -40∘ is the optimum incidence angle, which prevents flow separation within the passage. Kitson [53] reached the same result while he was studying the effect of the incidence angle on turbines working with compressible fluid.

As the flow travels radially down, the secondary flows start to take part in the flow in the form of circulations that rotate in a direction opposite to the direction of rotor rotation. These secondary flows are generated by two mechanisms [32]. The first one is that when

the flow moves radially inside the rotor, the blade speed U, referring to the velocity triangle at rotor inlet in figure 2.12a, decreases at a rate greater than the decrement of the tangential component of the absolute flow velocity. This decrement in the blade velocity causes the relative velocity vector to move toward the direction of the absolute velocity vector (toward pressure surface).
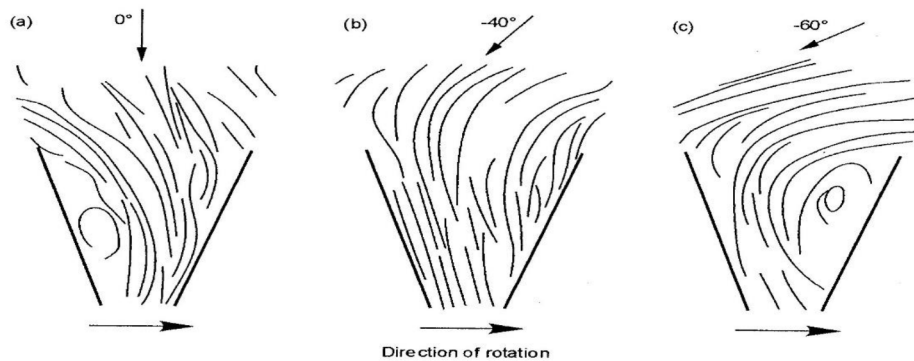
Figure 2.19: Flow baths for different incidence angle (a) zero incidence angle (b) -40◦ incidence angle (c) -60◦ incidence angle [32]

The second mechanism is Coriolis forces that results from Coriolis acceleration. Therefore, if the incidence angle were negatively large, the secondary flows would also be large and cause the flow to separate the from pressure surface, and if the incidence angle was nearly zero or positive, the flow will tend to separate from the suction surface. In the range of optimum incidence angles the secondary flow circulations are minimised and the flow does not separate, which results in lower losses and better turbine performance.

Dai *et al.* [50] used Laser Doppler Velocimetry (LDV) measurements to get the flow pattern within the rotor passages. For incidence angle of -44◦, figure 2.20 shows the results for the relative flow angle variation along the flow bath. Secondary flows can be noticed clearly at 20% and even in 40% of the chord length where the flow still moves radially into the rotor. As the flow reaches the exit of the rotor, the flow predominantly moves in axial and tangential directions. The flow faces a high turning in the tangential direction near the trailing edge of the rotor as shown in figure 2.20d. As a result of this

tangential movement, Coriolis acceleration and the cross-passage acceleration act on the low momentum fluid causing it to move from pressure to suction surfaces and from the hub to shroud.

Huntsman [54] studied the flow along the rotor surface of a low speed turbine using surface mounted hot-film anemometer. Figure 2.21 shows the flow along suction and pressure surfaces. It is obvious that the flow at suction surface tend to move to the shroud surface but the fluid on the pressure surface is moving in the stream-wise direction. The fluid moving toward the shroud on the suction surface meets the fluid leaks from the pressure side of the blade to generate a vortex in the corner between the suction surface and the shroud.

(S.S.): suction surface

(P.S.): pressure surface

(a) 20% chord   (b) 40% chord   (c) 70% chord   (d) 96% chord
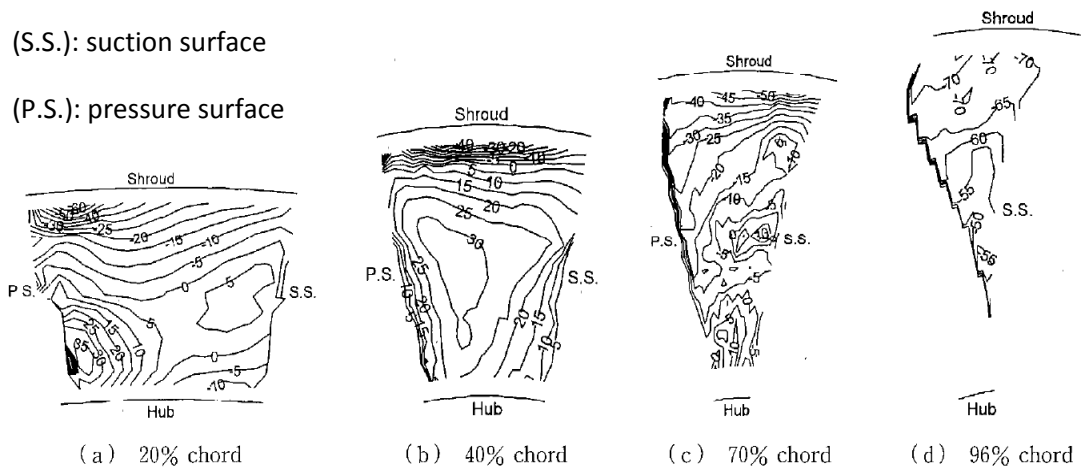
Figure 2.20: Relative flow angle β at (a) at 20%, (b) 40% (c) 70% (d) 96% of the chord length [50]
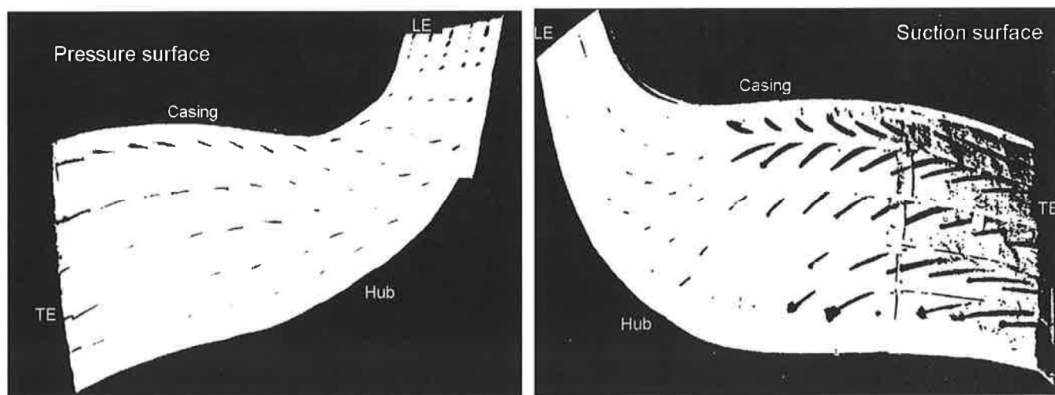
Figure 2.21: Flow visualization at rotor blade surface for low speed turbine [54]

Deng *et al.* [55] analysed the flow inside a turbine running at 60000 RPM and power rating of 100 kWe using CFD. Figure 2.22 shows the flow baths along the suction and pressure surfaces, it can be noticed that the results are similar to huntsman's results shown in figure 2.21.

(a)   (b)
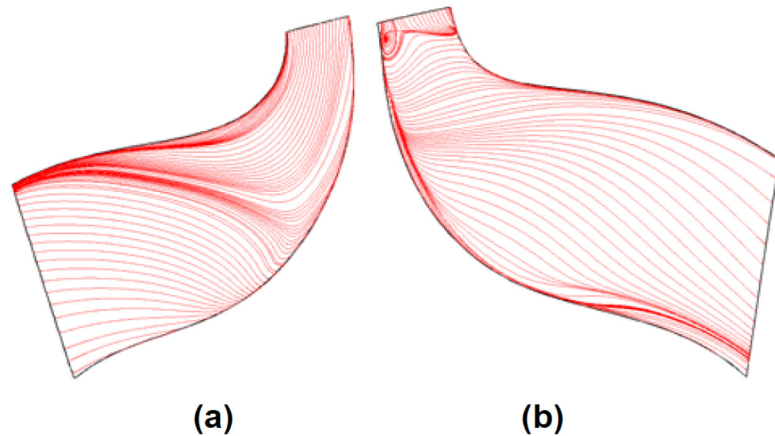
Figure 2.22: Flow visualization at rotor blade surfaces for high speed turbine using CFD (a) suction surface, (b) pressure surface [55]

Figure 2.23 shows the static pressure distribution at the hub, mid-span and shroud along the pressure and suction surfaces for the same turbine. It can be can be noticed that at the last portion of the suction surface the static pressure at hub is greater than the static pressure at mid span and shroud. However, at the same location of the pressure surface, the static pressure at shroud is greater along the blade surface. This pressure difference, confirms the movement of the flow toward the shroud at the suction surface.
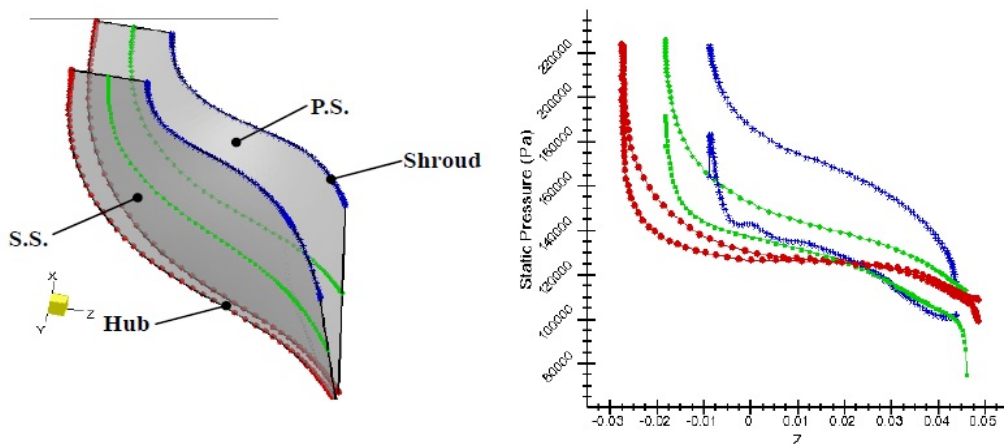
Figure 2.23: Static pressure distribution at hub, mid-span and shroud along pressure and suction surfaces of radial turbine [55]

Conclusions

Mean line methods can be used to predict off-design as well as design point performance for the radial turbomachines using the loss correlations available in literature. Studying the off-design performance is not important in the case of fuel powered gas turbines as they usually operate on the design point. However it becomes more critical in solar powered MGTs because of solar irradiation fluctuations. Using mean line methods has the advantage of being fast whilst needing only a small amount of information regarding the turbomachine geometry. However, the accuracy of these methods is not high as they break down the highly-interlinked loss mechanisms into simpler forms to be able to model it. Also, the one-dimensional methods cannot estimate the losses and the efficiency of the individual component accurately as the flow within those machines is highly three-dimensional. Moreover, parts of the loss correlations are based on ideal gas assumptions, which introduces uncertainties when the behaviour of the working fluid deviates from that of an ideal gas. Within this research, CFD should be used to predict the performance of the turbine and compressor, and then the results could be refined by including some of the one-dimensional loss correlations to improve the predictions accuracy. This method will be applied to the turbine and the compressor of the solar powered MGT, which then will be built and tested to validate the performance results.

The secondary flows within the turbine rotor passages has been addressed by many authors, however, there was no attempt to implement end wall features to reduce their effects on the aerodynamic performance of the turbine. By exploring the literature (refer to section 6.2), it has been found that implementing riblets into the walls of the curved ducts and axial turbomachines can reduce the secondary flow within their passages. Therefore, CFD will be used to test the ability of riblets with different geometries and

configurations implemented to the rotor hub surface to reduce the secondary flows and

improve the turbine performance.

Chapter 3

3. Centrifugal Compressor Design

3.1 Introduction

A methodology for a centrifugal compressor design is presented in this chapter, which was used to design a compressor for a 6 kWe solar powered MGT. A meanline methodology was used to calculate the main geometric parameters for the compressor components which subsequently were used to generate their three-dimensional geometries. Computational Fluid Dynamics (CFD) was used to fine tune those components to achieve better performance.

As highlighted in the previous chapter the CFD analysis does not account for all sources of loss in the radial turbomachines, which subsequently affects the accuracy of the performance predictions for such machines. The novel contribution of this work is the consideration of the losses that are not accounted in the CFD analysis in the performance map generation for the compressor. Hence, this chapter is aiming at improving the accuracy of predicting the compressor performance by using one dimensional correlations to improve the CFD results.

3.2 Compressor Design

The compressor design procedure starts with the meanline design for the compressor components which is then followed by the geometry generation using meanline calculation outputs. The performance of the parts is then analysed using the CFD tools and based on the results the geometry is modified to reach the desired performance. The design starts by implementing the thermodynamic properties of the working fluid entering the compressor and the expected performance of the compressor in the preliminary design program. Based on these parameters and the performance parameters available in the literature; the appropriate thermodynamic and fluid dynamic conservation principles are applied within the preliminary design process to obtain the following:

- The main geometric parameters of components such as the mean radii, blade height and blade angles at inlet and outlet of the impeller wheel.
- Thermodynamic quantities at the inlet and outlet of each component.
- Flow velocities at the defined stations.

Using those outputs, the geometry of each component can be built. For each component, CFD is used to study the flow behaviour during the operation which indicates the required modifications on the compressor geometry to get an aerodynamically satisfactory design. Kalogeropoulos [56] summarised the criteria for achieving a good compressor design in the following:

- No abrupt change in the flow passage area.
- Incidence angle at the impeller inlet should be similar or within narrow range of deviation with blade leading edge angle.
- Back flows should be avoided especially when boundary layer is thick.
- No sudden change in the blade loading should occur along the flow passage.

- Local acceleration or deceleration of the flow must be avoided.

3.3 Meanline Design

As previously described, the meanline design is a good approach to get a quick estimate for the turbomachine design using small amount of information regarding the turbomachine geometry. To perform the preliminary design for the compressor a MatLab based program has been built. Two sets of data should be fed to the design program. The first set includes the operating conditions and required flow properties to be delivered by the compressor. The proposed design procedure requires the following set of values for the operating conditions and the output requirements of the compressor.

- Compressor intake total temperature.
- Compressor intake total pressure.
- Mass flow rate.
- Total pressure ratio of the compressor stage.
- Shaft speed.

The second set comprises empirical relations that are combination of performance and dimensionless ratios available in the literature. Based on the given data; the design starts with the impeller then the diffuser and finally the volute. In the next sub sections the design procedure is explained for those components.

3.3.1 Impeller Design

Figure 3.1 shows a schematic for a centrifugal compressor stage. The design procedure starts from the impeller inducer (point 0). A proper inducer design is the key to achieve a high-performance impeller, so the design should ensure that losses are reduced to the minimum [18].
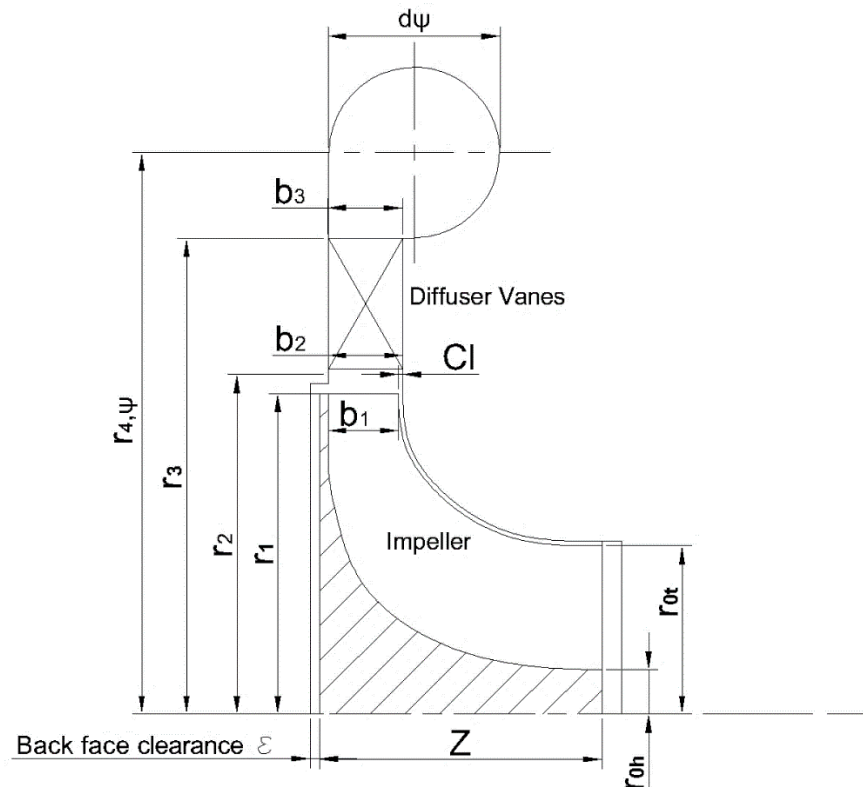
Figure 3.1: Centrifugal compressor schematic

The following design procedure aims at reducing the inlet tip relative velocity to minimise the inlet relative kinetic energy of the flow which will reduce the incidence losses at the inducer.

Inducer Design

Inducer design is an iterative process that aims at achieving the best geometry with the lowest amount of losses. Referring to the block diagram in figure A.1 (Appendix A), the process starts by allocating a small value for the absolute flow velocity at impeller tip. The terminating condition of this loop is to achieve a predefined Mach number. Impeller rotation creates suction pressure at the inducer which leads to accelerate the fluid approaching the leading edge, therefore reaching high Mach number is expected. A predefining Mach number gives assurance that shock losses are avoided, moreover shocks could lead to boundary layer separation through impeller passage.

Using the absolute velocity value and assuming that the flow enters the inducer axially as no pre-swirlers are used, the static temperature, pressure and the density of the working fluid can be calculated. Japikse [18] calculated the inducer area by introducing a blockage factor (B) to compensate the blockage due boundary layer as follows:

$$A_1 = \frac{\dot{m}}{\rho_1 C_{m1}(1 - B)} \qquad (3.1)$$

The inducer passage is the doughnut area is limited by the hub and the tip radii, so the tip radius can be calculated if the hub radius is known. Usually the hub radius is defined based on the gas turbine shaft diameter and configuration. Using the tip radius, the blade speed can be calculated and so the relative velocity. Impeller blades at inducer are radially fibered to withstand the high bending stresses, therefore the velocity triangle (figure 3.2) can now be defined at any point along the span. By fully defining the velocity triangle and the thermal properties, Mach number can be estimated. All the previous calculations will be performed with a new higher absolute velocity if the calculated Mach number is greater than the pre-set value. After finishing this loop, the design process moves to the exducer design of the impeller (point 1, figure 3.1).

Exducer Design

Referring to the block diagram in figure A.2, the components of the velocity triangle at exducer discharge (figure 3.3) can be resolved by knowing the impeller total isentropic efficiency, impeller discharge diameter, blade back sweep angle and the number of rotor blades. Kalogeropoulos [56] and Rodgers [5] reported achieving 90% total efficiency for small compressor impeller, for this reason assuming an efficiency of 90% is reasonable for the impeller design.
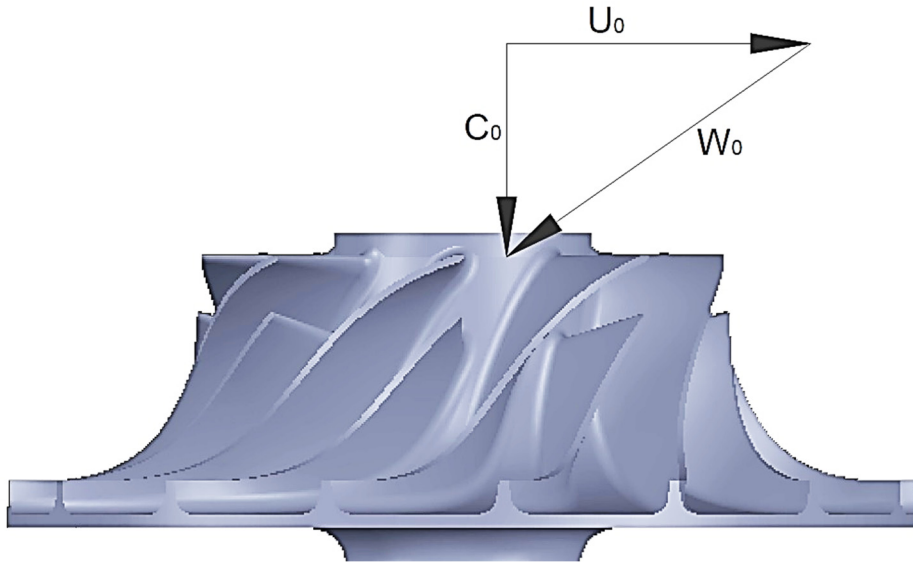
Figure 3.2: Inducer velocity triangle

The design procedure was constructed such that the compressor is part of a gas turbine, so the design of the compressor should match the turbine design. Aungier [34] used the specific speed as the matching criteria between turbine and compressor.

$$N_{s(comp)} = 1.25 N_{s(turbine)} \qquad (3.2)$$

Rodgers [57] suggested another matching criterion for gas turbine applications where the compressor impeller exit diameter must be around 0.87 times the turbine rotor inlet diameter. For exducer design, the second matching criterion was used as turbine rotor diameter is fixed based on turbine design procedure followed. The impeller back sweep angle is beneficial for the compressor performance, Whitefield *et al.* [6] summarised those advantages as:

- Causing a drop in the absolute flow velocity, which in turn increases the static pressure and reduces the absolute Mach number.

- Stabilising the operating range by increasing the negative gradient of the required work input.

- Reducing the blade loading along impeller passage which reduce secondary flow generation.
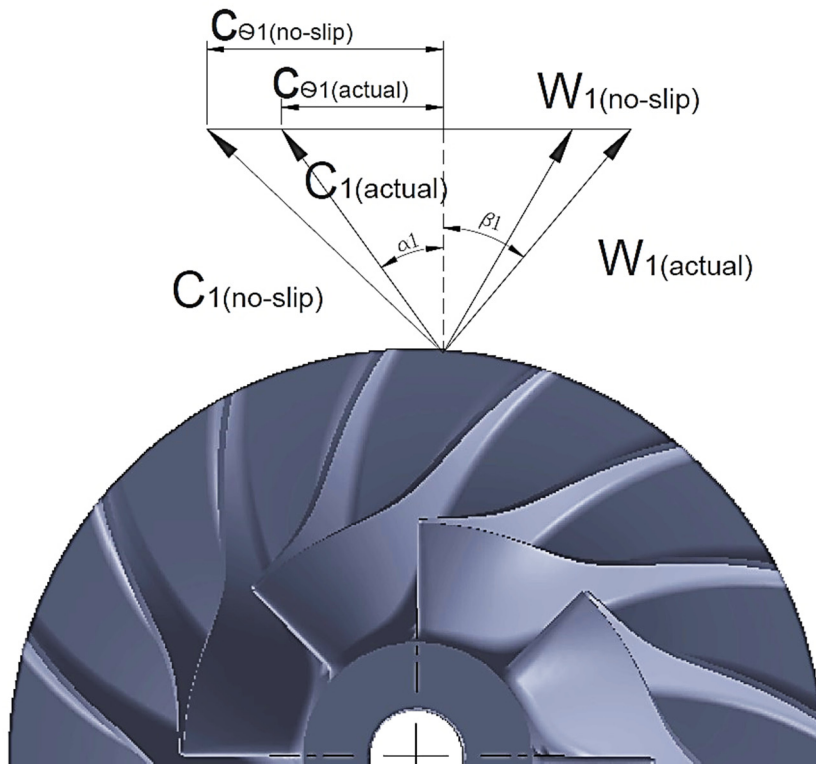
Figure 3.3: Exducer velocity triangle

In the literature, no optimum value for the blade back sweep angle was reported, however, stress considerations limit it, as increasing its value increases bending stresses on the blades. A value of $-30°$ was chosen as high stresses are expected because of the high rotational velocity.

The impeller blade number is a crucial design parameter, as small number of blades leads to higher blade loading which in turn increases secondary flow formation and could lead to boundary layer separation. On the other hand, a large number of blades increases blockage and friction losses as contact surface area increased. Rodgers [58] studied the effect of changing blade numbers on impeller performance and found that for impeller with a specific speed in the range 0.5-1.5 the optimum blade number ranges from 12-16. Getting the impeller design finalised, the diffuser design can be established to gain the required diffusion of the flow leaving the impeller.

53

3.3.2 Diffuser Design

The flow exits the impeller wheel with a high kinetic energy which can reach up to 40 percent of the input work [18]. To utilise this energy a proper diffuser has to be used after the impeller stage. Vaned and vaneless diffusers are commonly used in centrifugal compressors. Vaned diffusers consist of two parallel walls or pinched from one side or both. Flow in the vanless space is a free vortex where the angular momentum of the fluid is conserved, therefore, the radius ratio of the diffuser can be calculated by applying mass and angular momentum conservation between diffuser inlet and outlet.

$$r_1 C_{\theta 1} = r_2 C_{\theta 2} \qquad\qquad (3.3)$$

$$\rho_1 C_{m1} A_1 = \rho_2 C_{m2} A_2 \qquad\qquad (3.4)$$

Vaneless diffusers suffer from the low recovery coefficient RC (equation 4.31) and the long passage length required to achieve the desired pressure recovery. The use of a vaned diffuser instead improves the pressure recovery where pressure recovery of 0.7 or higher can be achieved with smaller size [6]. A channel diffuser has been chosen for this application as it has a high pressure recovery coefficient and it is easy to manufacture. Referring to figure 3.4, the channel diffuser is characterised using the following geometric parameters:

- Leading edge radius ratio (r_2/r_1)
- Ratio of the diffuser throat width to height $(AS = b_2/W_2)$
- Incidence angle, which is defined as the angle between the diffuser suction surface and the absolute flow angle.
- Number of vanes
- Diffuser outlet to inlet area ratio $(AR = A_3/A_2)$
- Ratio of the length of the diffuser channel to its throat width $(LWR = L/W_2)$

- Divergence angle ($2\emptyset$)
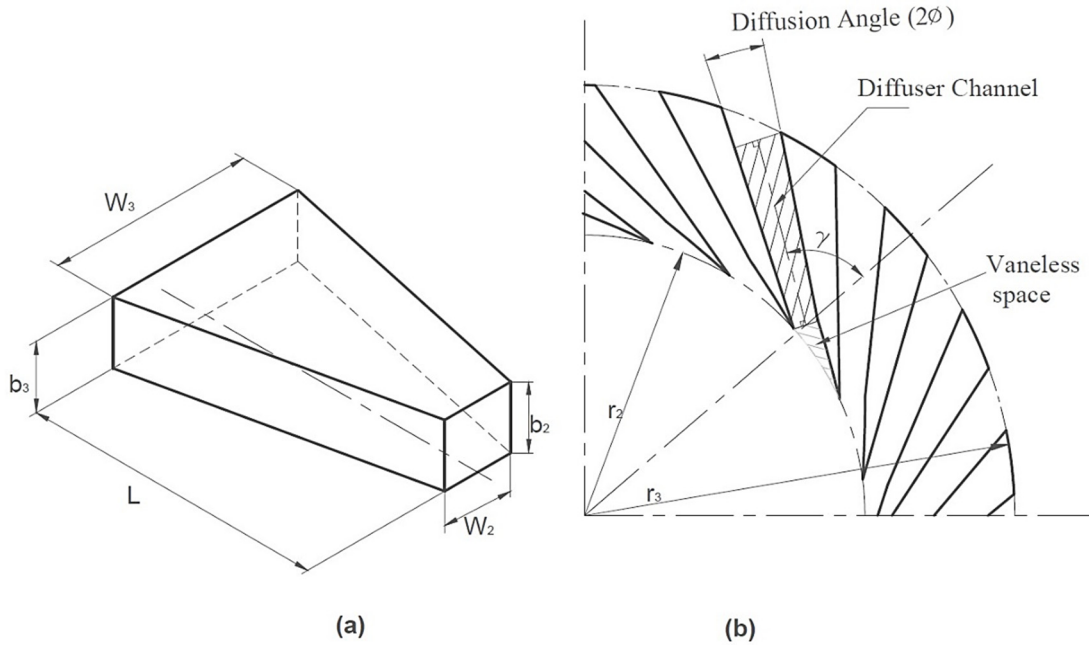
Figure 3.4: Diffuser schematic, (a) channel diffuser passage, (b) diffuser schematic

The starting point in channel diffuser design is finding the optimum radius for the diffuser vanes leading edge. A small gap between impeller blades and diffuser leading edge creates more noise, induces higher stresses on the impeller blades, increases the back pressure effects on the flow within the impeller passage and leads to getting high Mach number at the diffuser vane's leading edge. On the other hand, a large gap results in increasing the boundary layer blockage, therefore the leading edge radius ratio (r_2/r_1) selection would be a trade-off between boundary layer blockage and Mach number [59, 6]. Rodgers [60] tested a channel diffuser with a constant throat area and different radius ratios 1.035, 1.125, 1.1215 and 1.18 to find the optimum diffuser leading edge radius ratio. From his tests, the best performance was achieved using the radius ratio of 1.125. However, another test performed by Osborne *et al.* [59] showed that best performance for the diffuser can be achieved using radius ratio of 1.05.

Throat aspect ratio is another important parameter that affects the channel diffuser recovery performance. Runstadler *et al*. [61] plotted the relation between diffuser recovery coefficient and its aspect ratio for different boundary layer blockage percentages at diffuser throat. Figure 3.5 indicates that the highest recovery coefficient can be achieved with aspect ratio of 1. The effect of decreasing the aspect ratio to values lower than unity has a greater negative effect on the recovery performance at low blockage, while this effect is almost negligible at high blockage percentage. On the other hand, increasing the aspect ratio has small penalty on performance at lower throat blockage, but this penalty becomes considerable at high blockage.
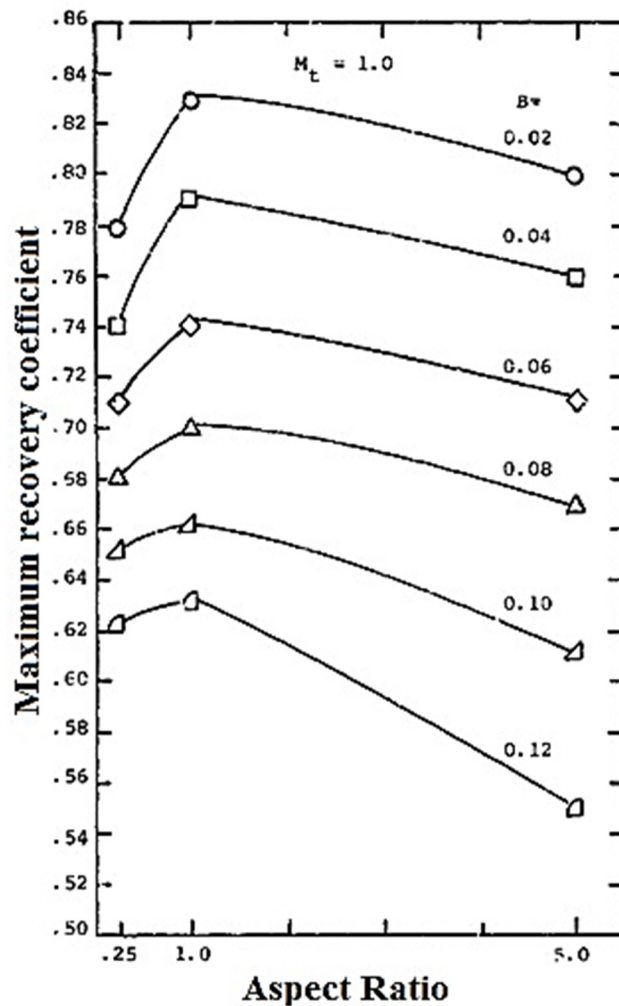
Figure 3.5: Aspect ratio effect and blockage percentage effect on diffuser recovery coefficient [61]

The flow leaving the compressor impeller does not move in a straight line, but rather it follows a spiral curve. Figure 3.6 shows that the optimum recovery coefficient can be achieved when the flow hits the diffuser vanes with a negative angle of around 4º. The number of diffuser vanes has a minor effect on compressor performance. Rodgers [60] tested a compressor with 13 and 21 vanes and found no noticeable change in either compressor performance operating range. Kalogeropoulos [56] recommended using a number of vanes greater than the number of impeller blade and that the number of vanes should be a prime number to avoid impeller blades passing frequency excitation leading to blades' vibration.

To calculate the diffuser channel dimensions, a suitable aspect ratio must be selected. Using the aspect ratio and Mach number values at the impeller discharge; it is possible to use one of the channel's diffusers performance maps to obtain the diffuser channel dimensions.
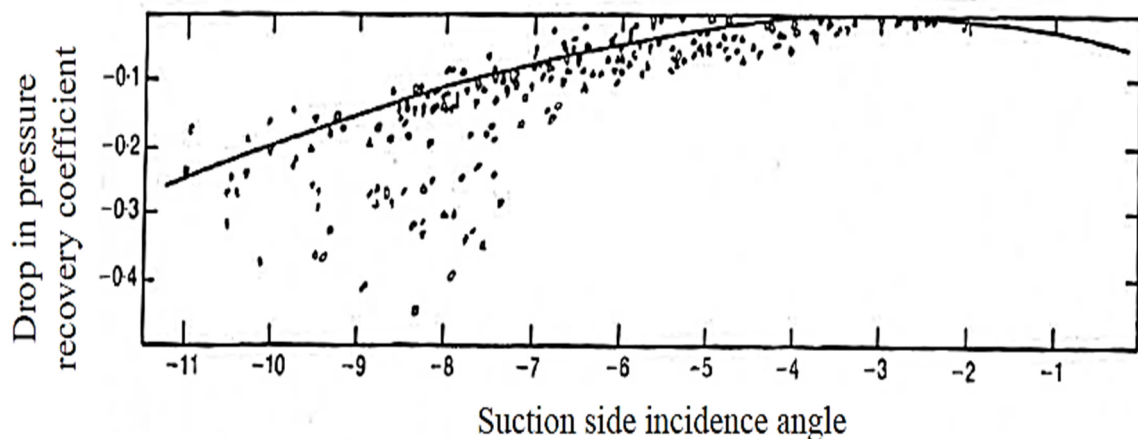
Figure 3.6: Incidence angle effect on diffuser performance [6]

Figure 3.7 shows a channel diffuser map for aspect ratio 1, Mach number 0.8 and blockage of 4%. The channel's diffuser recovery coefficient values are plotted in terms of area and length to width ratios, thus by selecting the desired recovery coefficient and either area ratio or length to width ratio, the channel geometry can be fully defined.

57
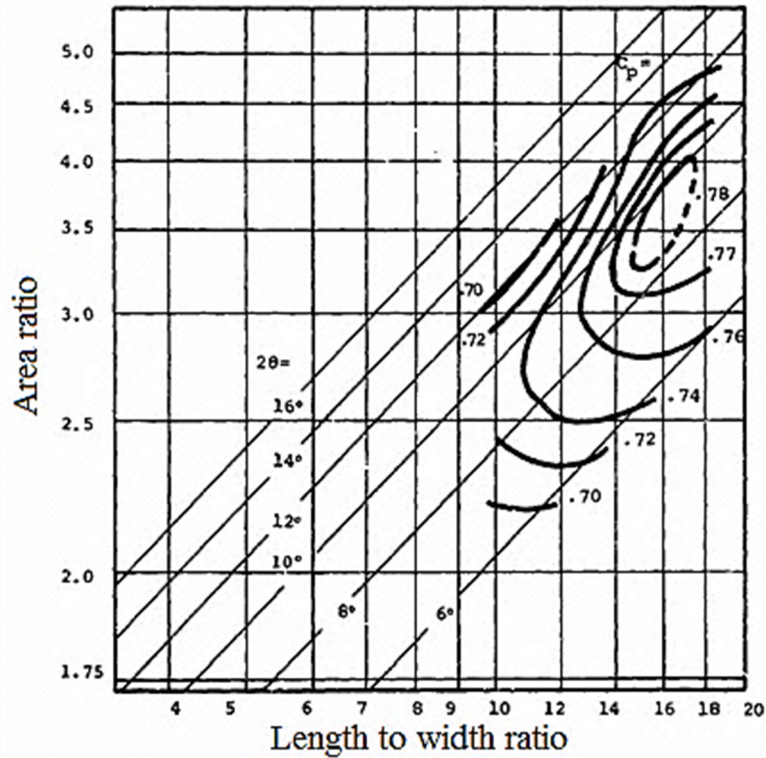
Figure 3.7: Performance map for a channel diffuser of AS=1, Ma= 0.8 and blockage= 4% [61]

3.3.3 Volute Design

The centrifugal compressor volute is an annular passage used to collect the flow and direct it into single pipe. The volute design seeking the cross-sectional area and the distance between cross sectional area and turbine axis. The design method used here assumes that the angular momentum of the flow is conserved between diffuser discharge and volute exit [62].

Considering a small volute element as shown in figure 3.8a, the mass flow increment across this section equals the mass flow entered from the diffuser passage. Knowing that the difference between flow velocity at the diffuser discharge and at volute section centroid is small, the density of the air can be assumed to be constant and the mass flow increment through that section is given as:

$$d(C_{\theta 4\Psi} A_{4\Psi}) = C_{r3} r_3 b_3 d\Psi \qquad (3.5)$$

By integrating both sides from 0 to Ψ the geometric dimensions of the volute section can be estimated.

$$C_{\theta 4\Psi} A_{4\Psi} = C_{r3} r_3 b_3 \Psi \qquad (3.6)$$
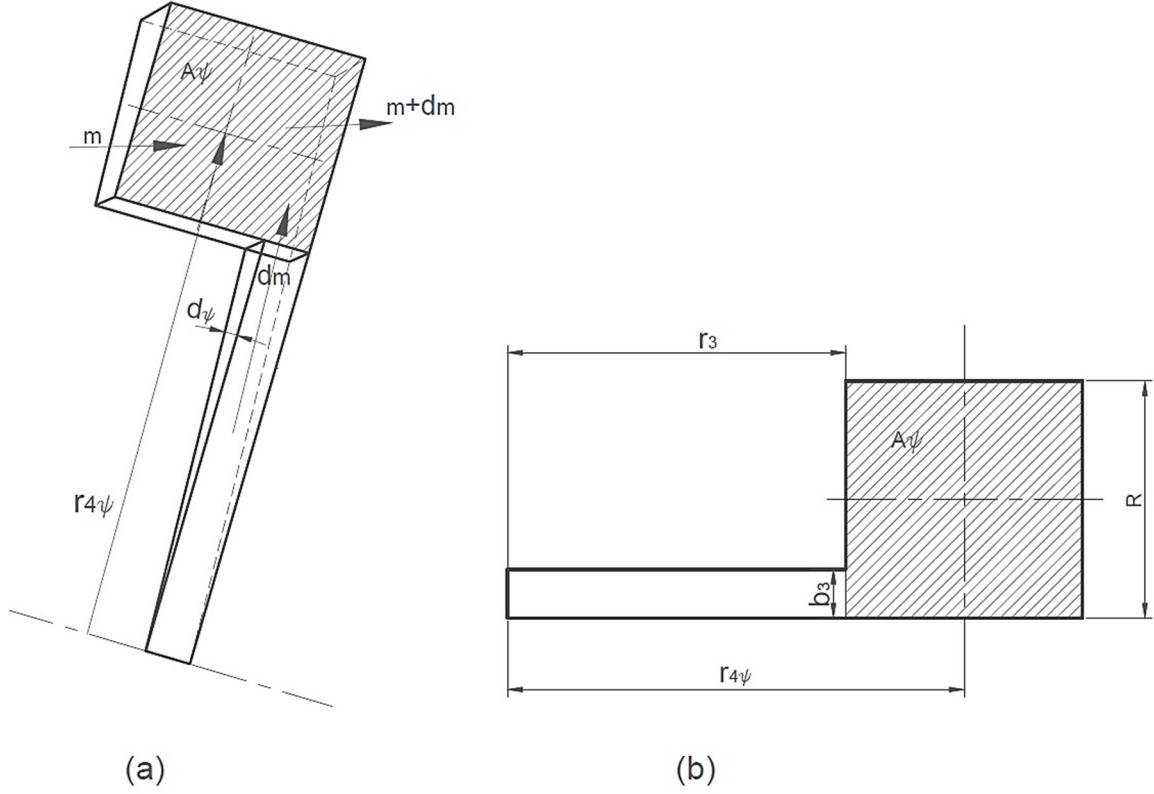
Figure 3.8: Volute element schematic

To solve this equation at any cross section of the volute located at angle Ψ , the area of that section and the tangential flow velocity at the section centroid are required. Benisi *et al*. [62] assumed that the angular momentum of the fluid is conserved between the volute inlet and discharge, therefore the flow velocity can be calculated using equation 3.7.

$$C_{\theta 4\Psi} r_{4\Psi} = C_{\theta 3} r_3 \qquad (3.7)$$

By combining equations 3.6 and 3.7 the ratio of the section's area to its centroid radius can be written as:

$$\frac{A_{4\Psi}}{r_{4\Psi}} = \frac{C_{r3}}{C_{\theta 3}} b_3 \Psi \qquad (3.8)$$

Because of manufacturing limitations, the volute was designed with a square cross section with side length R. Referring to figure 3.8b, the cross-sectional area and centroid radius

59

can be written in terms of the square side length and the diffuser exit radius, and hence equation 3.8 can be solved for the side length of the volute cross section. Getting all the dimensions for the compressor parts, next comes the geometry generation so CFD can be performed to analyse the compressor performance.

3.3.4 Specific Heat Change

The variation in the specific heat c_p and the specific heat ratio γ has an important effect on the turbomachinery design as the performance estimation of the components is affected by their values. Hence, the variation of the specific heat should be considered in the design and the performance estimation processes. Generally, in gas turbines operating using fuels their values are a function of the temperature and the air to fuel ratio, however the solar powered MGT operates using air only therefore their value is a function of temperature only.

To gain an accurate value for c_p and γ, an iterative approximation method was used in the design of both the turbine and compressor. In this method, an initial guess for c_p and γ values were used to calculate the initial temperature raise (through the compressor) and drop (through the turbine). Thereafter, the mean values for c_p and γ between the inlet and exit conditions were used to regenerate the next values of the temperature at the exit of the compressor and turbine. Number of iterations were performed to reach accurate values for c_p and γ. To gain more accurate results the entropy curves can be used to evaluate these values of c_p and γ [63].

3.4 Impeller Geometry Generation

Like the turbine rotor, the compressor impeller blades are defined by the meridional projection of the hub and shroud contours, blade thickness along hub and shroud, and the

camberline of the blade defined at the mid span. The hub and shroud projection curves are defined by third order Bezier curves with four control points. The starting and the end points are defined by the radii and blade heights at rotor inlet and exit and the remaining points' position can be changed to achieve the best performance. Referring to figure 4.14, blade camberline can be defined by the distribution of the angle β along the z-axis where β is the blade angle referred to the axial direction. Verstraete et al. [64] defined β for both full and splitter blades using a third order polynomial (equation 3.9).

$$\beta(s) = \beta_o(1 - s)^3 + 3\beta_1 s(1 - s)^2 + 3\beta_2 s^2(1 - s) + \beta_3 s^3 \qquad (3.9)$$

Where s is the non-dimensional meridional length of the camberline ($0 \leq s \leq 1$). β_o and β_3 are the blade angles at the leading edge and the trailing edge respectively. By knowing the angle β, it is possible to calculate the blade angle distribution referred to meridional plane (θ) for radially fibered blades using equation 3.10.

$$\frac{d(r\theta)}{dz} = \tan \beta \qquad (3.10)$$

The thickness of the blades was defined at the hub and the tip and was assumed to be linearly distributed along the camberline. At the shroud, blade thickness was given a constant value along the stream wise direction. At the hub, the thickness distributed in parabolic form, where the thickness of the blade at the leading edge allocated the same value as the shroud. The maximum thickness occurs at 65% of blade length [64]. The final values of blade thickness can be finalised using finite element analysis for the impeller.

3.5 Compressor Design for 6 kWe gas turbine

The compressor design method described earlier has been applied to the design of a centrifugal compressor to meet the cycle specifications of 6 kWe gas turbine. The design

parameters used are discussed in this section together with the results generated using the meanline design program and the CFD results.

3.5.1 Design Parameters

The operating conditions at the design point of the compressor with the performance parameters needed for the impeller design are listed in table 3.1. The compressor should run at the turbine rotational speed as they are mounted on the same shaft and is required to deliver 0.09 Kg/s of air to satisfy turbine requirements. The compressor inlet is drawing air directly from the ambient, therefore standard atmosphere temperature and pressure values were used for the total thermodynamic properties of the air.

Table 3-1: Compressor design parameters

Parameter	Value
Mass flow rate	0.09 kg/s
Total inlet pressure	1 atm
Total inlet pressure	288 K
Rotational speed	130,000 rpm
Blockage percent	3%
Back sweep angle	30 °
Number of impeller blades	16
Absolute flow angle	0 °
Inlet hub radius	9 mm
Turbine Tip diameter	36.7 mm
Diffuser leading edge radius ratio	1.12
Diffuser throat aspect ratio	1
Diffuser channel length to width ratio	10
Target recovery coefficient	0.7

Whitefield *et al*. [6] found that using a value of 3% to compensate for the boundary layer blockage at the impeller inducer is fairly accurate for subsonic impellers. Therefore, the

impeller design starts with 3% blockage, however the inducer geometry can be modified to achieve the desired mass flow rate depending on CFD results. As mentioned in section 3.3.1, the Optimum number of impeller blades ranges between 12 and 16. To select the right number of blades, three impellers with 12, 14 and 16 blades were analysed using CFD. The most stable performance was achieved using 16 blades, where lower number of blades was noticed to induce higher secondary flows along the impeller passage. Figure 3.9, shows the rotating shaft of the MGT, where the tie rod of the shaft diameter is 7.6 mm, therefore the diameter of the hub diameter was limited to 18mm to leave some material to grind in the shaft balancing process.

As describe earlier, the vaned diffuser design starts by locating vanes leading edge radius ratio (r_1/r_2); where a value of 1.12 was used following Rodgers suggestions [60]. By knowing the diffuser leading edge radius, Mach number can be calculated by assuming the angular momentum is conserved in the vaneless space. Using Mach number value and assuming aspect ratio 1, a channel diffuser map for similar values can be used to design the initial geometry of the diffuser channel.

Figure 3.9: MGT shaft arrangement

From the preliminary calculations; the Mach number value at diffuser's leading edge was found to be close to 0.8, therefore the map in figure 3.7 was used to construct the initial

geometry for the diffuser channel. The vaned diffuser was selected not only to achieve high recovery coefficient, but also for the compactness of the design; therefore, length to width ratio10 and recovery coefficient 0.7 were used. The diffusion angle and the area ratio corresponding to those values are 7º and 2.2 respectively.

3.5.2 Three-Dimensional Geometry

Using the commercial tool ANSYS BladeGen; the compressor impeller blades were generated. BladeGen requires radii at inlet and exit, the hub and shroud meridional curves, blade angle along the camberline and blade thickness. The inducer and exducer radii values were obtained using the one-dimensional calculations. The blade camberline curve and the thickness distribution of the blades are described in section 3.4 while the hub and shroud meridional curves were defined using a third order Bezier curves. Both camberline and meridional curves were modified manually couple of times to achieve the required mass flow rate, pressure ratio and satisfying the conditions listed in section 3.2. The final impeller geometry that delivers the right amount of flow and pressure rise and maintains aerodynamically satisfactory flow along its passage is shown in figure 3.10. In this design, the same camberline and meridional curves definition and thickness distribution were used for both full and splitter blades.

The diffuser vanes were constructed using the commercial software (SolidWorks). Once the diffuser channels' geometry is known, the throat of the pressure surface corner can be positioned at the diffuser inlet radius r_2 and rotated to achieve the desired tilting angle γ. Referring to figure 3.4b, the initial value of γ can be calculated using equation 3.11 which assumes the suction surface incidence angle to be -4 as discussed in section 3.3.2.

$$\gamma = \alpha_2 - |4 - \emptyset| \qquad (3.11)$$
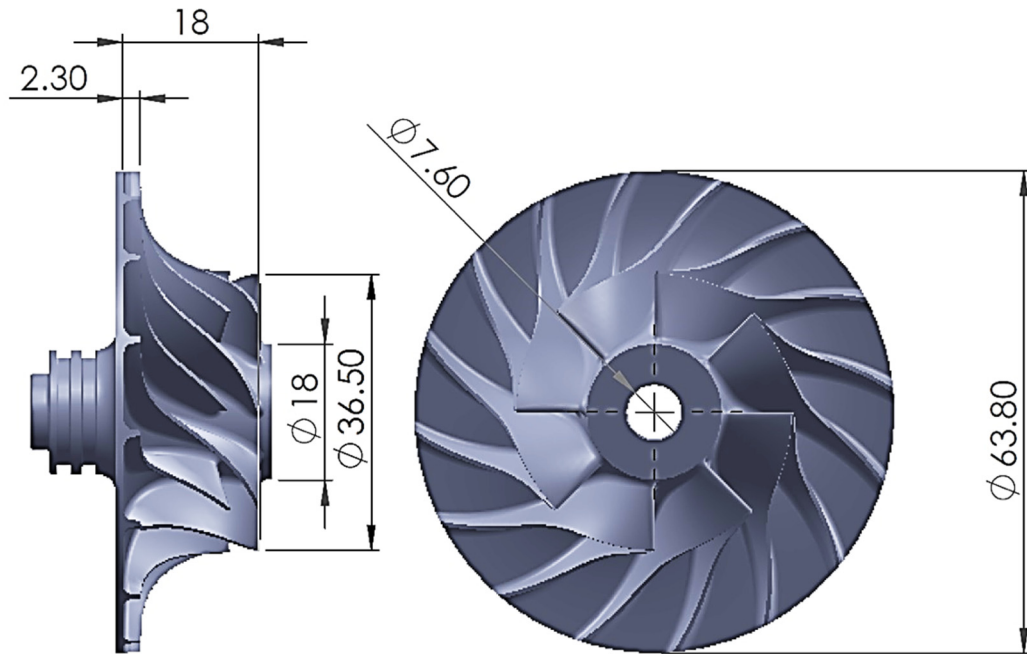
Figure 3.10: Impeller geometry

After that an array with the required number of vanes is constructed around the rotation axis. The vane island is then constructed by connecting the pressure surface of one channel with the suction surface of the neighbouring channel. The curve connecting the suction surface throat corner with the pressure surface throat corner is drawn as a cubic curve. Whitefield *et al*. [6] used this method to generate a concave surface along the vaneless space to match the flow path of the air where the flow doesn't move in straight lines in the vaneless space of the diffuser. At the trailing edge of the vane the suction and pressure surfaces are connected using a circular curve of radius equal to the suction surface trailing edge radius. The design process of the diffuser is iterative, therefore the tilting angle, area and aspect ratios and channel length were modified iteratively based on the CFD results to achieve the required diffusion at the design point. The final diffuser geometry is shown in figure 3.11.
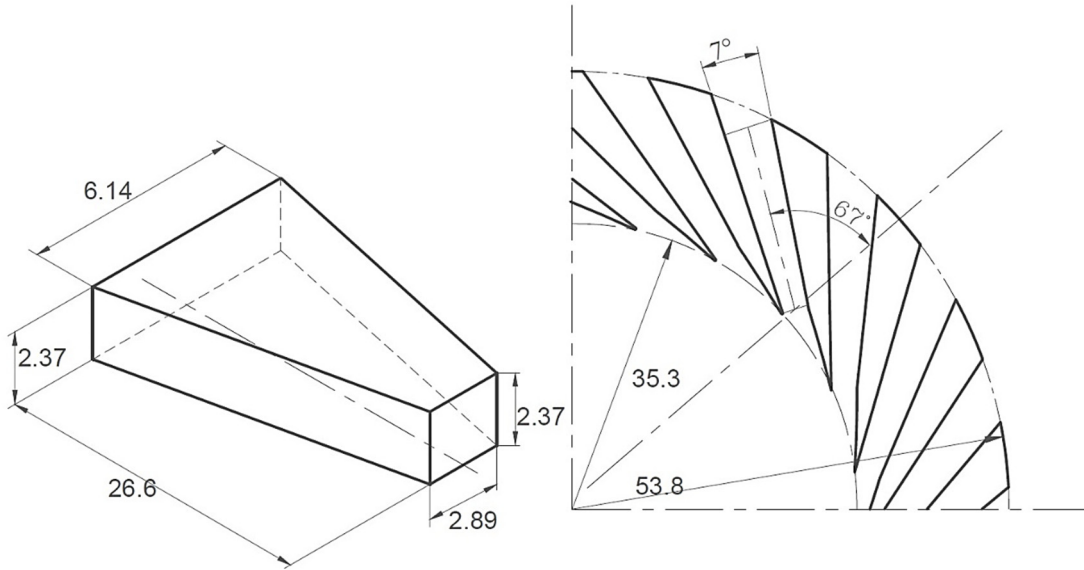
Figure 3.11: Channel diffuser geometry

Finally, the volute geometry was generated in SolidWorks using the geometrical data in table 3.2.

Table 3-2: Volute geometry data

Volute Angle (°)	0	30	60	90	120	150	180	210	240	270	300	330	360
Cross section side length (mm)	48.3	45.7	43.1	40.3	37.5	34.6	31.6	28.3	24.9	21.1	16.8	11.5	0.0

3.5.3 Numerical Methodology

To refine and verify the compressor design, CFD has been performed on the Compressor stage. One full and one splitter blades, single diffuser passage and the volute were set as the computational domain for the CFD analysis. Usually modelling compressor is done without the volute, however it has been included to increase the accuracy of predicting the compressor performance including pressure loss that occurs along the volute passage. ANSYS Turbo Grid was used to generate hexahedral structured meshes for the impeller and diffuser passages, and ANSYS Workbench meshing tool was used to generate tetrahedral unstructured mesh for the volute. The numerical analysis was performed using

ANSYS CFX 15.0 solver. The flow was assumed to be fully turbulent. This assumption is based on the calculated Reynolds number in the rotor passage. The Reynolds number was calculated assuming the flow in the impeller passage as a rectangular duct flow, therefore using the passage hydraulic diameter, Reynolds number at the design point is 5.7×10^5. Non-slip boundary condition was set for the passage surfaces. In order to solve the boundary layer accurately, the near wall mesh was refined to achieve first node non-dimensional distance $y^+ = 1$. Stage connection (mixing planes) were used between impeller and diffuser and between the diffuser and the volute. Uniform total pressure and temperature were set at the domain inlet and uniform static pressure at the domain outlet. As one diffuser passage and one impeller full and splitter blades were used, rotational periodicity was imposed on the periodic boundaries. Similar to the turbine rotor, the tip clearance was set to 7% of the blade span to comply with machining tolerances. With this setup, a steady state solution was generated using CFX.

3.5.4 Grid Independence Analysis

To ensure that the CFD solution is independent of mesh refinement, a grid independence study has been performed. Two parameters: the mass flow rate and the total pressure ratio were calculated. Six grids of increasing refinement have been used to calculate these parameters, starting with a coarse grid of 400,000 nodes and ending with a grid of 2,500,000 nodes. Figure 3.12 shows the percentage difference in calculating mass flow rate and pressure ratio referring to the values generated using the finest grids. Using the gird of about 1,100,000 nodes the difference was reduced to less than 0.15% for both parameters. The final mesh for the impeller and the diffuser are shown without the volute for clarity in figure 3.13.
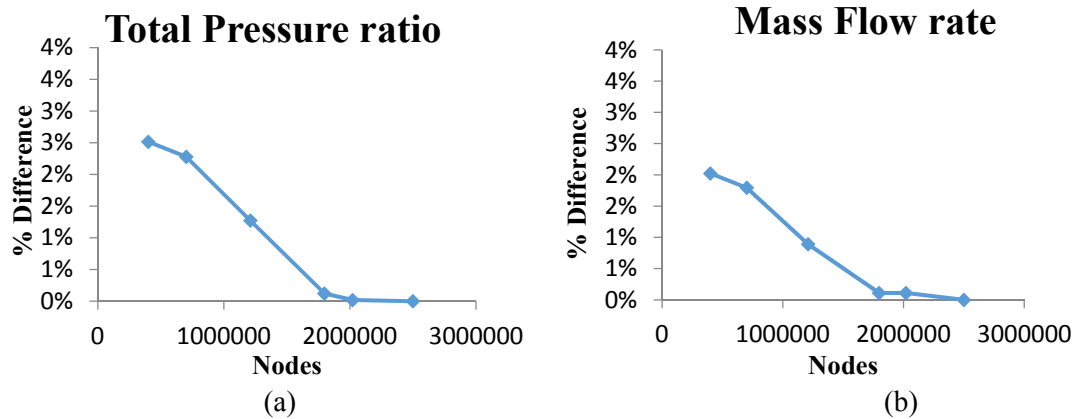
Figure 3.12: Grid independence study for compressor (a) pressure ratio (b) mass flow rate
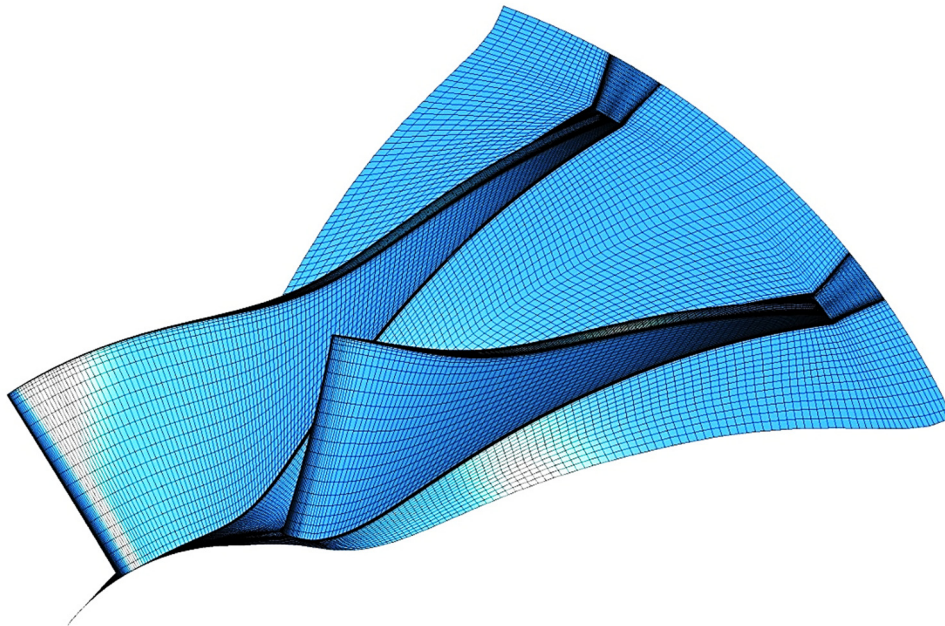
Figure 3.13: Impeller grid

3.5.5 Compressor Design Validation

After finalising the compressor design, the results of the CFD analysis and the preliminary design were compared for the impeller stage in table 3.3. The impeller geometry design is strongly related to the velocity triangles; therefore it is suitable to compare the preliminary design velocity triangles with those generated using CFD. Velocity triangles at impeller inducer and exducer are shown in figures 3.14 and 3.15 respectively. In the meanline design the inducer area was calculated based on boundary layer blockage of 3%, where this

assumption is used for 16 full blades, however in the real design the number of full blades is 8 blades and 8 splitters. The splitter blades were intentionally positioned where the passage area starts to increase abruptly to reduce the boundary layer blockage. This means that the blockage would be less than the assumed value which explains the higher mass flow rate predicted using CFD. Increasing the mass flow rate will lead to increase in the meridional flow velocity and, at constant rotational speed, increasing the meridional velocity will lower the relative flow angle as shown in figure 3.14. The meridional flow velocity of the flow does not change considerably along the compressor impeller passages; therefore, the mass flow difference will have similar effect on the exducer velocity triangle as shown in figure 3.15.

To seal the turbine and the compressor of the MGT, piston ring seals were used. Those seals are not only responsible for preventing air leakage from both turbine and compressor but also they should prevent the oil used for cooling the shaft bearings to enter their housing. For this purpose, compressed air is taken from the compressor outlet where the pressure is higher than the oil pressure and injected between the seals, hence the blockage factor wasn't modified to let more air to enter the impeller to compensate for the sealing air.

Table 3-3: Comparison between preliminary design and CFD results for the compressor impeller

Parameter	Preliminary design	CFD	% Difference
Impeller Inducer			
Total temperature (T_{o0}) [K]	288	288	0
Static temperature (T_0) [K]	283.4	283	0.1
Total pressure (P_{o0}) [bar]	1.013	1.013	0.0
Static pressure (P_0) bar]	0.95761	0.95340	0.4
(r_{0t}) [mm]	18.5		-
(r_{0h}) mm]	9		-

Absolute flow velocity [m/s]	96	110	12.3
Relative flow velocity [m/s]	269.5	254	6.1
Absolute flow angle [Degree]	0	0.48	-
Relative flow angle [Degree]	69	65.67	5.1
Impeller Exducer			
Total temperature (T_{o1}) [K]	415	420	1.2
Static temperature (T_1) [K]	368	363	1.4
Total pressure (P_{o1}) [bar]	3.039	3.1	2.0
Static pressure (P_1) [bar]	1.997	2.116	5.6
(r_1) [mm]	31.9		-
Absolute flow velocity [m/s]	307.5	331	7.1
Relative flow velocity [m/s]	171.6	174	1.4
Absolute flow angle [Degree]	72	69.8	3.2
Relative flow angle [Degree]	49	51	3.9
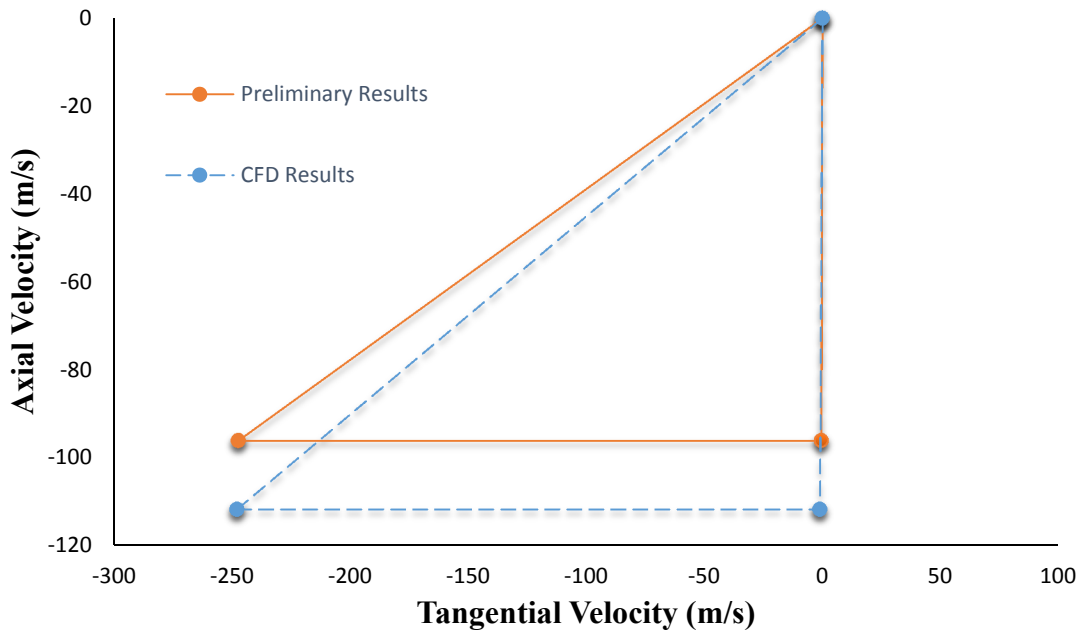
Figure 3.14: Comparison between Preliminary design and CFD velocity triangles at impeller inducer
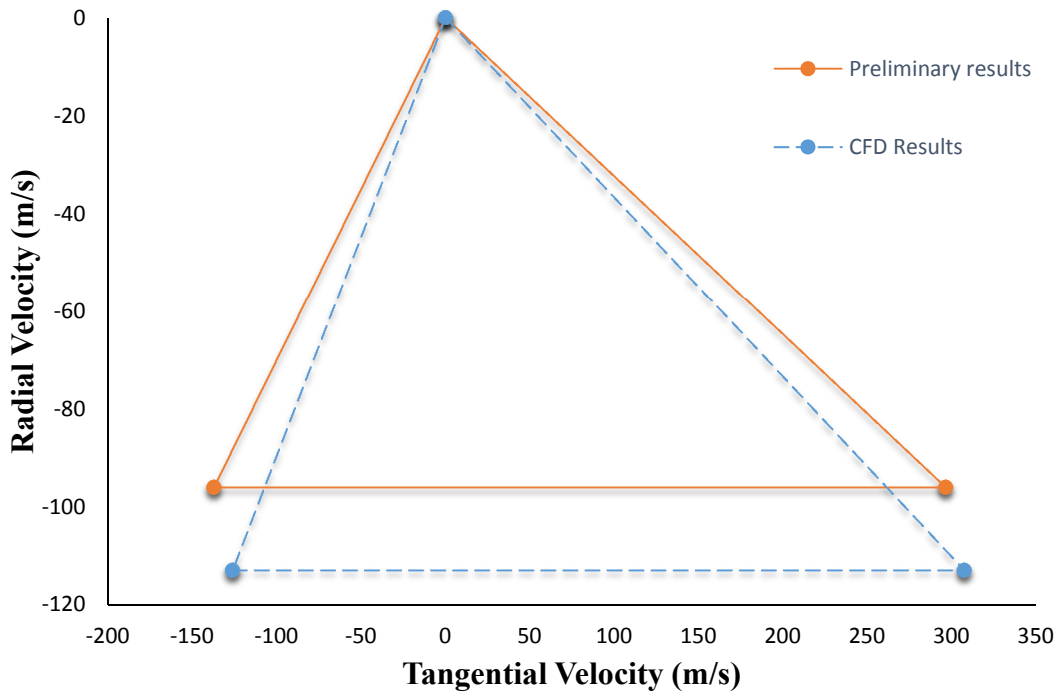
Figure 3.15: Comparison between Preliminary design and CFD velocity triangles at impeller exducer

Figure 3.16 shows the deviation between the blade and flow incidence angle at the impeller inducer at different spanwise location.
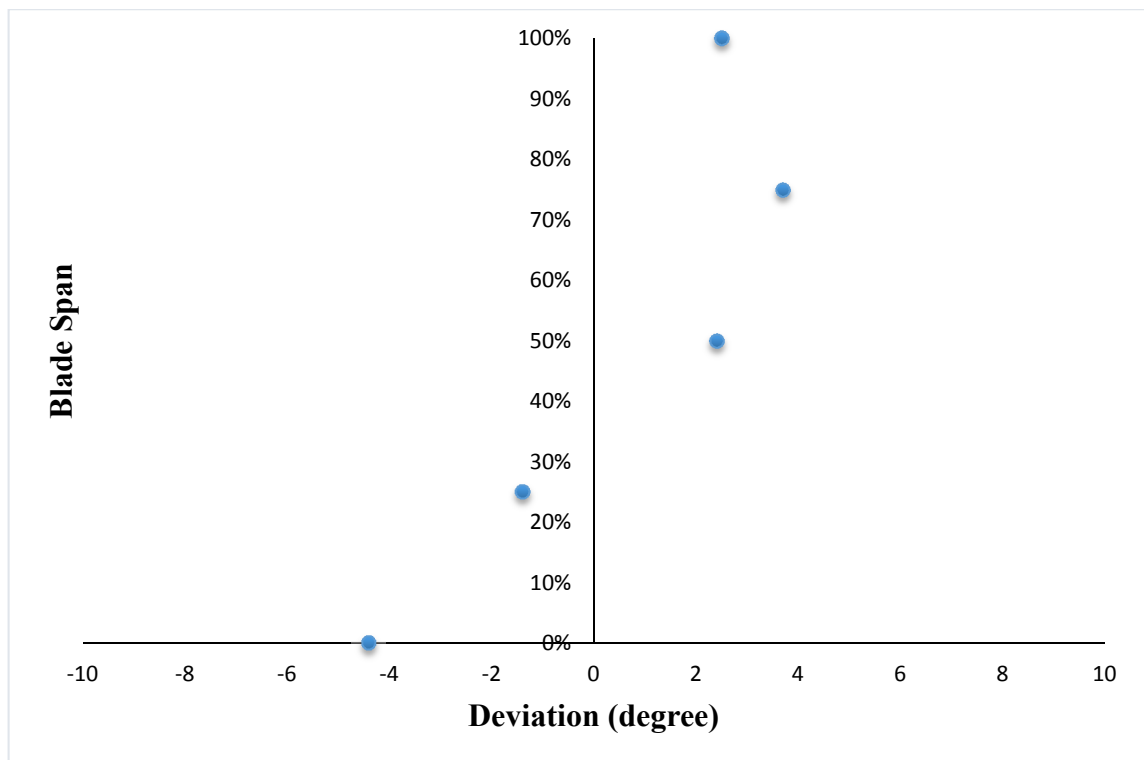
Figure 3.16: Deviation between blade and incidence angle along the span of the impeller inducer

From the hub to 30% of span, the incidence angle is negative as the blade angle is relatively small, where the maximum deviation angle of 4.4º occurs at the hub. As the blade angle starts increasing in the radial direction, the incidence angle becomes positive. The overall deviation between the flow and the blade angles is sufficiently small, indicating that the inducer design is sufficient to avoid any adverse effect which leads to boundary layer stall. In figure 3.17 the velocity vectors are plotted along the impeller and diffuser passages at 50% of blade span. It can be noticed that the flow vectors are aligned in the streamwise direction, also no flow recirculation flows detected.
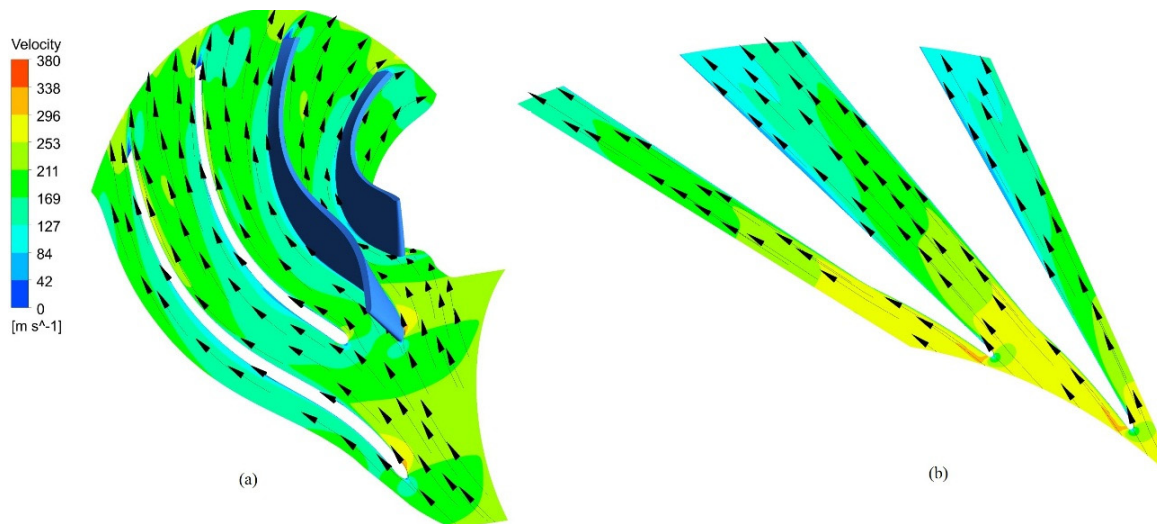
Figure 3.17: Velocity vectors distribution (a) impeller passage (b) diffuser passage

The blade loading at mid span for the full impeller and splitter blades are plotted in figures 3.18 and 3.19 respectively showing that there is not sudden changes in blade loading. At the leading edge of both blades, a small jump in the pressure occurs at the pressure surface, this drop occurs due to flow acceleration trying to pass around the blade leading edge which could lead to stall. In figure 3.20, velocity vectors around impeller blades shows that the flow does not stall due to the pressure jump spotted on the blade loading graphs. At the trailing edge part, air leaks from the pressure side and re-enters the impeller passage from the suction side, this recirculated flow leads to the pressure drop spotted at the pressure surface close to trailing edge.
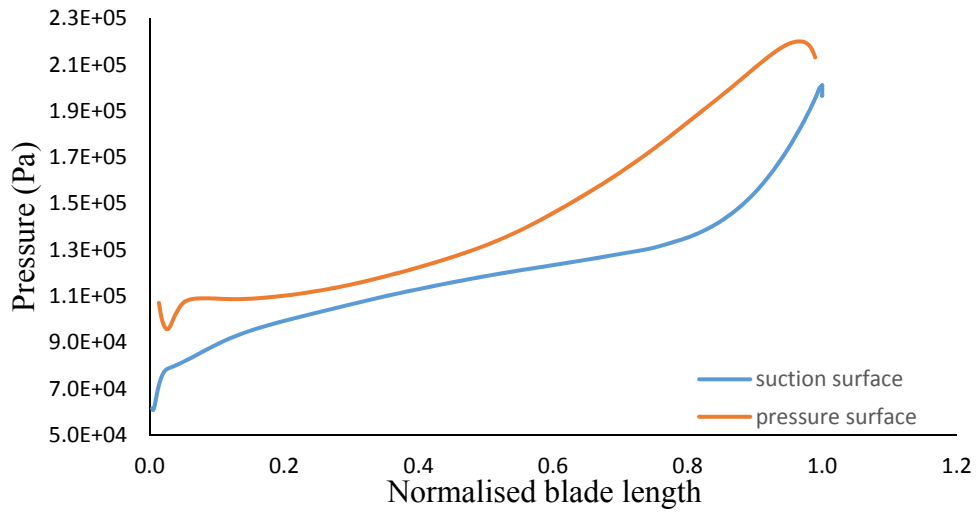
Figure 3.18: Blade loading distribution along the impeller full blade
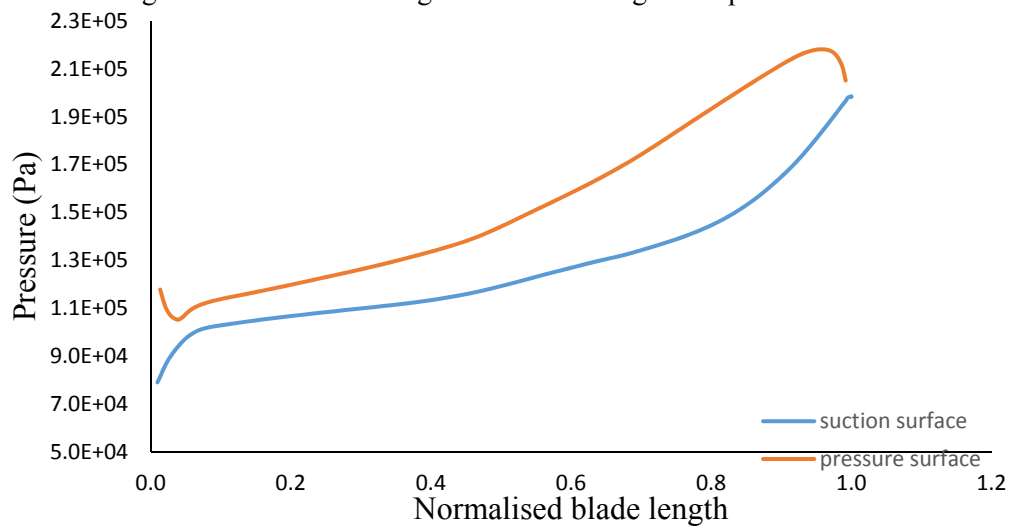
Figure 3.19: Blade loading distribution along the impeller splitter blade

(a)

(b)
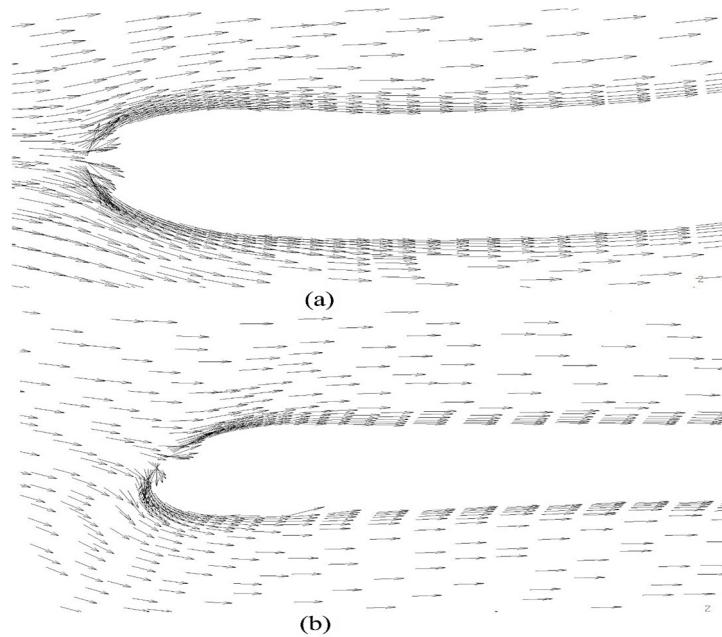
Figure 3.20: Velocity vectors near the leading edge at mid span for (a) full blade (b) splitter blade

3.6 Stress Analysis for the Compressor Impeller

Structural analyses for the compressor impeller has been conducted to ensure that it doesn't fail during operation. This has been conducted assuming an operating speed of 130,000 rpm and running temperatures of 105°C. The temperature used is the relative total temperature at the exit impeller blade resulted from the CFD calculations. The meshing and the stress analysis has been performed within ANSYS static structural software. Figure 3.21 shows the results of the analysis for the compressor.
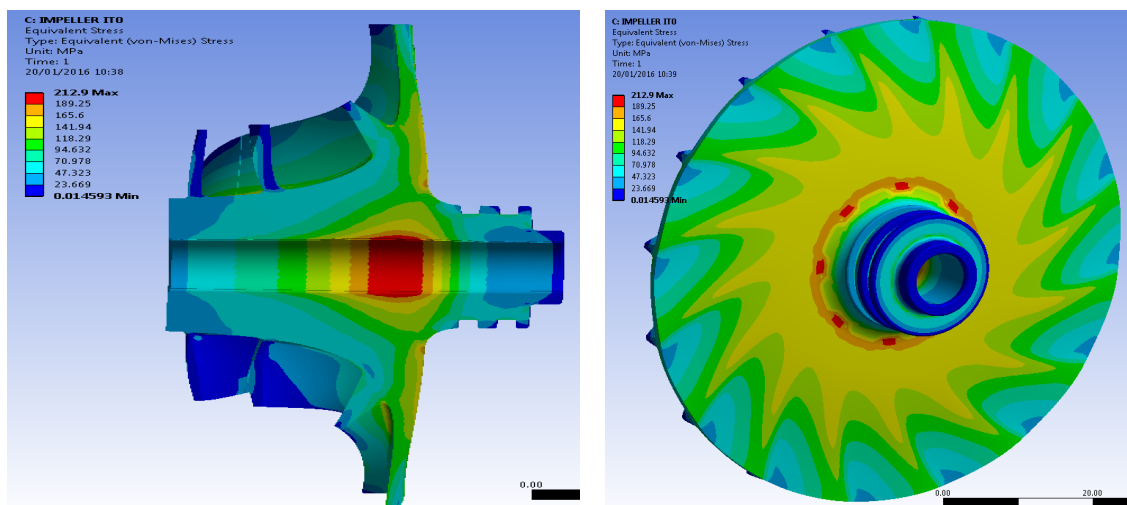
Figure 3.21: Equivalent stress of compressor operating at 130000 rpm and 105 C

As can be seen, the maximum stress occurs at the impeller bore with a value of 213 MPa. This value is below the yield strength of the aluminum alloy selected for the impeller (6082 AL). To complete the structural analysis for the compressor wheel, a low Cycle Fatigue (LCF) and a blade vibration analysis have to be performed to estimate the life of the wheel and the health of the blades under loading.

3.7 Compressor Map Generation

The compressor performance maps are normally generated to monitor its outputs and performance at different rotational speeds and to indicate the operating envelope. There is an abundance of models in the literature for performance prediction of centrifugal

compressors. To provide confidence in a particular model for a given design, experimental data is needed, which would not be available at the design stage. Typical loss models used for performance prediction are one-dimensional empirical correlations. The accuracy of these correlations depends on the quality and generality of the test data that they are based on. Loss correlations typically break down the losses into categories, each one can be modeled and calculated separately. However, this may compromise the accuracy of predictions as some loss mechanisms are strongly related to each other.

Compressor efficiency simply indicates loss occurs in the machine, and it can be predicted by measuring the pressure and temperature at compressor inlet and exit. CFD can also be used to estimate the compressor efficiency. Similar to the turbine rotor, including the impeller back space and modelling the surface roughness increase the complexity of the CFD case. Therefore, in this work, the performance map is initially generated using CFD results, then it is updated to account for windage and friction losses which are calculated using analytical correlations.

To evaluate the windage loss caused by the viscous forces of the fluid between impeller back face and the casing, Daily and Nece [25] formula (equation 2.34) can be used. And for the friction loss within the rotor passage, Jansen [17] treated the flow in the impeller passage which consists of the blades' surfaces, the hub, and the shroud as a duct flow. Based on his model, the friction loss can be calculated using equation 3.15.

$$\Delta h_{fr} = C_{sf} \left(\frac{L_H}{D_H}\right) \frac{(\bar{W}^2)}{2} \qquad (3.15)$$

Where, L_H and D_H are the hydraulic length and hydraulic diameter of the impeller passage which can be calculated using equations 3.35 and 3.36 respectively. The skin friction factor (C_{sf}) has a value of 0.11 for low specific speed compressors, and 0.22 for

high specific speed compressors. $\overline{W}$ is the average flow velocity given by Both *et al.* [65] as:

$$\overline{W} = \frac{V_{0t} + V_1 + W_{0t} + 2W_{0h} + 3W_1}{8} \tag{3.16}$$

After finding the loss due to friction and windage, the compressor total to total isentropic efficiency can be reformulated to account for those losses as follows:

$$\eta_{tt} = \frac{\Delta h_{CFD}}{\Delta h_{CFD} + \Delta h_w + \Delta h_{fr}} \times \eta_{tt(CFD)} \tag{3.17}$$

Figure 3.22 shows the compressor performance map generated for the designed compressor using the presented method and using the CFD results only.
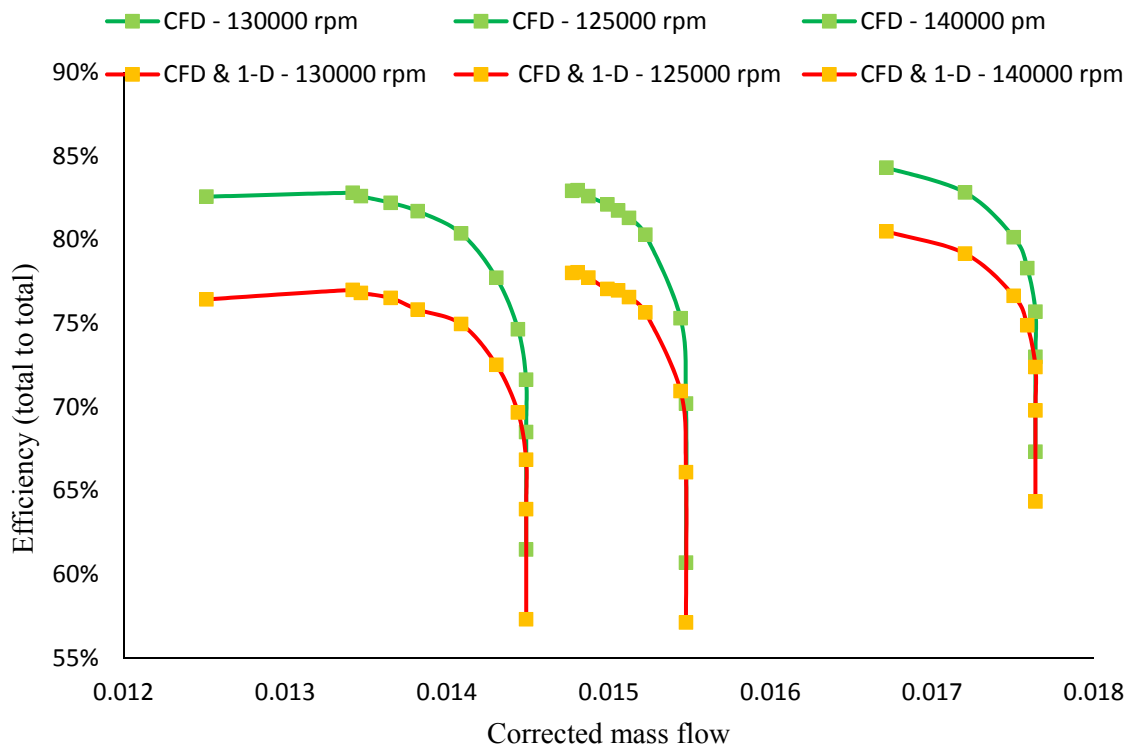
Figure 3.22: Compressor map generated accounting for windage and friction losses

The difference between both methods ranges between 3.5-8 % in compressor efficiency, which indicates a high importance to account for the friction and windage loss to gain an accurate performance map for the compressor. This model has not been validated against the actual performance of the compressor. The time limitation did not allow for characterising the compressor performance before the submission of this thesis. However,

validation of the methodology experimentally for the turbine case give some re-assurance to the suitability of this model. Moreover, in the near future a test would be setup to generate a full performance map for this compressor.

Conclusions

Within this chapter a methodology for centrifugal compressor design has been presented and was successfully employed to generate a compressor geometry for a 6 kWe micro gas turbine. The limitations of the CFD to predict accurately the compressor performance have been addressed. Compressor designers normally avoid adding the back face clearance to the computational domain and treat the impeller walls as smooth surfaces to remove geometrical and numerical complexity of the numerical domain. In this chapter, a new method to modify the CFD predictions of the compressor performance was proposed. In this method, the losses due to the back face clearance and the surface roughness of the impeller were calculated using the loss correlations available in the open literature. This method has been successfully applied to the radial turbine which gives confidence in its accuracy, however in the future the generated map must be verified against the experimental data for the designed compressor.

Chapter 4

4. Radial turbine design

4.1 Introduction

This chapter presents a methodology for radial turbine design, which was used to design a turbine for a 6 kWe solar powered MGT. A meanline methodology was used to calculate the main geometric parameters for the turbine components which subsequently were used to generate a three-dimensional geometry of the components. Computational Fluid Dynamics (CFD) was used to refine the components design to achieve better performance.

Turbine design procedures are well documented in the standard text books. Thus, the main objective of this chapter is to improve the accuracy of predicting the turbine performance by using the one-dimensional loss correlations to improve the CFD predictions. The proposed method is explained within this chapter and validated against the experimental data of two turbines.

4.2 Turbine Design

Referring to figure 4.1, the design process followed in this work starts with the meanline design for the turbine components. The outputs of these calculation are then used to generate the three-dimensional geometry for the turbine parts. A performance analysis and flow behaviour examination using CFD tools is then used to refine the design to reach the desired performance. This section briefly describes the design steps and provides details for the meanline design process.
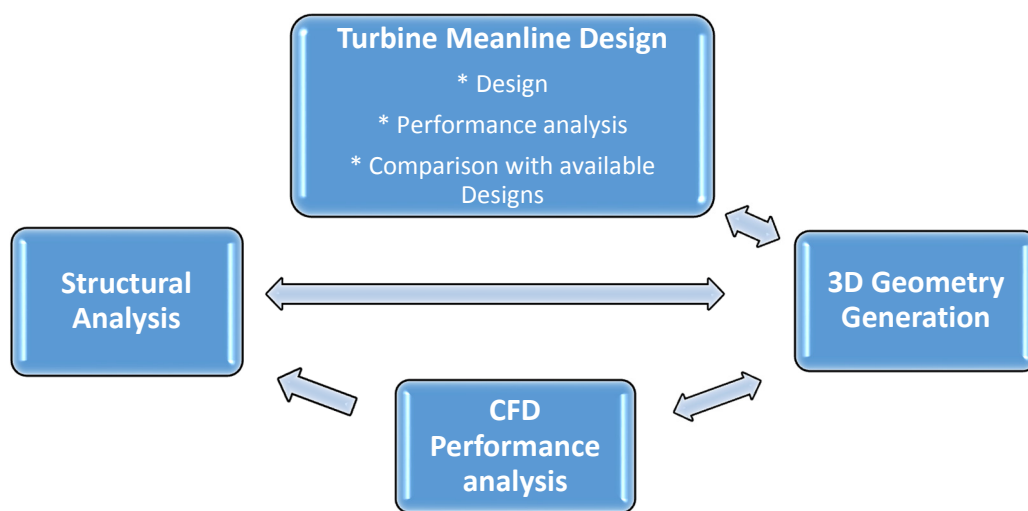
Figure 4.1: Turbine design process diagram

The process starts by implementing thermodynamic properties of the working fluid entering the turbine and its expected performance in the preliminary design program. Based on these parameters and the performance parameters recommended in literature; the appropriate thermodynamic and fluid dynamic conservation principles are applied within design process to obtain the following results:

- The main geometric parameters of components such as the mean radii, blade height and blade angles at inlet and outlet of the rotor wheel.

- Thermodynamic quantities at the inlet and outlet of each component.

- The flow velocities at the defined stations.

Using those outputs, the geometry of the turbine can be build. CFD then can be used to study the flow behaviour at the design point operating conditions to indicate the required modifications on the turbine geometry to get an aerodynamically satisfactory design. In the next section the meanline design method is explained.

4.3 Meanline Design:

A meanline or one-dimensional design approach is the application of basic equations and empirical relations to calculate the overall design parameters. This method is a good approach to get the first estimate for the radial turbomachine design and analysis as it is fast and needs a small amount of information regarding the turbomachine geometry. Also, several design options can be checked before moving to advanced stages of system design including three-dimensional geometry construction and computational analysis.

To perform the meanline design a MatLab based program has been built. Two sets of data should be fed to the program. The first set includes the required outputs from the turbine, and the operating conditions. Those values usually come from the gas turbine cycle analysis and required power output.

- Turbine inlet total temperature.

- Turbine inlet total pressure.

- Mass flow rate.

- Required output shaft power.

- Shaft speed.

The second set comprises empirical parameters that are a combination of performance and dimensionless ratios available in literature. Based on the given data; the design

program performs the design calculations for the turbine rotor, nozzle guide vanes and the volute. The diffuser design is done separately after that.

4.3.1 Rotor Design

Figure 4.2 shows a schematic for a radial turbine stage. The design starts by determining the velocity components and angles of the velocity triangles at the rotor inlet and discharge. As previously mentioned, a number of parameters has to be defined based on the recommendations in the literature to start the calculations process. The first parameter used here is the stage loading coefficient, which indicates the work capacity of the turbine and can be expressed as:

$$\psi = \frac{\Delta h_o}{U_3{}^2} \tag{4.1}$$

By replacing the enthalpy change by its equivalent, equation 4.1 can be written as:

$$\psi = \frac{C_{\theta 3}}{U_3} - \frac{r_{4t}}{r_{3t}}\frac{C_{\theta 4}}{U_4} \tag{4.2}$$
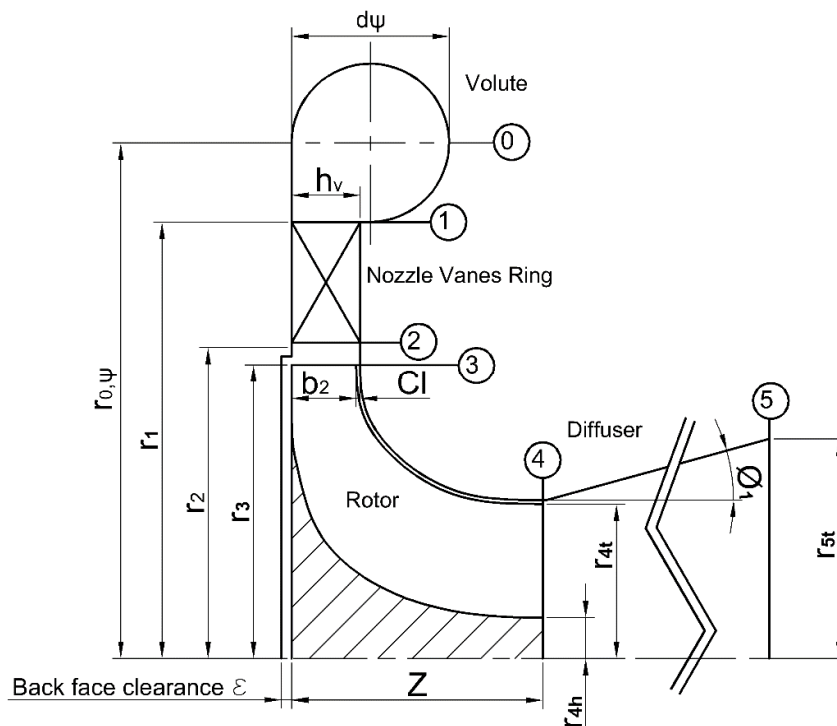
Figure 4.2: Radial turbine schematic

As the swirl at the rotor exit is very small, $C_{\theta4}$ is small compared to $C_{\theta3}$, so equation 4.2 would be:

$$\psi = \frac{C_{\theta3}}{U_3} \qquad (4.3)$$

The blade loading coefficient is another required parameter. It is defined as the rotor exit meridional velocity divided by the rotor inlet blade speed:

$$\phi = \frac{C_{m4}}{U_3} \qquad (4.4)$$

Figure 4.3 shows the total to static efficiency correlation with blade loading and flow coefficient. The points in the figure show the performance points for different turbines, and the efficiency contours has been correlated to these points. From the figure, it can be noticed that inside the best efficiency region (red rectangle); the blade loading ranges from 0.8-1 and the exit flow coefficient from 0.2 to 0.3. Selecting the suitable values for these coefficients is not enough to calculate the velocity triangle components. Therefore, Mustafa *et al*. [32] recommended to use the rotor meridional velocity ratio (equation 4.5) which, normally has a value of unity.
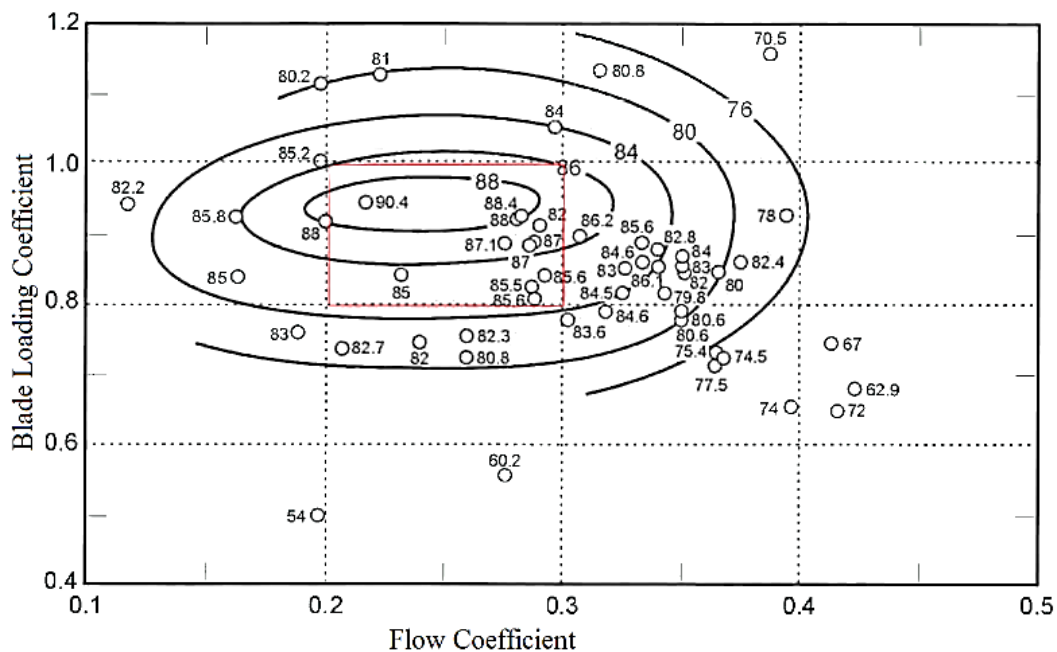
Figure 4.3: Blade loading and flow coefficient correlations for radial turbine [32]

$$\zeta = \frac{C_{m3}}{C_{m4(rms)}} \qquad (4.5)$$

It is also necessary to choose the flow angle at the rotor exit (α_4), which has the value of zero assuming no swirling flow at the rotor exit. Using the previous values and assuming a realistic stage efficiency for the rotor and the stator, thermodynamic states and velocity triangles can be defined at rotor inlet and exit.

After defining the thermodynamic properties and the velocities at the rotor ends, its geometry needs to be defined. To get the main rotor dimensions, a number of geometrical ratios are used. Whitefield and Baines [6] recommended the use of the exit hub to inlet tip radius ratio(r_{4h}/r_3), and the ratio of axial length to rotor inlet radius(Z/r_{t3}) for this purpose. Mustafa et al. [32] suggested a value of 0.3 for the radius ratio (r_{4h}/r_3) to achieve the best performance. Bearing in mind that the small value for rotor exit hub leads to blade congestion at the hub which limits the flow area, therefore, Whitefield and Baines [6] set the following limit for the rotor hub radius:

$$r_{4h} > \frac{Z_B t_h}{2\pi \cos \beta_{4h}} \qquad (4.6)$$

Setting a low axial length to diameter ratio (Z/r_{t3}) would minimise friction losses by shortening the passage length, however the blade wrap angle increases which leads to higher secondary flows and increasing the possibility of flow separation at exducer region resulted from high deceleration rates [66]. A short turbine also improves the rotodynamic stability of the MGT by reducing the overhung mass of the rotating shaft. On the other hand, by using high axial length ratio, the flow passage length increases which will introduce more friction losses but will also reduce secondary flows resulted from decreasing wrap angle and will also retard flow separation at rotor exducer. Hamdan et al. [66] suggested a procedure to calculate the optimum axial length to achieve relative velocity acceleration ratio $\left(w_3/w_{4(rms)}\right)$. Regarding to Rohlik [35], the optimum

performance can be achieved using $(w_3/w_{4rms}) \geq 2$, and based on this, the optimum

axial length ratio would be 0.56.

Starting with the rotor inlet; the continuity equation is used to calculate the area needed to

pass the design mass flow (equation 4.7). The inlet area also can be calculated as the area

of a cylinder with radius equal to rotor inlet and height equal the blade height minus the

area blocked by rotor blades (equation 4.8). Blockage due to secondary flows and

boundary layer development is not accounted for in both inlet and outlet calculations, this

method was used by Mustafa *et al*. [32] and Atkinson [67]. By solving equations 4.7 and

4.8 inlet blade height can be calculated.

$$A_3 = \frac{\dot{m}RT_3}{P_3 C_{m3}} \tag{4.7}$$

$$A_3 = b_3 2\pi r_3 - b_3 N_b t_3 \tag{4.8}$$

Where the rotor inlet blade thickness t_3, was assumed to be constant in the span-wise

direction. In the above equations the symbols $\dot{m}$, b_3 and N_b stand for the mass flow rate,

blade thickness and number of blades respectively.

At the rotor exducer, the calculations are different from the inlet, as the blade thickness

and flow meridional velocity are not uniform in the span-wise direction. Atkinson [67]

used fluid velocity at the rms radius to calculate the flow area.

$$A_3 = \frac{\dot{m}RT_4}{P_4 C_{m4(rms)}} \tag{4.9}$$

Where the rms radius is defined numerically as:

$$r_{4rms} = \sqrt{\frac{r_{4t}^2 + r_{4h}^2}{2}} \tag{4.10}$$

The available geometrical area for fluid flow, can be estimated as the doughnut area of

hub inner radius and tip outer radius minus the area blocked by blade thickness. Blade

thickness was assumed to be linearly distributed from hub to shroud (figure 4.4), so the blockage area due blades can be calculated as:

$$A_{4blade} = \frac{1}{2}(t_{4h} + t_{4t})(r_{4t} - r_h) \tag{4.11}$$
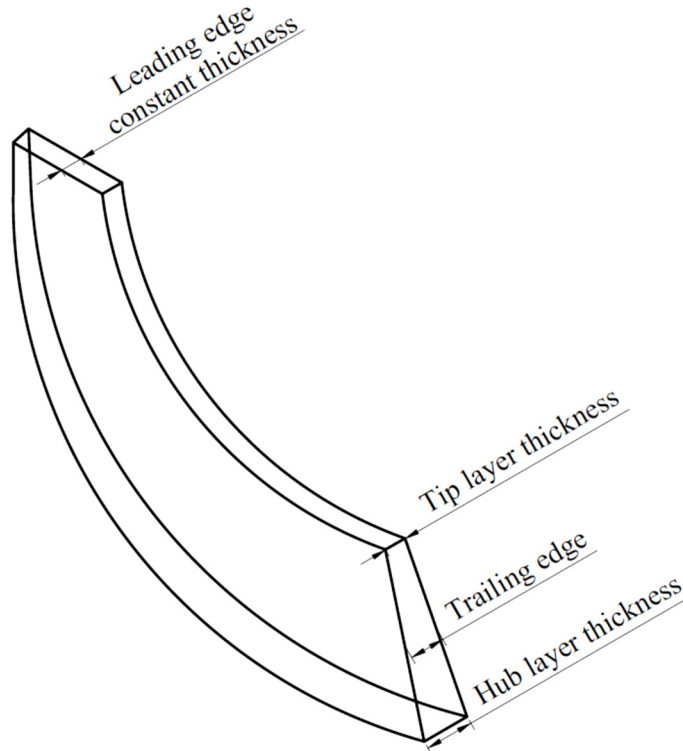
Figure 4.4: Rotor span wise thickness distribution

The flow chart in figure B.1 (see appendix B) summarises the design procedure and the calculations at the rotor inducer, while the exducer calculations are presented in figure B.2. Referring to figure B.1, it can be perceived that design process is an iterative process, where objective at this stage is to reduce the incidence loss to the minimum. Incidence loss is a function of the relative fluid velocity (W_3). Regarding to Glassman *et al.* [36]; the incidence loss can be defined as an enthalpy change using the following relation:

$$\Delta h_{inc} = \frac{1}{2}W_3{}^2 \sin^2 \beta_3 \tag{4.12}$$

To improve the efficiency of the rotor the relative flow velocity at rotor inlet should be reduced as much as possible to reduce the incidence losses.

Using the relation between the loading coefficient and the relative velocity, Mustafa *et al.* [32] suggested to use it to minimise the fluid velocity at the rotor inlet. Referring to figure 2.3a, the velocity triangle components at the rotor inlet are related by the following equation:

$$C_3{}^2 + U_3{}^2 - 2C_3 U_3 \sin \alpha_3 - W_3{}^2 = 0 \qquad (4.13)$$

Using the definition of the loading coefficient $\left(\psi = \frac{C_3 \sin \alpha_3}{U_3}\right)$, the previous equation can be rewritten in 4.14.

$$\psi = \sin^2 \alpha_3 \pm \sin \alpha_3 \sqrt{\left(\frac{W_3}{U_3}\right)^2 - \cos^2 \alpha_3} \qquad (4.14)$$

And for ψ to be real, this condition has to be satisfied $\left(\frac{W_3}{U_3}\right)^2 \geq \cos^2 \alpha_3$. Therefore, the minimum relative velocity can be achieved when $\frac{W_3}{U_3} = \cos \alpha_3$

The second component of the turbine, is the NGV. The next section will explain their design process, which is built to match the rotor design.

4.3.2 NGV Design

The NGVs are distributed around the turbine rotor in the form of ring, and their role is to accelerate the flow approaching the rotor and direct it to the correct angle, to achieve the maximum performance. Initially straight (non-cambered) vanes have been selected for this purpose. This type is easy to manufacture and it is sufficient for the turbine application as the aerodynamic losses within the stator are much less than the losses occurring within the turbine rotor [67].

The design of the NGV has to match the rotor design, therefore, their design starts by finding the optimum distance between the nozzle guide vanes and rotor inlet. Watanabe *et al.* [68] defined this distance using the interspace geometry parameter I_g (equation 4.15).

The interspace gap is essential to allow mixing the flow leaving the NGV trailing edge, however increasing this gap will introduce total pressure loss. Therefore, the optimum interspace value which compromises loses and flow mixing was found to be 2.

$$I_g = \frac{r_2 - r_3}{h_v \cos\left(\frac{\alpha_2 + \alpha_3}{2}\right)} \tag{4.15}$$

To calculate the vane exit radius using equation 4.15, the value of vane exit flow angle α_2 is required. In the interspace region between the rotor and the guide vanes, there is no work done on the fluid, therefore, the fluid total temperature is assumed to be constant along the interspace gap ($T_{o2} = T_{o3}$). Similarly, the pressure loss due to the interaction between the fluid and the passage walls is assumed to be negligible ($P_{o2} = P_{o3}$). Because of the small size of the interspace gap the angular momentum can be considered as a conserved quantity and the flow is a free vortex in the gap, this assumption has been applied successfully by Whitefield and Baines [13] and Mustafa $et\ al.$ [32]. Initially α_2 is assumed to be equal to α_3 (rotor inflow angle). By applying the conservation of angular momentum between vane exit and rotor inlet, the vane exit tangential and absolute velocities can be determined (equation 4.16).

$$C_{\theta 2} = C_2 \sin(\alpha_2) = \frac{C_3 \sin(\alpha_3)\, r_3}{r_2} \tag{4.16}$$

The next value of vanes exit angle can be determined by applying the conservation of mass between vanes exit and rotor inlet (equation 4.17).

$$\rho_2 C_2 \cos(\alpha_2)\, A_2 = \rho_3 C_3 \cos(\alpha_3)\, A_3 \tag{4.17}$$

The density of the air at the vanes exit can be calculated using equation 4.18.

$$\rho_2 = \frac{P_2}{R T_2} \tag{4.18}$$

Based on the earlier assumptions ($T_{o2} = T_{o3}$) and ($P_{o2} = P_{o3}$), the static temperature and pressure can be determined.

$$T_2 = T_{o2} - \frac{C_2^2}{2C_p} \qquad (4.19)$$

$$p_2 = P_{o2}\left(\frac{T_2}{T_{o2}}\right)^{\frac{\gamma}{\gamma-1}} \qquad (4.20)$$

After finding the second value of α_2, the calculation process keeps iterating till the change in its value is negligible. This process is described in figure 4.5.
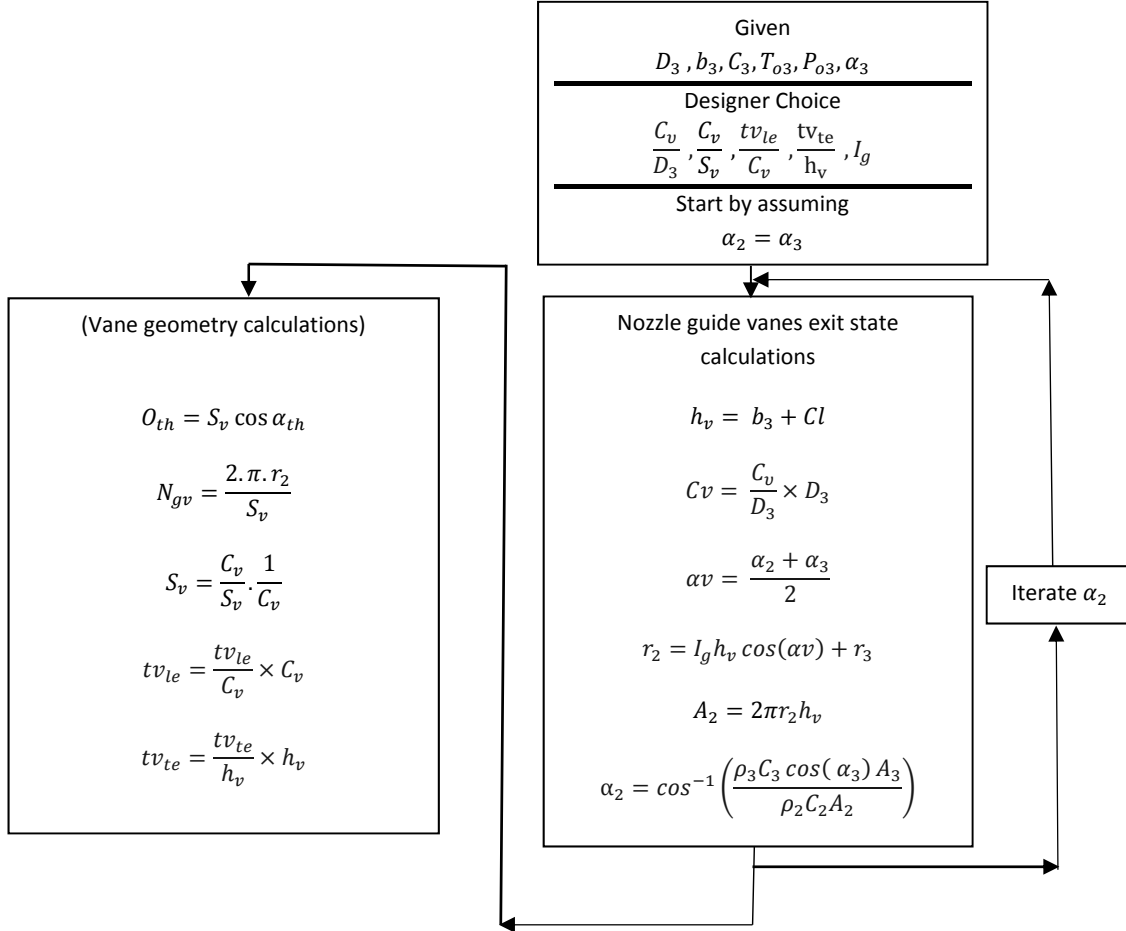
Figure 4.5: Nozzle guide vanes design flow chart

The vane geometry (figure 4.6) can be described by four dimensionless ratios that are: vane chord to rotor inlet diameter (C_v/D_3), vane chord to vane pitch (C_v/S_v), leading edge thickness to vane chord (tv_{le}/C_v) and trailing edge thickness to vane height (tv_{te}/h_v). By selecting the proper values from literature, the vane chord length C_v, vanes pitch S_v and vane leading and trailing edge thickness can be set. By knowing the vanes

pitch, number of vanes can be calculated using equation 4.21 rounded to the closest prime number greater than the resulted value to avoid rotor blades dynamic excitation.

$$N_{gv} = \frac{2\pi r_3}{S_v} \qquad (4.21)$$
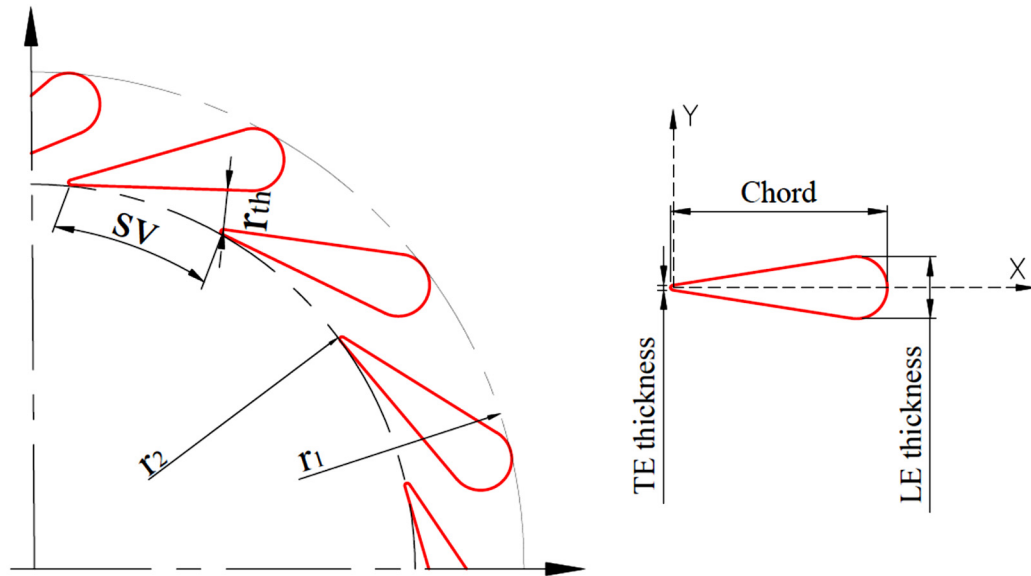
Figure 4.6: Straight Nozzle guide vanes

The last part of the design procedure is to align the vanes in the right setting angle to achieve the desired flow angle and the correct mass flow rate. Different authors such as Hiett and Johnson [48] and Aungier [34] suggested a modification on the cosine rule used to determine the axial turbines stator throat area. Using those methods doesn't guarantee achieving the required throat and flow angle, so they require iteration in the numerical analysis stage. In the straight NGVs, the throat is close to the trailing edge, so the flow deviation between the throat and the trailing edge is negligible. So, the throat of the vanes is calculated using the cosine rule (equation 4.22).

$$O_{th} = S_v \cos \alpha_{th} \qquad (4.22)$$

Where α_{th} is the flow angle at the throat section, in the 1-D calculations it is assumed to be equal to the vane exit angle α_2. The vanes tilting angle was set to α_2 when distributing

the vanes around the stator to achieve the required throat opening and flow angle. Later in the numerical analysis the tilting angle is iterated to achieve the required throat area and required flow angle.

CFD results revealed that straight vanes have a high-pressure loss coefficient, so the decision was to use an aerofoil shaped vanes. The same design procedure has been used to find the angles and throat area. The geometry of an aerofoil shaped vane is described in figure 4.7. The vane camberline was defined by Bezier curve with four control points, the leading and trailing points are defined by the radii at vane inlet and exit. Two control points along the camberline was used to optimise vanes geometry to reach the highest performance. For the blade thickness NACA airfoil thickness distribution was used with maximum thickness to chord ratio of 0.15 located at 0.18 of the chord length from the vane leading edge.
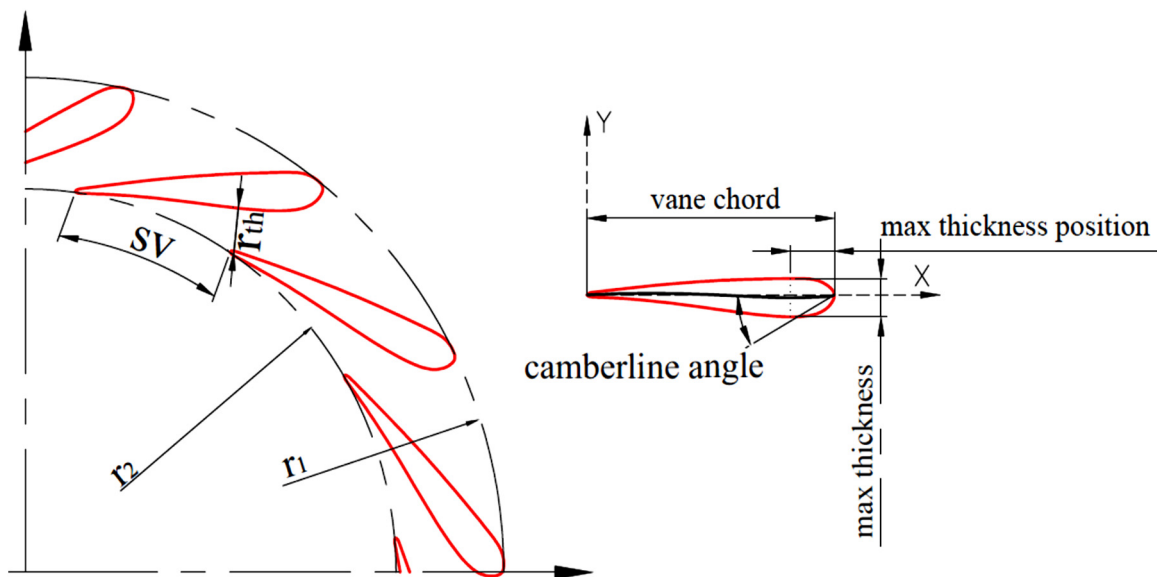
Figure 4.7: Aerofoil shaped NGV geometry schematic

The next section describes the volute design process, which deliver the working fluid from the heating source of the MGT to the NGVs.

4.3.3 Volute Design

Referring to figure 4.8, the volute is an annular volume that delivers uniform flow with a proper incidence angle to the NGVs. The results of the volute design are: the cross-sectional area and the distance between cross sectional area and turbine axis. Aungier [34] assumes that the mass and angular momentum are conserved quantities during the volute design. As the angular momentum is constant along volute passage then the flow will be a free vortex centred at rotor axis. Pullen *et al*. [69] has validated this assumption against the experimental data and found of a reasonable accuracy along the volute.
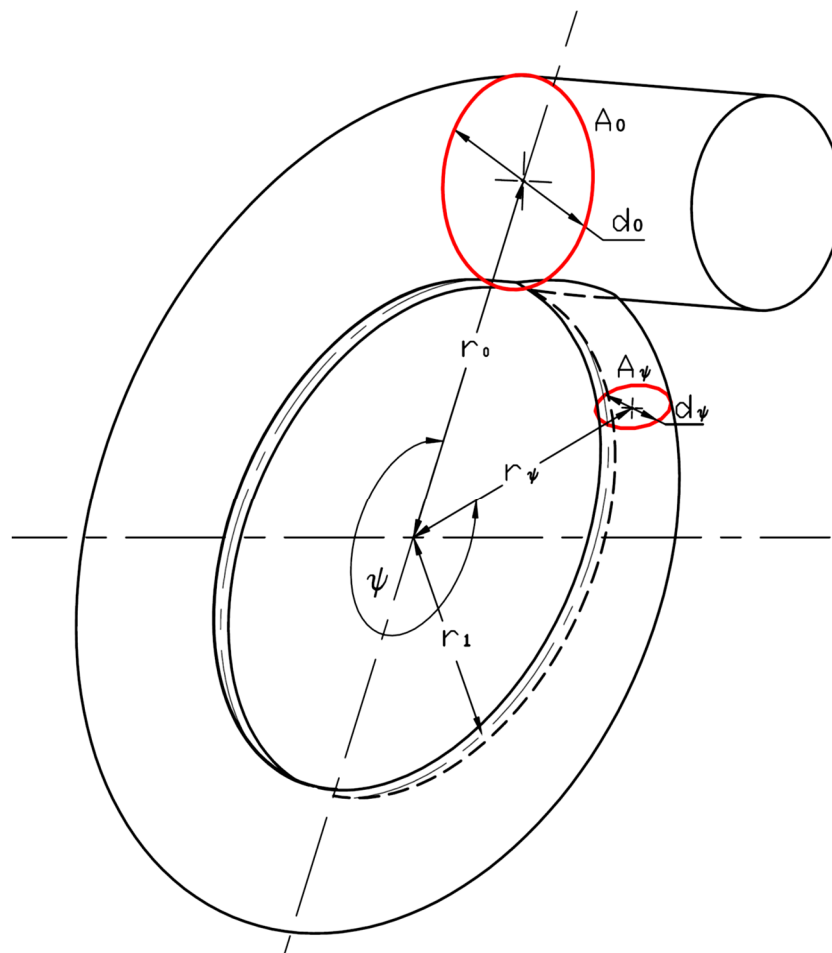
Figure 4.8: Turbine Volute

Based on that assumption, the angular momentum at NGVs inlet can be related to the volute entry ones using equation 4.23.

$$C_{\theta 1} r_1 = C_0 r_0 \tag{4.23}$$

The mass flow enters each cross-section plane of the volute is:

$$\dot{m}_\Psi = \rho_\Psi A_\Psi C_{\theta\Psi} \tag{4.24}$$

To satisfy mass flow uniformity around the volute, the mass flow entering any volute

cross section located at angle Ψ would be:

$$\dot{m}_\Psi = \dot{m}\left(1 - \frac{\Psi}{2\pi}\right) \tag{4.25}$$

Where: Ψ in radians. By combining both equations 4.24 and 4.25 the area to radius ratio

can be written as a function of the azimuth angle Ψ:

$$\frac{A_\Psi}{r_\Psi} = \frac{\dot{m}}{r_\Psi C_{\theta\Psi} \rho_\Psi}\left(1 - \frac{\Psi}{2\pi}\right) \tag{4.26}$$

$$\frac{A_\Psi}{r_\Psi} = \frac{A_0}{r_0}\left(1 - \frac{\Psi}{2\pi}\right) \tag{4.27}$$

The flow angle at the volute exit is:

$$\tan\alpha_1 = C_{\theta 1} C_{m1} \tag{4.28}$$

From equation 4.23, $C_{\theta 1}$ can be substituted by $C_0(r_0/r_1)$, and from conservation of mass

flow, C_{m1} can be replace by $(C_1 \rho_0 r_0/\rho_1 r_1)$, so equation 4.28 can be written as:

$$\frac{1}{\tan\alpha_1} = \left(\frac{A_0}{r_0}\right)\frac{1}{2\pi h_v} \tag{4.29}$$

By rearranging 4.29, the volute entry area to the centroid radius can be calculated using

equation 4.30.

$$\frac{A_0}{r_0} = \frac{2\pi h_v}{\tan\alpha_1} \tag{4.30}$$

From the NGVs design, the volute exit passage height and the desired exit flow angle can

be determined. Implementing those values in equation 4.30, the volute inlet area to radius

ratio can be set. Then using equation 4.27, the area to radius ratio for each cross-section

around the volute can be calculated. This simple method to design the volute is illustrated

in figure 4.9. The last component in the turbine is the exhaust diffuser, the next section describes the design procedure for this component.
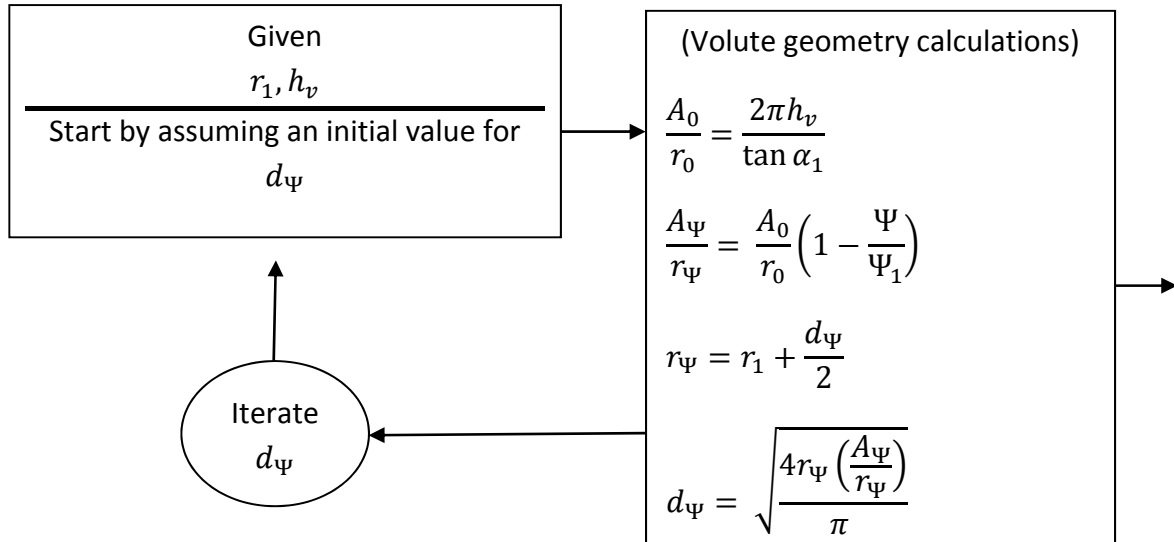
Figure 4.9: Volute design flow chart

4.3.4 Exhaust Diffuser Design

The exhaust fluid exiting the rotor has some kinetic energy which hasn't been utilised within the rotor. Exhaust diffusers are usually attached to the rotor exit to recover this energy. The role of the diffuser is to decrease the static pressure at the rotor exit artificially, to increase the pressure ratio across the turbine stage. Figure 4.10 shows the T-s diagram for the rotor with diffuser, where the diffuser reduces the exit flow velocity to reach zero in the ideal case where the total pressure of the exit flow will be equals to its static pressure and equals to the ambient pressure. Also, the pressure ratio across the rotor is increased from $\frac{P_{03}}{P_5} = \frac{P_{03}}{P_4}$.

Different diffuser configurations are cited in the literature (figure 4.11). Conical diffuser has been chosen for this application because of manufacturing simplicity. Referring to figure 4.11a diffuser geometry can be described by exit to inlet area ratio and diffuser length to inlet radius ratio.

93
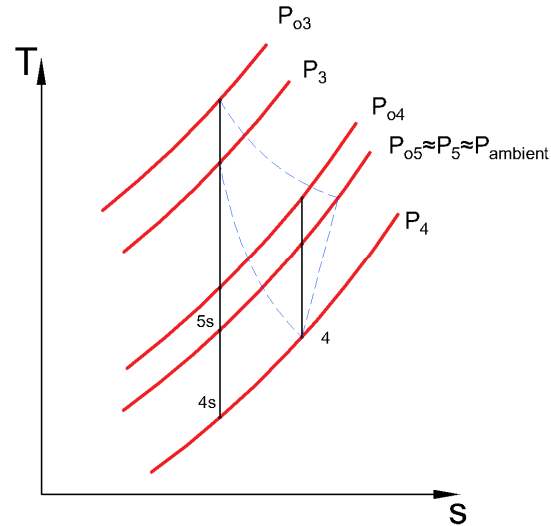
Figure 4.10: T-s diagram for turbine with exhaust diffuser
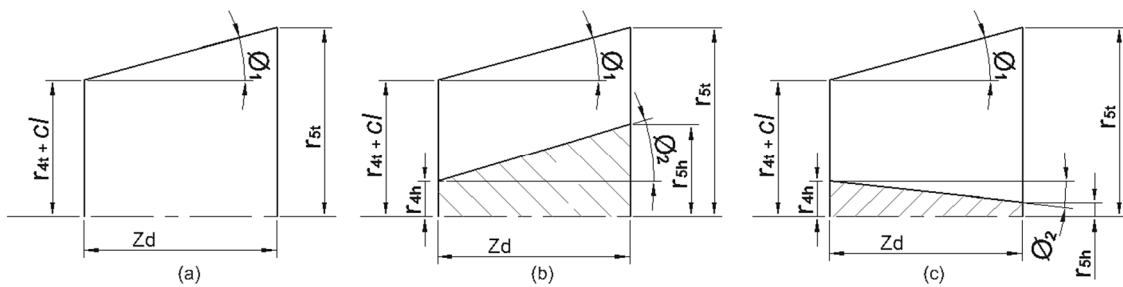
Figure 4.11: Diffuser types (a) conical (b) divergent annular (c) convergent annular

The performance of diffuser depends on the geometrical parameters, Reynolds number, inlet boundary layer thickness, exit swirl angle, blockage due boundary layer and turbulence intensity [6]. At the design point the only know parameter is Reynolds number which is higher than 10^5 and it sits in the region where Reynolds number effect is negligible [70]. Also, the turbine rotor is designed to achieve zero exit swirl so the effect of swirl is assumed to be negligible. Figure 4.12 shows the performance map for conical diffusers of wide range of geometrical parameters.
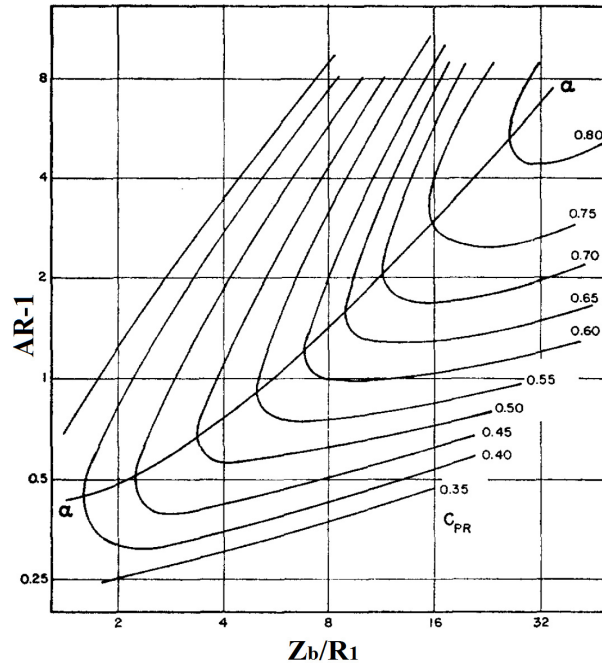
Figure 4.12: Conical diffuser performance map [71]

The design of the diffuser starts by selecting either the area ratio or the length to inlet
diameter ratio, then from the pressure recovery contours the second geometrical
parameter can be found. The best recovery is achieved along the optimum divergence
angel line a-a. Generally, the diffuser recovery coefficient is defined as:

$$RC = \frac{P_{(out)} - P_{(in)}}{P_{o(in)} - P_{(in)}} \tag{4.31}$$

The outputs of the meanline design can be used straight forward to generate the geometry
of the volute, NGVs and exhaust diffuser. However, the rotor geometry needs further
refinement based on the CFD and the Finite Element Analysis (FEA) results. The next
section discusses the procedure followed to generate the rotor geometry.

4.4 Rotor Geometry Generation:

Referring to figure 4.13, the rotor blade is defined by the meridional projection of the hub
and shroud contours, blade thickness along hub and shroud, and the camberline of the
blade defined at the mid span. The hub and shroud projection curves are defined by
Bezier curves with the control points 1-4. The starting and end points defined by the radii

95

and blade heights at rotor inlet and exit. Bezier control points gives the freedom to fine tune the design according to CFD results.
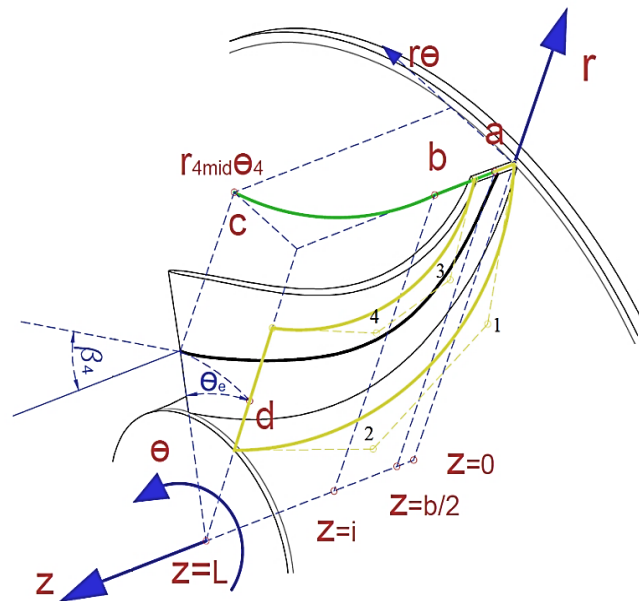
Figure 4.13: Definition of the blade camberline and hub and shroud projection contours

The camberline is defined by the distribution of the angle θ along the z-axis, where θ is the blade angle distribution referred to meridional plane. The θ value was defined as a straight line from points a to b as the blade at the rotor inlet is completely radial, and by a second order polynomial (equation 4.32) from point b to c [67].

$$r\theta = a_o + a_1(z - i) + a_2(z - i)^2 \qquad (4.32)$$

As the turbine blades are radially fibered the slope of the polynomial at any axial position is:

$$\frac{d(r\theta)}{dz} = \tan\beta \qquad (4.33)$$

Then the angle β can be calculated using equation 4.34.

$$\tan\beta = \frac{d(r\theta)}{dz} = a_1 + 2a_2(z - i) \qquad (4.34)$$

To find the coefficients a_o, a_1, a_2 and the distance i, the following conditions at the starting and end points were applied:

$$\theta = 0 \, , \qquad \beta = 0 \qquad\qquad (z = i)$$

$$\theta = \text{blade rac angle at rotor exit}, \ \beta = \beta_{4mid} \qquad\qquad (z = L)$$

The thickness of the blades is defined at the hub and the tip and it is assumed to be linearly distributed along the span. At the shroud, blade thickness was given a constant value along the streamwise direction. Along the hub, the thickness was distributed in parabolic form, where the thickness of the blade at the leading edge was allocated the same value as the shroud. The maximum thickness occurs at 65% of blade length [67]. The final values of blade thickness can be refined using finite element analysis for the rotor.

4.5 Turbine Design for 6 kWe MGT.

The turbine design procedure described earlier has been applied to the design a radial turbine to meet the cycle specifications of 6 kWe MGT. This section discusses the turbine design parameters used. It also shows the design results generated using one-dimensional design program compared with the CFD results.

4.5.1 Design Parameters.

As previously mentioned, one of the objectives of this research is to design radial turbine to be fitted to a 6 kWe MGT for solar application. The cycle analysis was performed by another OMSoP team member. Table 4.1 shows the turbine design point operating conditions resulting from the cycle analysis.

Table 4-1: Design poin Conditions for the Turbine

Parameter	Value
Turbine inlet total pressure (bar)	2.919
Turbine inlet total temperature (K)	1073
Turbine mass flow rate (kg/s)	0.09
Turbine desired output (kW)	21

In table 4.2, the performance parameters needed to be fed to the turbine design are listed. The selection of the rotor design parameters has been justified in section 4.3.1. The selection of the rotational speed came from the cycle analysis of the MGT, as it has been found that the maximum cycle efficiency is achieved at the rotational speed of 13000 rpm.

Table 4-2 : Turbine design parameters

Parameter	Value
Stage Loading Coefficient (ψ)	0.9
Ratio of axial length to rotor inlet radius$\left(\dfrac{Z}{r_{3t}}\right)$	0.56
Exit flow coefficient (ϕ)	0.25
Rotor meridional velocity ratio ($\zeta = \dfrac{C_{m3}}{C_{m4}}$)	1
Exit hub to inlet tip radius ratio $\left(\dfrac{r_{4h}}{r_3}\right)$	0.3
Vane chord to rotor inlet diameter $\left(\dfrac{C_v}{D_3}\right)$ (straight, airfoil)	0.3, 0.35
Vane chord to vane pitch (solidity) $\left(\dfrac{C_v}{S_v}\right)$ (straight, airfoil)	1.2, 1.34
Thickness of vane leading edge to vane chord $\left(\dfrac{tv_{le}}{C_v}\right)$	0.285
thickness of vane trailing edge to vane height $\left(\dfrac{tv_{te}}{h_v}\right)$	0.12
Inter-space geometry parameter $\left(I_g\right)$	2

For the design of straight nozzle guide vanes, the vane chord to rotor inlet diameter (C_v/D_3) was selected to be 0.3 as suggested by Heitt *et al.* [48] The values of the vane chord to vane pitch (solidity) (C_v/S_v) , thickness of vane leading edge to vane chord (tv_{le}/C_v) and thickness of vane trailing edge to vane height (tv_{te}/h_v) where given values of 1.2, 0.285 and 0.12 respectively following the recommendations of Atkenson [67]. The interspace geometry value I_g recommended by Watanabe *et al.* [68] for optimum stator performance and minimum losses was suggested to be two.

For airfoil shaped vanes, the values of (C_v/D_3) was set to 0.35 based on exiting NGVs designs, (C_v/S_v) was similar to the one used in the straight vanes. The value of maximum thickness normalised to chord length was selected to be 15%, and the maximum thickness position normalised to the chord length was 18% from the leading edge.

4.5.2 Preliminary Design Results

Table 4.3 shows the design results obtained from the mean line design process for the rotor and stator vanes. The area and the centreline radius for each circular cross section of the volute at different angle starting from 0° to 360° are listed in table 4.4.

Table 4-3: Meanline design results

Parameter	Design Results	Units
Rotor inlet total temperature (T_{o3})	1073	K
Rotor inlet static temperature (T_3)	962	K
Rotor exit total temperature (T_{o4})	856	K
Rotor exit static temperature (T_4)	842	K
Rotor inlet total pressure (P_{o3})	2.92	bar
Rotor inlet static pressure (P_3)	1.8319	bar
Rotor exit total pressure (P_{o4})	1.067	bar
Rotor exit static pressure (P_4)	1.01	bar
Rotor inlet radius (r$_{t3}$)	0.0367	m
Rotor Exit radius (r$_{4t}$)	0.0237	m
Exit hub radius (r$_{4h}$)	0.0011	m
Rotor axial length (Z)	0.020	m
Rotor inlet height (b_3)	0.004	m
Rotor tip velocity at rotor inlet (U_3)	499	m/s
Flow relative velocity at rotor inlet (W_3)	135	m/s
Absolut flow velocity at rotor inlet (C_3)	467	m/s
Rotor tip velocity at rotor exit (U_{4rms})	229	m/s
Flow relative velocity at rotor exit (W_{4rms})	261	m/s

Absolut flow velocity at rotor exit (C_{4rms})	125	m/s
Specific speed (N_s)	0.5	-
Absolut flow angle at rotor inlet (α_3)	74	Degree
Absolut flow angle at rotor exit (α_4)	0	Degree
Relative flow angle at rotor inlet (β_3)	-21.8	Degree
Absolut flow angle at rotor exit (β_{4rms})	-61	Degree
Absolut flow angle at vane exit (α_2)	76	Degree

Table 4-4: Volute design data

Volute Angle (°)	0.0	30.0	60.0	90.0	120.0	150.0	180.0	210.0	240.0	270.0	300.0	330.0	360.0
Cross section radius (mm)	19.78	18.82	17.81	16.77	15.67	14.5	13.3	12	10.7	9.1	7.3	5.1	0.0

Based on the preliminary design results, the turbine rotor blades and aerofoil shaped NGVs were generated using commercial tool ANSYS BladeGen. BladeGen requires radii at inlet and exit, the hub and shroud meridional curves, blade angle along the camberline, and blade thickness. For the rotor, all the required values were calculated as described in the earlier sections except the hub and shroud meridional curves, where the curves were defined using 3rd order Bezier curve to give a flexibility for the design to be modified according to CFD results. Similarly, for the airfoil shaped NGVs BladeGen requires the leading and trailing edge radii, the camberline angle from the leading edge to the trailing edge and vane thickness normal to the camberline. The camberline angle distribution were defined as a 3rd order Bezier curve, so the throat area and flow angle can be controlled to achieve the required flow angle and mass flow rate. By specifying the values of maximum thickness and maximum thickness position normalised to chord length, BladeGen calculates the vane thickness normal to the camberline based on NACA airfoil thickness distribution. For this

design, the values of 15% and 18% were allocated for the maximum thickness and maximum position respectively.

In Figure 4.14, the designed rotor with it major dimensions are displayed. The rotor was scalloped and some material was removed from the rotor back face to reduce the stresses at the turbine shaft root at rotor back face. This turbine was scalloped more than the amount required to reduce root stresses in order to reduce rotor mass as much as possible in the benefit of the shaft rotordynamics.
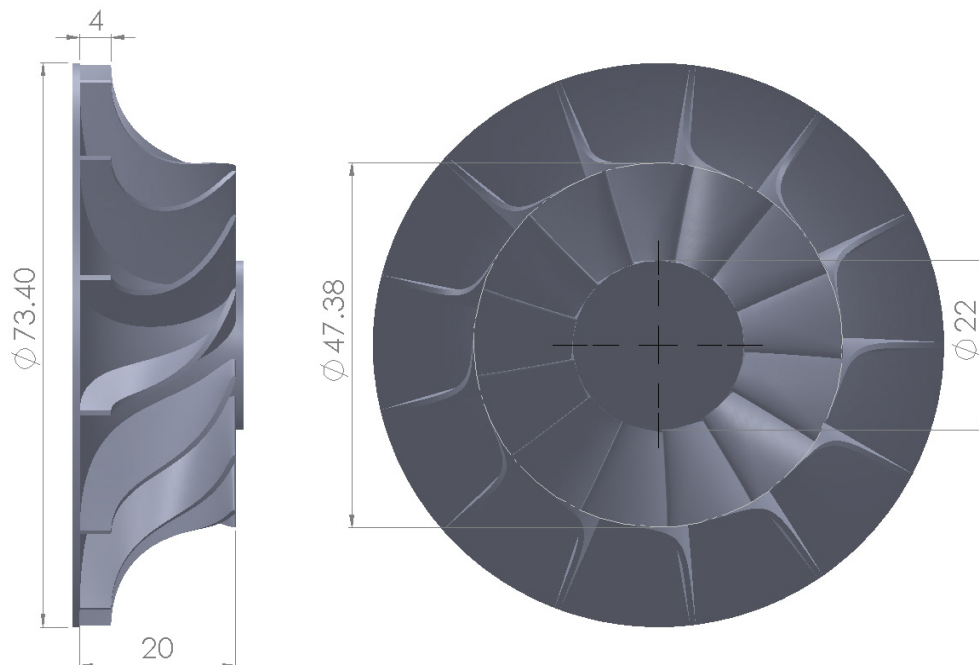
Figure 4.14: Rotor dimensions

Figure 4.15 shows the designed NGVs. Through the design process CFD indicated that the total pressure loss coefficient of the aerofoil shaped NGVs is a 0.04 and 0.08 for the straight NGVs. Therefore, the decision was to proceed with the aerofoil shaped NGVs, also all the results shown now after are using the aerofoil NGVs.
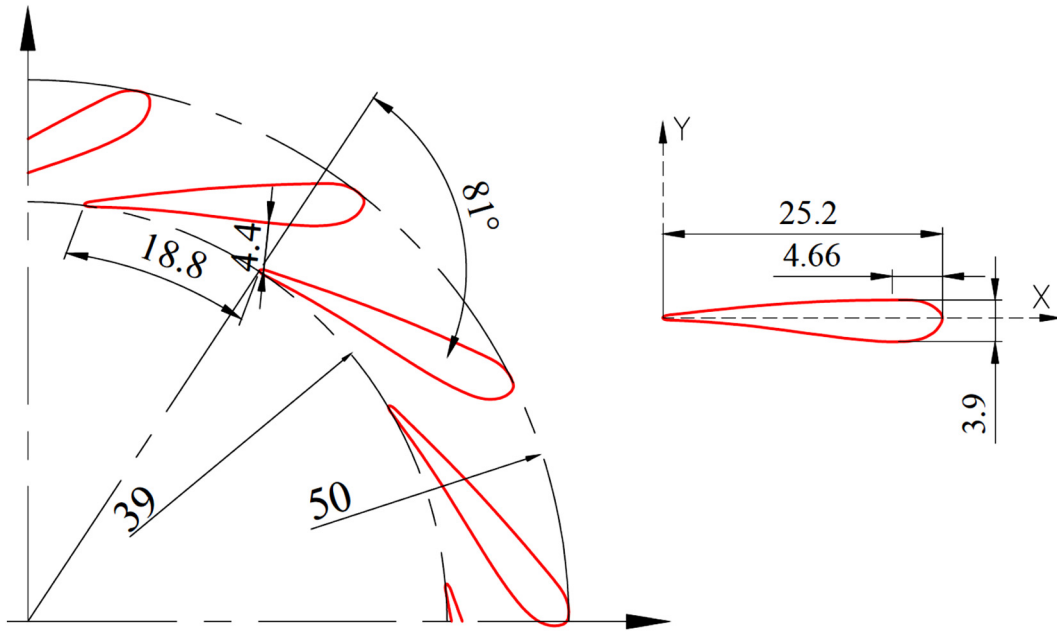
Figure 4.15: Nozzle vanes dimensions

Manufacturing a single volute unit based on circular cross section design requires expensive casting manufacturing process. Therefore, a squared cross section volute with a side length equal to the circular cross section diameter was manufactured.

4.5.3 Numerical Methodology

To tune and verify the turbine design, CFD has been performed on the turbine stage. A single guide vane and single rotor blade have been set as the computational domain for the CFD analysis. The commercial tool ANSYS TurboGrid was used to generate hexahedral structured meshes. The numerical analysis was performed using ANSYS CFX 15.0 solver. CFX is a Reynolds Averaged Navier Stokes (RANS) based solver which solves the flow equations using the finite volume formulation. The flow was assumed to be fully turbulent, this assumption is based on the calculated Reynolds number in the rotor passage. Reynolds number was calculated assuming the flow in the rotor passage as a rectangular duct flow, therefore using the passage hydraulic diameter Reynolds number at the design point is 27000. Dai *et al*. [50], found that turbulence intensity along the rotor passage doesn't

exceed 7%, so 5% has been used in this work. The Shear Stress Transport (SST) turbulence model was used as it showed a good matching with the experimental data for radial turbines [72, 45].

Non-slip boundary condition was set for the passage surfaces. In order to resolve the boundary layer accurately, the near wall mesh was refined to achieve first node non-dimensional distance $y^+ = 1$. Stage connection (mixing plane) is defined between rotor and stator, where all fluxes are averaged through the interface surfaces. Uniform total pressure and temperature were set at the domain inlet and uniform static pressure at the domain outlet. As one vane and one rotor blade passage were used, rotational periodicity was imposed on the periodic boundaries. The tip clearance used is 7% of the blade span, however, this value for larger turbines is around 3%, but because of machining tolerances this small value is not achievable. For this setup, CFX was run for a steady state solution.

4.5.4 Grid Independence Analysis

To ensure mesh independence, a grid independence study has been performed. Two parameters: the mass flow rate and output shaft power were calculated from CFD. Six grids of increasing refinement have been used to calculate theses parameters, starting with a coarse grid of 20000 nodes and ending with a grid of 1,366,922 nodes. The results of the mesh independence study (figure 4.16) shows that increasing number of mesh nodes will not affect the results starting from 832,000 nodes distributed between the rotor and stator domains, hence the stator passage required ~ 200,000 nodes and the rotor passage required ~ 423,000 nodes. The final mesh is shown in figure 4.17.
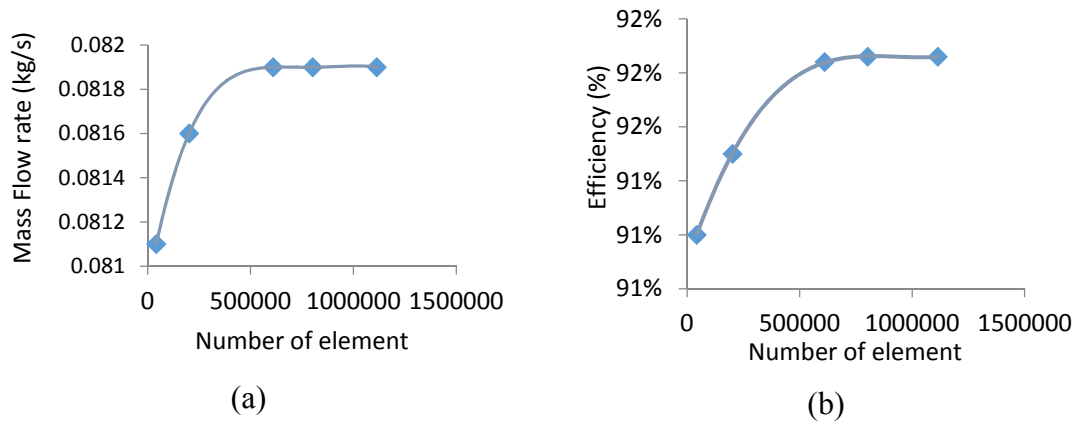
Figure 4.16: Turbine characteristics with different mesh size (a) mass flow rate (b) efficiency
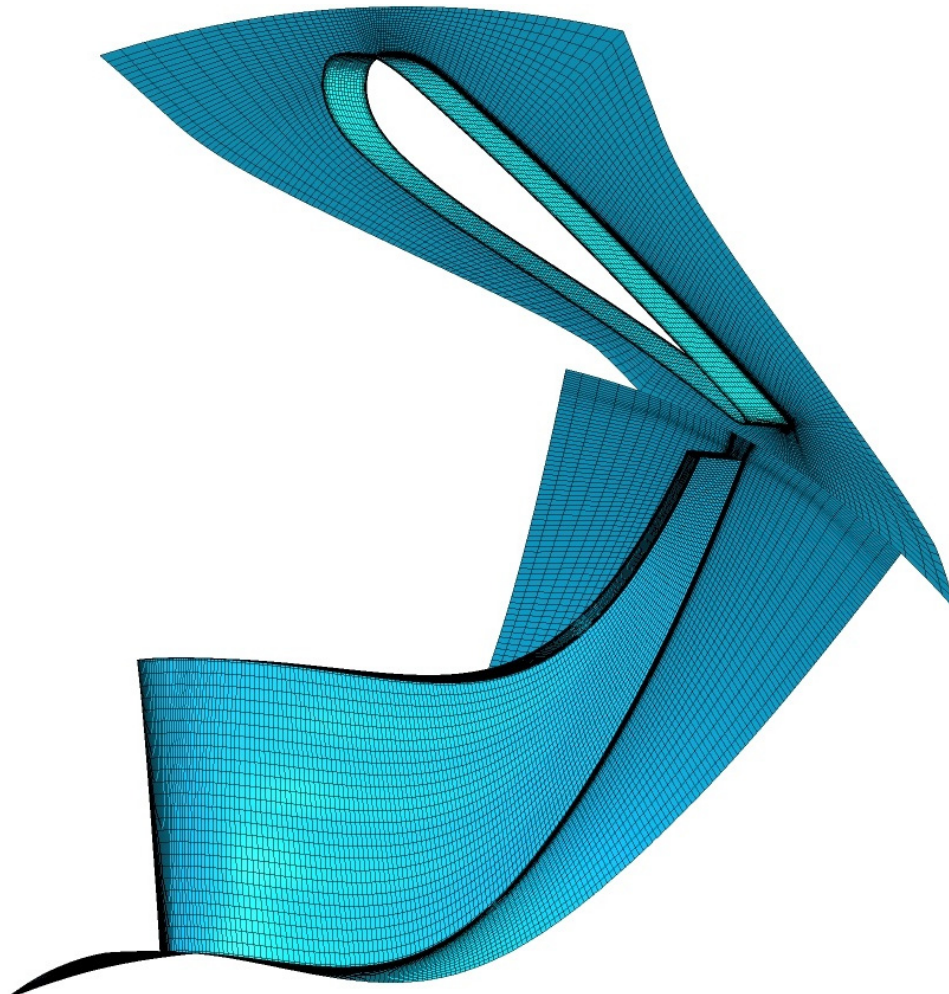
Figure 4.17: Computational domain grid

4.5.5 Turbine Design Validation

Once the numerical analysis for the turbine is concluded, the design characteristics should

be tested against the design requirements to verify the design process. The validation will

be starting with the velocity tringles at the rotor terminals as they are well related to the

machine performance. Figures 4.18 and 4.19 show the velocity triangles at rotor inlet and exit respectively, and the numerical value are compared in table 4.5. These figures compare the CFD results with those obtained from the one-dimensional design process.
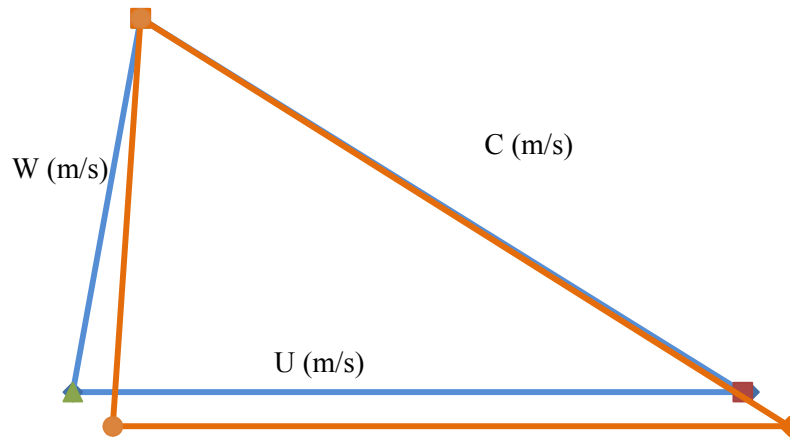
Figure 4.18: Velocity triangles at rotor inlet resulted from preliminary design and CFD results
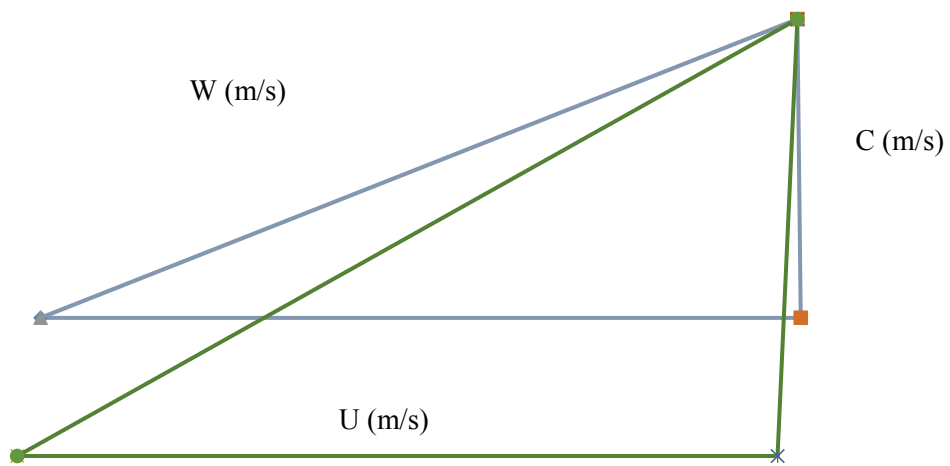
Figure 4.19: Velocity triangles at rotor outlet resulted from preliminary design and CFD results defined at RMS radius

Referring to figure 4.18, the absolute flow angle is matching between the CFD and the one-dimensional results, this indicates that the stator design method is accurate and sufficient to predict the flow angle.

Table 4-5 : Percent difference between the meanline results and the CFD

Parameter	Preliminary design	CFD	% Difference
Rotor Inlet			
Absolute flow velocity	465	497	6.4%
Relative flow velocity	135	142.5	5.3%
Rotor Exducer			
Absolute flow velocity	125	183	31.7%
Relative flow velocity	261	285	8.4%

In both methods: the meanline and the CFD, the rotor has the same inlet area and mass flow, therefore the flow meridional velocity will be inversely proportional to the fluid density. In the meanline calculations, the gas pressure at the rotor inlet was assumed to be similar to that before that at the stator inlet, which results in a higher density value than the CFD. Therefore, in the meridional velocity predicted in the CFD is higher than that of the meanline results.

It can be noticed from figure 4.19 that the same effect has been conveyed to the rotor exit because of the assumption made at the inlet. However, larger difference can be observed between the CFD results and the meanline results (31.7% compared to 6.4%). This increment in the meridional velocity results from the blockage due to boundary layer growth, i.e. flow velocity increase to compensate the flow area reduction due boundary layer blockage at the rotor outlet.

Table 4.6 listed the boundary conditions for turbine design point operation. Implementing those values in the CFD setup for the turbine stage shows that that the turbine achieves the

desired outputs which are listed in table 4.7. The most important target of this design is to achieve the desired power output from the MGT (6 kWe) based on the provided operating condition. While the compressor requires 12 kW to operate and the mechanical and electrical efficiencies are 95% and 90% respectively, 21.5 kWe would be sufficient to generate the targeted 6 kW electric power.

Table 4-6: Boundary conditions used in CFD calculations

Total temperature at domain inlet (Kelvin)	1073
Total pressure at domain inlet (bar)	2.919
Flow angle at domain inlet (degree)	0 (Radial direction)
Rotational speed (rpm)	130,000
Exit static pressure (bar)	1.01

Table 4-7: Overall Performance Results Table

Inlet Mass Flow Rate (kg/s)	0.09
Total to static Pressure Ratio	2.827
Total-to-Total Isentropic Efficiency %	0.83
Rotation Speed (rpm)	130,000
Shaft Power (watt)	21500
Nozzle loss coefficient	0.04

To check the flow behaviour along the turbine passage figure 4.20 was produced to show the velocity vectors at different span heights for the rotor. It can be noticed that the flow vectors are aligned in the streamwise direction, this with performance data assures that the design is fairly good. At 80% of span between 30-60% of blade chord, the flow vectors deviate from the streamwise direction towards the pressure surface.
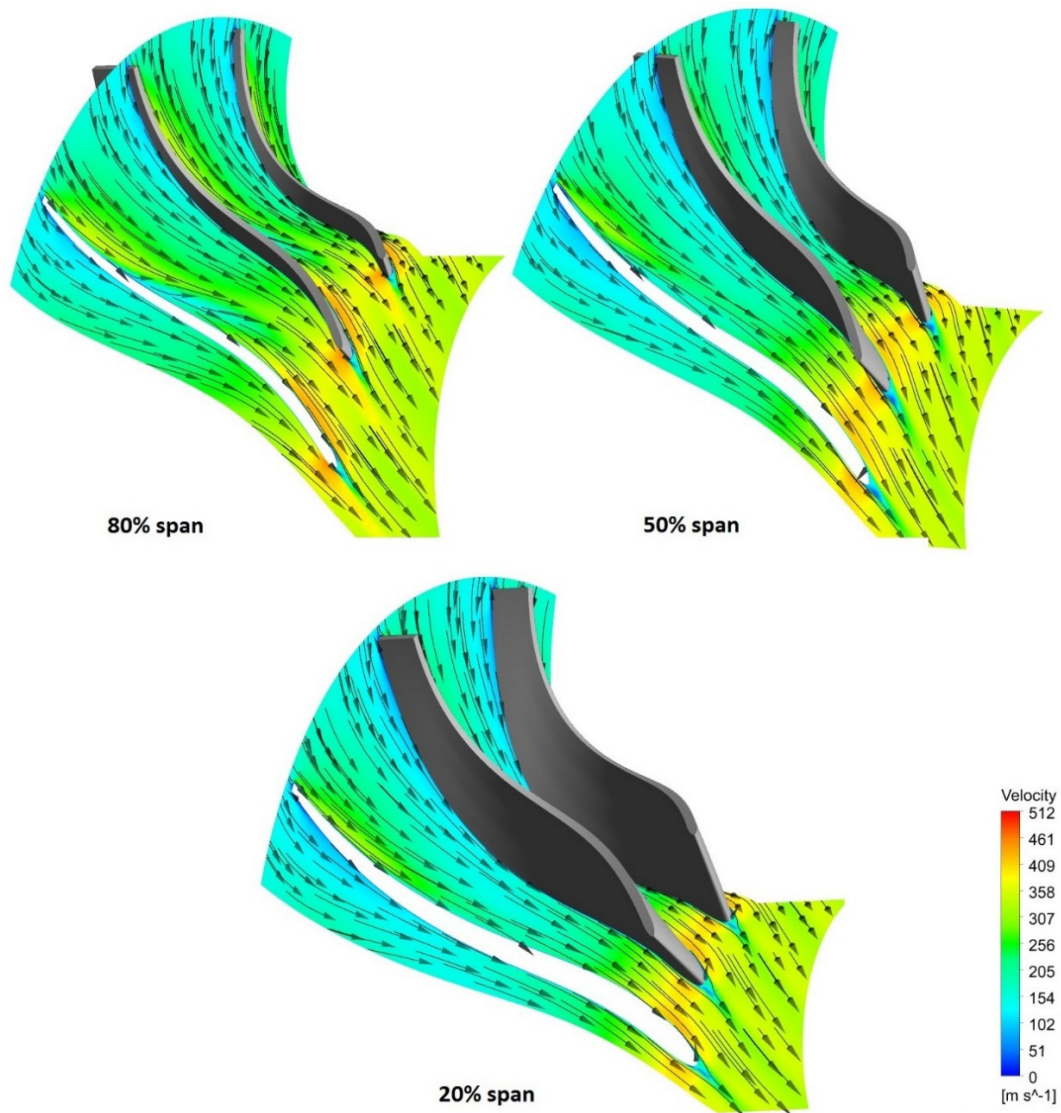
Figure 4.20: Relative velocity contours and velocity vectors along the rotor passage

This deviation is caused from the injection of flow from pressure to suction surface through the tip clearance gap. The mix of this jet flow with the secondary flow vortex at the tip suction side corner leads to an increment in the passage losses within the rotor. This explains the importance of the clearance height at rotor outlet which is the main source of tip clearance loss mentioned in chapter 2.

Figure 4.21 shows the relative Mach number contours at 50% of span for the turbine vanes and rotor. Maximum Mach number is 0.9 this means the flow remains subsonic, and no shock losses are expected.
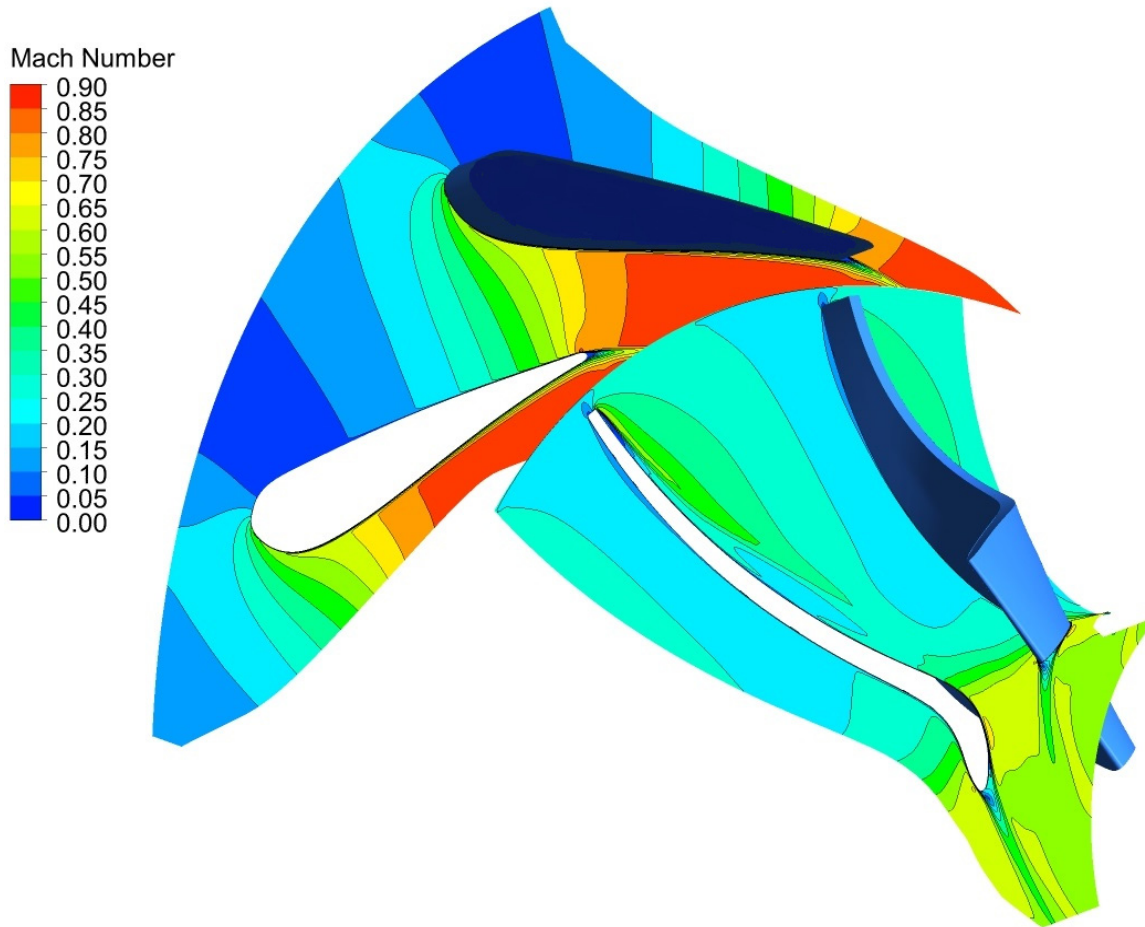
Figure 4.21: Mach number contours at 50% span

Blade loading was plotted at 50% span in figure 4.22 to make sure that no flow separation

occurs and the flow is not forced to reverse direction near the trailing edge. The red circle

is the region where the flow is usually forced to reverse direction because the pressure at

suction surface becomes larger than that on the pressure surface. This pressure reversal

causes losses in the turbine, so in this design this reversal in the pressure has been avoided.

At the rotor inlet, a small pressure jump can be spotted at the suction surface. This pressure

increment is a result of the separated flow caused from the small deviation between the

flow and the blades angle. This can also be spotted in the relative Mach number distribution

at the mid-span of the rotor (figure 4.21), however, the favourable pressure gradient along

the passage causes a rapid reattachment of the flow.
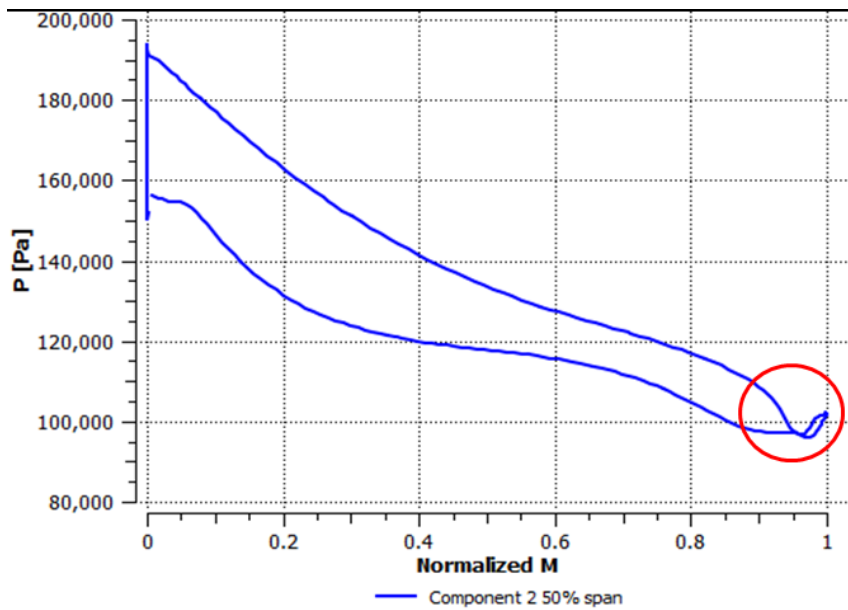
Figure 4.22: Rotor blades loading at 50% span

4.6 Stress Analysis for the Turbine Rotor

Structural analyses for the turbine rotor has been conducted to ensure that it doesn't fail during operation. This has been conducted assuming an operating speed of 130,000 rpm and running temperatures of 698^0C. The temperature used is the relative total temperature of the air at the rotor inlet resulted from the CFD analysis. The meshing and the stress analysis has been performed within ANSYS static structural software. Figure 4.23 shows the results of the analysis for the compressor.
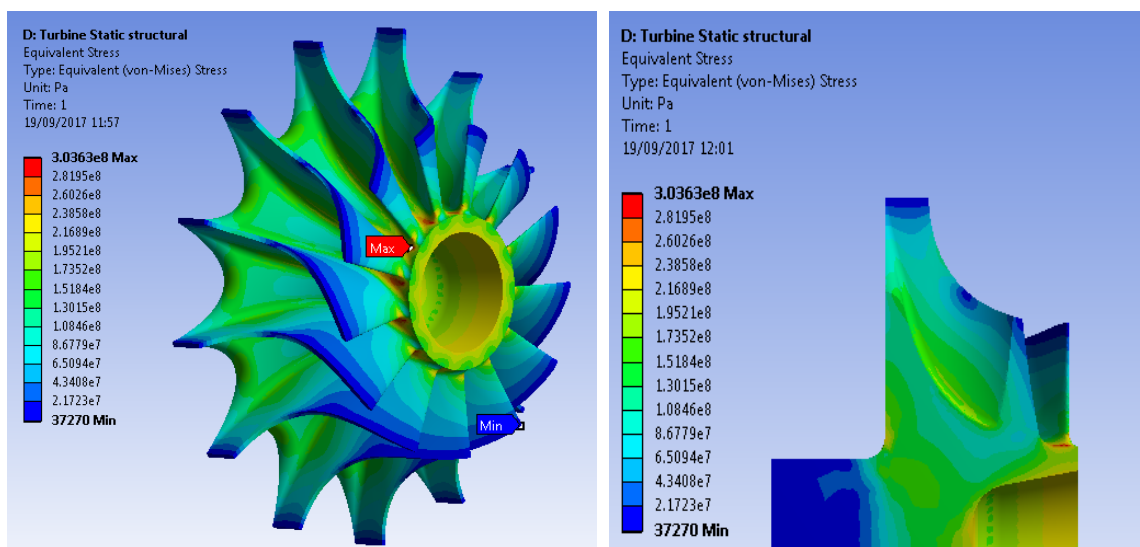
Figure 4.23: Equivalent stress in turbine operating at 130000 rpm and 698^0C

As can be seen the peak stress on the turbine is at the blade root with a value of 303 MPa. Referring to table 4.8, the equivalent stress is below the yield point of Gamma Titanium Aluminide (ɣ-TiAL) alloy at 698 °C. Stresses at the bottom of the hole (added to reduce the rotor mass) are also high but still less than the maximum allowable stress for the (ɣ-TiAL). Similar to the compressor wheel, a LCF and blade vibration analysis have to be performed for the life estimation and the health of the blades of the rotor wheel.

Table 4-8: Gamma TiAl yield stress at different temperatures [73]

Temperature	Yield Stress (MPa)
100	527
300	498
550	475
700	471
800	380

4.7 Performance Prediction Method

The output of the turbine and its performance over its operating range are normally monitored using the performance maps. These maps are of a special importance in the gas turbines applications as they are necessary for matching the turbomachinery components. Therefore, accurate predictions are necessary to be established at the design stage of the machine. In this section, a method is proposed to generate an accurate map for the turbine stage.

In this approach, CFD has been used to simulate a wide range of operating conditions for the turbine. The computational domain included all the turbine parts, but it did not include the clearance between the turbine rotor and the back plate, and rotor walls were assumed to be smooth. With these assumptions, CFD calculations don't account for neither windage nor friction losses, so to compensate for these losses in performance prediction, one-dimensional correlations were used to refine the CFD predictions. This procedure gives more accurate results to predict the performance of the turbine than the one-dimensional methods, which cannot simulate such highly three-dimensional flow accurately. On the

other hand, including the turbine back clearance in the numerical domain requires a very fin meshes and coupling the main flow bath with the clearance gap which, might degrade the accuracy of the CFD if not done properly. All of these induce more complication to the CFD case; therefore, it is believed that the use of the one-dimensional correlations to refine the CFD predictions, will be a fast and a simple method to increase the accuracy of the turbine map.

To evaluate the windage loss caused by the viscous forces of the fluid between rotor back face and the casing, the Daily and Nece [25] formula (equation 2.13) can be used. And for the friction loss within the rotor passage, the Suhrmann *et al*. [74] one-dimensional model can be used. The loss formula he suggested accounts for the friction and the secondary flow losses. Therefore, to calculate the friction loss, the first part of his model was considered in this work, which is shown in equation 4.34.

$$\Delta h_{fr} = K_p \left(\frac{L_H}{D_H}\right) \frac{(W_3{}^2 + W_4{}^2)}{2} \tag{4.34}$$

Where, L_H and D_H are the hydraulic length and hydraulic diameter of the rotor passage.

$$L_H = \frac{\pi}{4}\left\{\left(Z - \frac{b_3}{2}\right) + \left(r_3 - r_{4t} - \frac{b_4}{2}\right)\right\} \tag{4.35}$$

$$D_H = \frac{1}{2}\left\{\frac{4\pi r_3 b_3}{4\pi r_3 + N_b b_3} + \frac{2\pi(r_{4t}{}^2 - r_{4h}{}^2)}{\pi(r_{4t} - r_{4h}) + N_b b_4}\right\} \tag{4.36}$$

The factor K_p has a value of 0.11 for low specific speed turbines $\left(\frac{r_3 - r_{4t}}{b_4} > 0.2\right)$, and 0.22 for high specific speed turbines where $\left(\frac{r_3 - r_{4t}}{b_4} < 0.2\right)$.

After finding the losses due friction and windage, the new value for the turbine efficiency can be calculated as:

$$\eta_{tt} = \frac{\Delta h_{CFD} - \Delta h_w - \Delta h_{fr}}{\Delta h_{CFD}} \times \eta_{tt(CFD)} \tag{4.37}$$

4.8 Performance Prediction Validation

To verify the accuracy of the method used to predict the turbine performance, this was applied to generate the performance map for the designed turbine. Also using this method a performance map generated for the turbine used in Sundstrand Power Systems T-100 Multipurpose Power Unit [75] which is close to the designed turbine in term of size and operating conditions (refer to section 5.4). Figure 4.24 shows the total isentropic efficiency for different pressure ratios at constant non-dimensional speed ($N/\sqrt{T_{o1}} = 2747$). Non-dimensional speed is used because the turbine test is run cold at low speed because of the test rig limitations (full test details are given in chapter 6). Performance prediction method (CFD & 1-D) shows a very good matching with the experimental data for pressure ratios greater than 1.42. For lower pressure ratios, the predicted values are fairly far from the test rig data. One of the main sources of this difference in the use of the non-dimensional speed to simulate those points. During the test, it has been noticed that decreasing turbine inlet temperature to achieve higher non-dimensional speed the efficiency drops down, however increasing inlet temperature and increasing speed to reach the same point results in noticeable better performance. Further discussion of the test data is presented in chapter 6 after applying the uncertainty analysis on the rig data. On the other hand, the CFD predictions are far from the experimental data for the whole range of pressure ratios where the minimum difference is 8.4% at pressure ratio of 1.46. Using the proposed prediction method, this error is was reduced to 0.1%, which shows the importance of using this method to update the CFD predictions.

Figure 4.25 shows predicted and test rig data for T-100 turbine, where the predicted results matches accurately the performance of the turbine at constant pressure ratio and different speeds. On the same figure, the initial CFD results where plotted to show the big difference between the CFD predictions and the experimental ones. Between the CFD data and the

experiments, the error ranges between 6.2% - 7%, while the error between the experiments and the CFD & 1-D method ranges between 0.3% - 1%. This difference again reveals the importance of using the proposed method to update the CFD results to improve the turbine performance predictions accuracy. For both turbines; the designed one and the T-100 power unit turbine the CFD & 1-D was able to predict their performance with a good accuracy, which indicates the validity of the proposed method to predict the turbine performance.
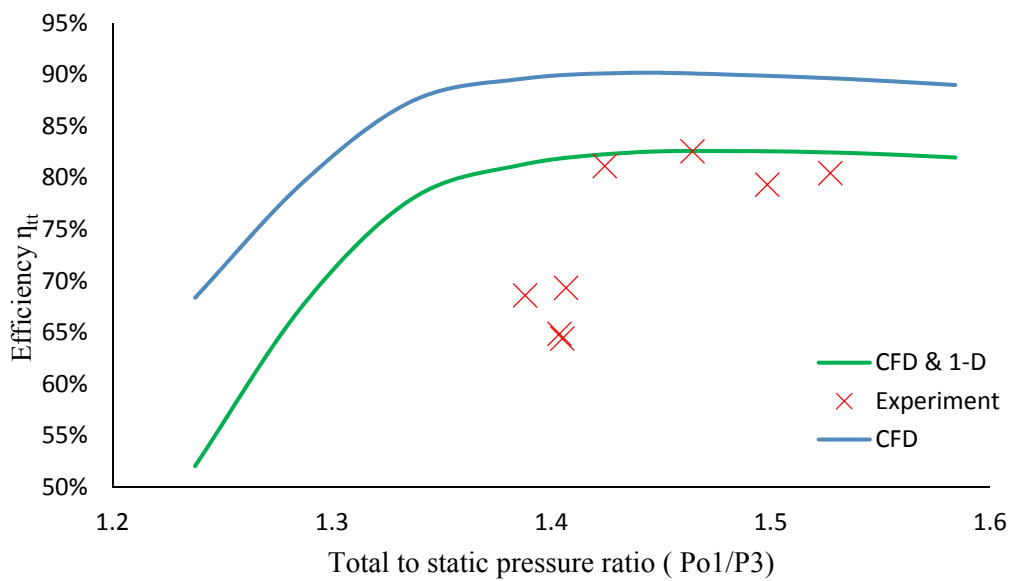
Figure 4.24: Turbine performance map
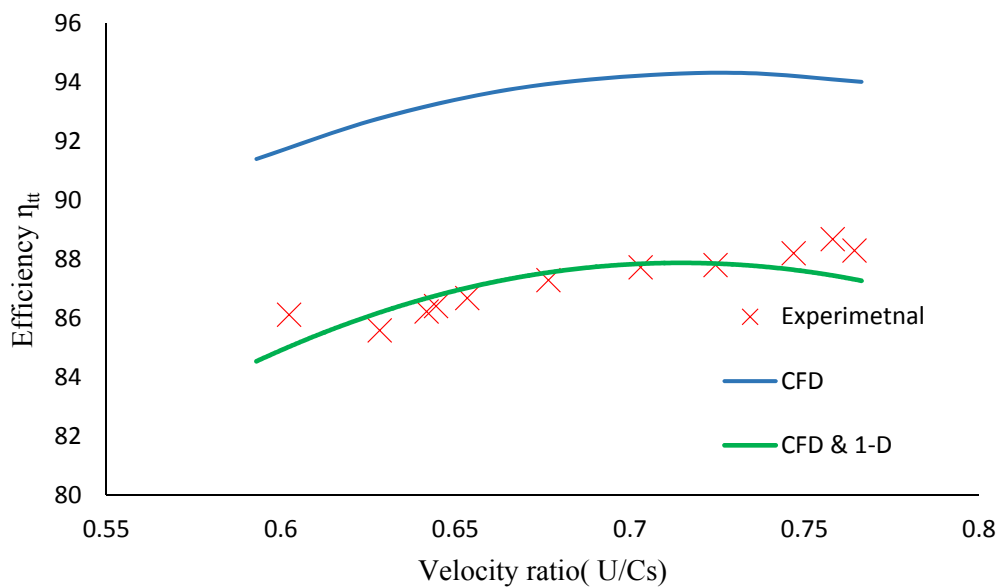
Figure 4.25: T-100 turbine performance map (for pressure ratio 5.7)

Conclusions

Within this chapter a methodology for radial turbine design has been presented and was successfully employed to generate the turbine components geometry for a 6 kWe MGT. The limitations of the CFD to predict accurately the turbine performance have been addressed. Turbine designers normally avoid adding the back face clearance to the computational domain and treat the rotor walls as smooth surfaces to remove geometrical and numerical complexity of the numerical domain. In this chapter, a new method to refine the CFD predictions of the turbine was proposed. In this method, the losses due to the back face clearance and the surface roughness of the impeller are calculated using the loss correlations available in the open literature. The designed turbine has been manufactured and tested in a purpose built test rig, where the actual performance map was generated. The comparison between the actual and the predicted data revealed a good match between both results, which indicates the validity of the demonstrated performance prediction method.

Chapter 5

5. End-Wall Features Effect on Radial Turbines Performance

5.1 Introduction

In this chapter, a novel idea of reducing turbine rotor friction losses through adding riblets to the rotor hub is explored thoroughly. Computational Fluid Dynamics has been used to study the effects of those features at design point conditions of the MGT. Riblets with different height and spacing have been examined to determine the riblet geometry where the maximum drag reduction is achieved. The relative height of the riblets to rotor inlet blade height was introduced to generalise the results. At the end of this study the results were compared with the available data in literature.

5.2 Riblets as Secondary Flow Control Mechanism

Flow within the radial turbine rotor is highly three-dimensional and is combined with strong secondary flows, which become more complicated near the passage walls. The interaction between the turbulent boundary layer and the solid surfaces affects the boundary layer development and causes energy losses due to skin friction drag. The surface profile is one of the important factors that affect the flow within the boundary layer, therefore many researchers focused on studying the effect of implementing engineered structures to control the flow near the solid walls. Riblets are surface structures with different shapes and arrangements as shown in figure 5.1, where they are normally arranged in the streamwise direction. They have proved their ability to reduce the wall skin friction within the turbulent boundary layer.

Walsh [76] studied experimentally the effect of adding riblets to a flat plate surface on drag reduction. Three different riblets geometries were used in the test: V-shaped, trapezoidal and cusp shaped riblets. The relative height of riblets and the spacing between them to the boundary layer thickness were changed during the experiment by changing the free stream velocity of the flow. The test revealed that riblets with certain height and spacing can reduce the viscous drag of the boundary layer where the maximum drag reduction achieved was 8% using V-shaped riblets.

To test the effect of adding riblets to compressor blades surfaces Oehlert *et al*. [77] fabricated trapezoidal riblets on a compressor blade surface using two different machining technologies: grinding and laser machining. The tested blades were part of a linear cascade in a wind tunnel. Ribs produced by both methods were able to reduce the total pressure loss coefficient by 3.6%. Feng *et al*. [78] conducted an experiment to test the effectiveness of riblets on drag reduction where they achieved 10% drag reduction by adding the riblets to the pressure surface of an axial compressor cascade. They also investigated the effect of

changing the flow incidence angle upon riblets drag reduction effectiveness, where they found the drag reduction performance is insensitive to the degree of incidence.

Trying to investigate the effectiveness of riblet on drag reduction for internal flows, Bushan et al. [79] found that adding riblets to a straight rectangular duct has a negative impact on drag. In their experiment, blade shape riblets with different heights and spacing were attached to the duct wall, and the pressure drop was measured across the duct for range of flow velocities. For all riblets arrangements and along the speed range the pressure drop was higher compared to the surface without riblets.

Zhang et al. [80] explored the potential of using engineered riblets on axial turbine hubs to improve their performance. The study was performed using numerical methods and experimental testing. The experiment was conducted in a low speed linear cascade, where V-shaped riblets were fabricated to the hub surface of the turbine passage and aligned in the streamwise direction. The study revealed that riblets can reduce pressure side of the horse-shoe vortex, and alleviate the growth of the passage vortex. In a different experiment carried by Govardhan et al. [81] single fence blade was added to the end walls of turbine cascade. The pressure side of the horse shoe vortex was weakened and the accumulation of the low energy fluid near the suction side corners was reduced in the passage with fence compared to smooth passage. Thus, the total pressure loss coefficient was reduced.

Using CFD, Zhong et al. [82] compared the secondary flows in an axial compressor cascade with and without endwall fence. Fence with different height, length and pitch location were introduced to the passage walls. The numerical results showed that the passage vortex is weakened in the passage with fence, and the maximum loss reduction can be achieved using the fence with length of 75% of the axial chord length and height of one third of the entry boundary layer thickness located at 30% of the pitch from the pressure side of the blades.

Kim *et al*. [83] used an approximation method for the aerodynamic efficiency to optimise the geometry of the endwall fence geometry to achieve the minimum pressure loss and heat transfer through passage walls. The numerical optimisation was carried on a single fence introduced to a 90º turning duct wall to mimic the effect of riblets on axial turbomachines passages. The mass-weighted average total pressure loss within the duct with was reduced by 8.6% using the optimised geometry relative to the duct without the fence. However, the fence increases the end wall heat transfer compared to smooth walls duct.

Miao *et al*. [84] investigated numerically the potential of blade and cusp shaped riblets to reduce the secondary losses within a 90º duct passage. Different number of ribs were investigated in the research: 1, 3, 5 and 7 distribute evenly from the centerline of the passage, where they cover the whole length of the turning. The height of the ribs was kept constant as 0.7 relative to the boundary layer height at the entry of the turning. Those features were found to form a barrier that impede the cross-stream movement of the low momentum fluid near the wall. Therefore, the secondary losses are reduced by weakening the streamwise vorticity that is formed by the rollup of the low energy fluid swiping from the pressure surface of the duct to the suction surface. Increasing number of ribs found to be beneficial as it resulted in weaker passage vortex.

The riblets concept has been also applied to the radial turbomachines. Where Lei *et al*. [85] numerically studied the flow within the centrifugal compressor with different riblets height and number attached to the impeller hub. They found that using riblets aligned in the streamwise direction decreases wall shear stress by restricting the low energy fluid motion from pressure side to suction side along the passage. The maximum drag reduction was achieved using 17 ribs of height 0.58 relative to impeller exit blade width. The numerical results were confirmed by testing the actual impellers in a purpose-built test rig. It is important to mention here that the riblets were fabricated using a ball end milling cutter.

(a) Bladde Riblets   (b) V-Shaped Riblets

(c) Trapozoidal Riblets   (d) Cusp (scalloped) Riblets
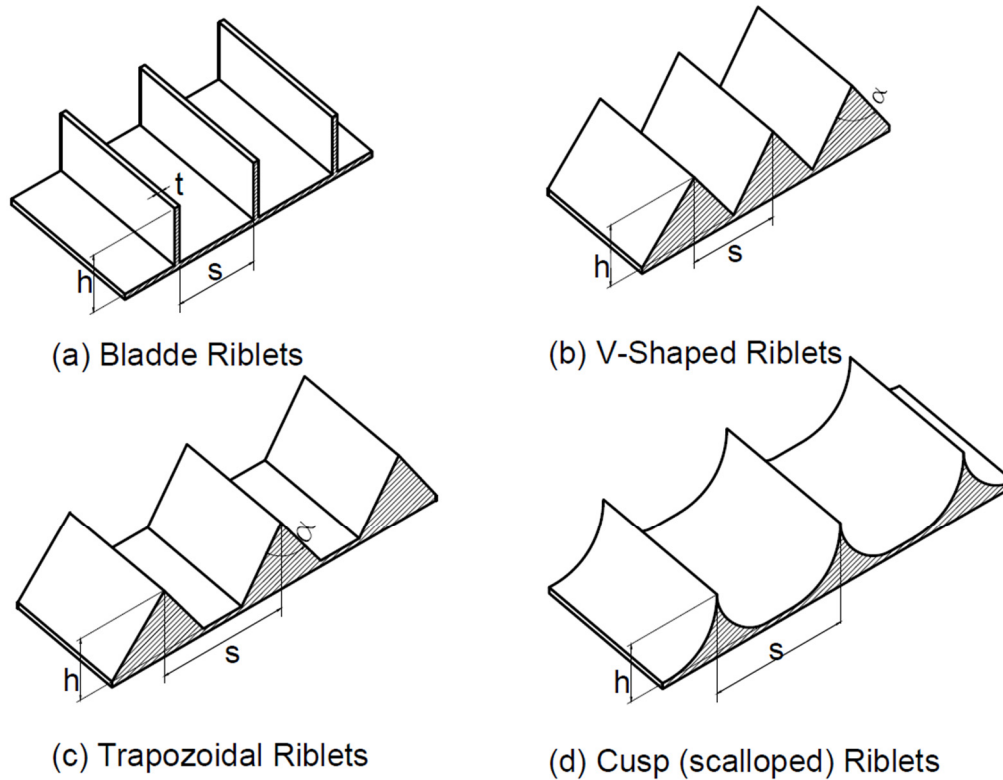
Figure 5.1: Different riblet configurations

From this review of the previous studies on riblets, it is obvious that there is a significant potential of using such features to reduce the secondary losses in radial turbines rotors. Therefore, this chapter is devoted to investigate numerically the ability of using riblets to control the secondary flows within the turbine rotor passages and enhance the turbine performance by reducing skin friction losses. This study will also address the effect of changing the geometry and arrangement of those features on their performance.

5.3 Numerical modelling and Case Setup

Walsh [76] investigated the effectiveness of several riblet geometries on drag reduction where he found that the highest drag reduction could be achieved using riblets with cusp shape. In a different study, Oehlert *et al.* [77] found that riblets with blade shape have greater effect on drag reduction over the cusp shaped riblets. Nonetheless, blade riblets can neither be machined nor they would withstand high stresses. Moreover, the residual surfaces resulted from the actual machining process of the turbine rotor are very similar to

cusp riblets. Figure 5.2 shows rotor sample machined using ball end cutter milling with different surface finish, where cusp riblets are clear in the magnified surfaces. So, the present work focused on studying the effect of cusp shape riblets as they are practically achievable.
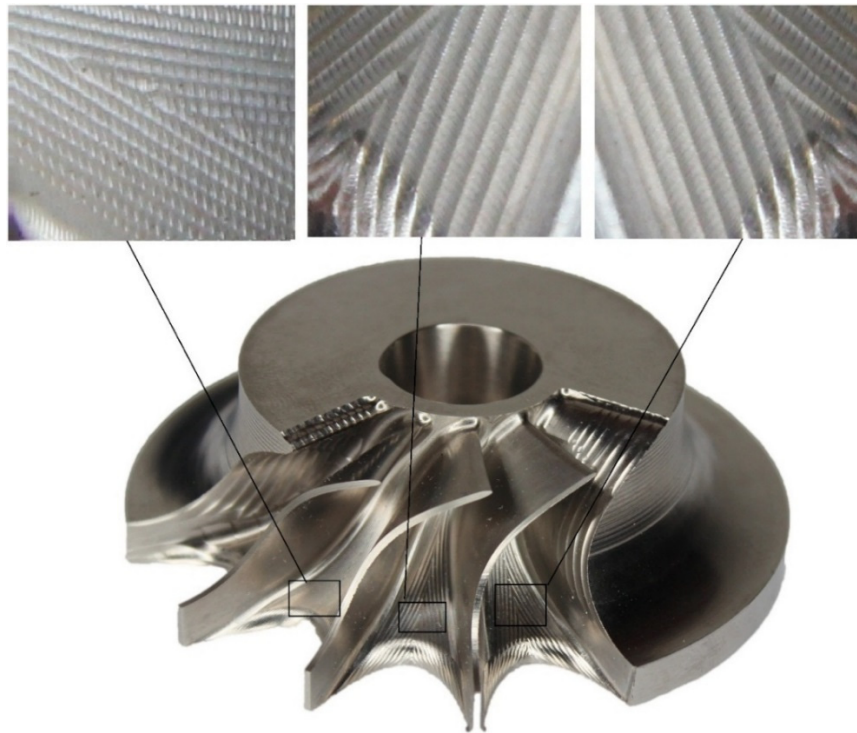
Figure 5.2: Turbine rotor with three different hub surface finish

To the knowledge of the author, the effects of the residual surface structures on the radial turbines performance were not addressed before, therefore it was important to include riblets with different geometry in the study. It is understood from the literature that the main geometrical parameters that affect the riblets performance are the height of the riblets and the spacing between them. Therefore, riblets with different heights (h) and spacing (s) were introduced to the hub surface of a turbine rotor designed in chapter 3. The turbine stage was then analysed numerically at design point conditions listed in table 1.

Table 5-1: Turbine specifications

Parameter	Value
Total Pressure Ratio (bar)	3

Turbine inlet total temperature (K)	1073
Turbine mass flow rate (kg/s)	0.09
Power generated by turbine (kW)	21
Rotational speed (rpm)	130,000

To generalise the results of the study, the dimensionless parameter h_{rel} was introduced to characterise the size of the riblets. h_{rel} is defined as the percentage ratio of the cusp height h to the rotor inlet blade height b (figure 5.3). The space between riblets was defined using the polar angle ($\emptyset$) between the adjacent riblets as the area of the passage is changing along the streamwise direction. Thus, the distance s can be calculated at certain radius of the hub as:

$$s = r_{hub}\emptyset \qquad\qquad (5.1)$$

The detailed dimensions for the riblets used in this study are summarised in Table 5.2.
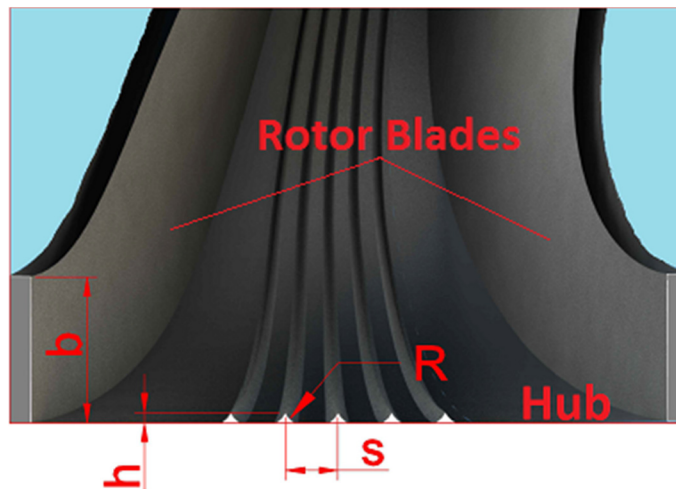
Figure 5.3: Riblets terminology
Table 5-2: Riblets dimensions

h [mm]	h_{rel} [mm]	R [mm]	s [3 riblets] $\emptyset = 4.45°$	s [5 riblets] $\emptyset = 2.2°$	s [10 riblets] $\emptyset = 1.1°$
0.06	1.5%	0.8	0.078r_{hub}	0.039r_{hub}	0.019r_{hub}
0.1	2.5%	0.6	0.078r_{hub}	0.039r_{hub}	0.019r_{hub}
0.2	5%	0.6	0.078r_{hub}	0.039r_{hub}	0.019r_{hub}

The computational domain included the single rotor blade and single nozzle vane. The stator vane was included to mimic the real situation of the turbine. TurboGrid has been used

to generate hexahedral structured mesh for the stator passage, where Workbench meshing tool was used to generate unstructured mesh for the rotor passage. The numerical analysis was performed using CFX 15.0 solver with the same setup presented in section 4.5.3. Grid independence check was performed for both numerical domains (smooth and ribbed rotors). For the rotor with riblets, the grid independence study was performed on the rotor with the highest cusp and smallest space as it requires the highest quantity of grid nodes to model those features. Using five grids of increasing refinement, the absolute vorticity, mass flow rate, flow velocities and angels at rotor inlet and outlet were calculated and compared. For the domain with riblets, the girds density varied between 400,000 and 2 million nodes, and for the rotor without riblets, the density was between 0.4-1.7 million nodes. Figure 5.4 shows the percentage difference in calculating the vorticity referring to the value generated using the finest grid. Vorticity showed the highest sensitivity to grid refinement, this is due to the small turbulent structures that needed fine mesh to be captured. For the domain with riblets the difference is reduced to less than 1% with the mesh of 1.2 million nodes, and for the domain without riblets the difference is reduced to less than 0.9% using the grid with 900k nodes. The final mesh for both rotors is shown in figure 5.5.
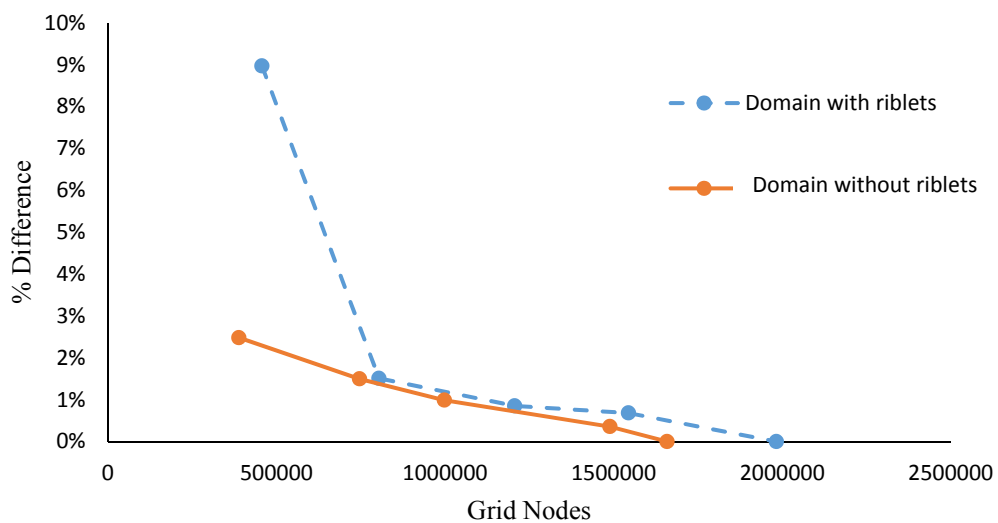
Figure 5.4: Grid independence study for computational domain with riblets

(a)

(b)
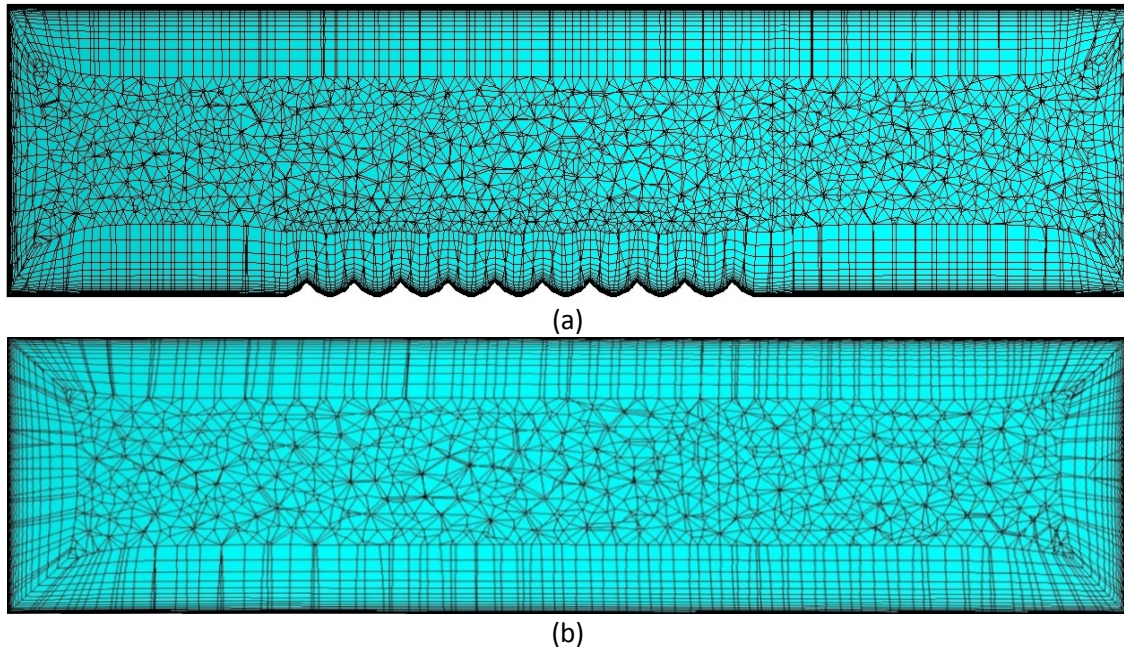
Figure 5.5: Computational grid (a) rotor passage with ribs (b) rotor passage without ribs

5.4 CFD Approach Validation

To verify the accuracy of the numerical method used, flow solutions were compared with experimental data. Experimental studies describing the flow within the turbine rotor are scarce. One of the main reasons for that, is difficulty to insert measuring instruments and the lack of the optical access to the rotor passage. Also, the high operating temperatures is another obstacle in front of using different flow visualisation techniques. Moreover, most of the published experiments does not have an adequate information to regenerate the geometry. Jones [86] provided the experimental data and the geometry description for the turbine used in Sundstrand Power Systems T-100 Multipurpose Power Unit. The turbine generates 50 horse power at pressure ratio 5.5 and a turbine inlet temperature 1056 K while running at 105,600 rpm which is very close to the turbine used in this study. The absolute flow angles at the rotor exit are compared in figure 5.6, where CFD results show a good agreement with the experimental results. However, CFD predictions deviate from the experimental near the tip region. This difference could be due to the rotor back-face clearance flow which was not included in the numerical domain. Sun *et al*. [87] noticed

124

similar deviation in the flow angle predicted using CFD when they studied the effects of back-face clearance gap on the flow in the turbine passage. Figure 5.7 shows a comparison between CFD and test rig results for the span-wise distribution of meridional velocity at the rotor exit. It can be noticed that the difference between the values is almost constant, which means that this deviation is related to the over estimation of the mass flow in the CFD analysis.
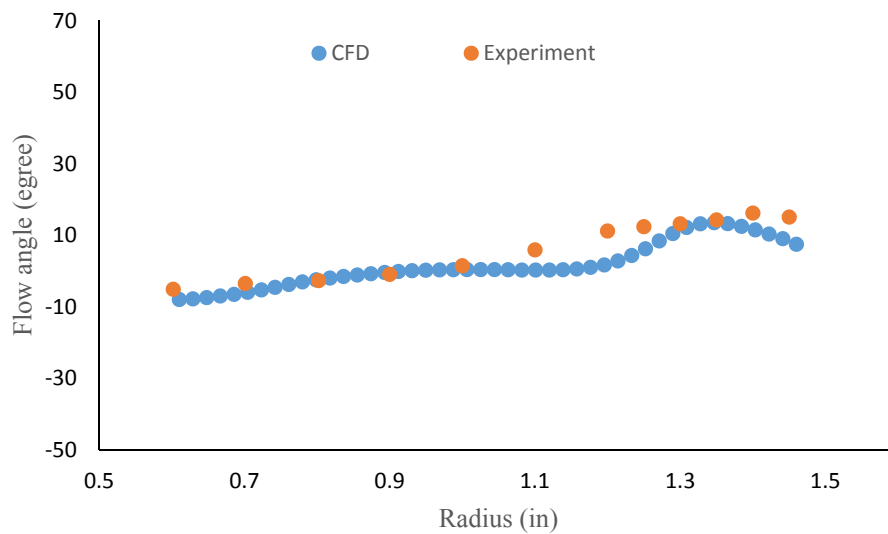
Figure 5.6: Spanwise distribution of rotor exit flow angle
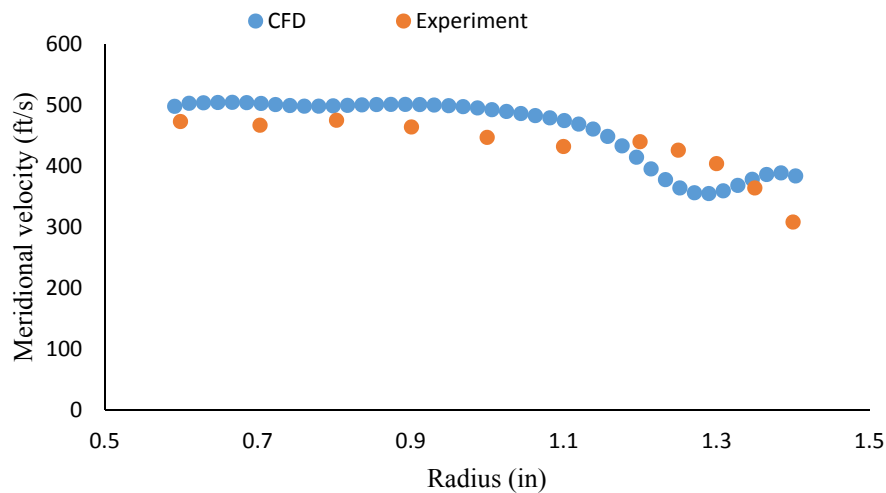
Figure 5.7: Spanwise distribution of the meridional velocity at rotor discharge

This could be because of the assumption of smooth profile of the turbine components, which will reduce the boundary layer blockage allowing more flow to pass. Moreover,

during the test, the flow is expected to leak through the back-face seal of the turbine which could reach up to 1% of mass flow. Generally, the simulation results agree with the experimental data. Therefore, the present CFD methodology was considered to be suitable to study the flow behaviour through the turbine rotor, and is capable to demonstrate the effect of adding riblets on the turbine performance.

Nonetheless, this validation process is not the best way to justify the capability of the CFD method use to capture the changes in the flow physics caused by riblets. In order to validate the CFD calculations, two sets of experimental data are needed to be compared with the numerical results. The first set is the experimental results for a turbine rotor with smooth walls similar to the data provided earlier in this section. The second set is the experimental data for a rotor with wall features. Comparing these sets of data with the numerical results, gives a confidence that CFD method used is capable to detect the performance change resulted by adding similar features to the turbine rotor. This wasn't possible in the current study because of the lack of such experimental data.

5.5 Results and Discussion

This section presents a description for the secondary flow motion in radial turbine passage, operating mechanism of riblets and comparison of different riblets geometries on drag reduction.

5.5.1 Secondary Flow in Radial Turbine Rotor

In the literature; authors divided secondary flow characteristics in a turbine rotor into three categories based on their location along the passage. At the inlet section where the flow is purely radial, Coriolis acceleration has a very large effect on the low momentum fluid at the hub and shroud; therefore it acts to move flow from the Pressure Surface (PS)

to the Suction Surface (SS) where the reduced static pressure ($P_r = P_s - \frac{1}{2}\rho\omega^2 r^2$) is minimum. Along the rotor bend, where the flow starts to change its direction from radial to axial, secondary flows are generated because of both passage rotation and curvature. Coriolis acceleration is responsible for the movement of the low energy fluid from PS to the SS at the hub and shroud surfaces. Also, the passage curvature acts to move the low energy fluid at the pressure and suction surfaces from hub to shroud. For a fluid particle that is moving along the bend with a particular velocity there is a pressure gradient acting normal to its direction of motion to balance the centrifugal force on it. This pressure gradient is constant along the spanwise direction while the near wall fluid particles have a lower velocity than particles in the free stream. This difference in velocity causes the near wall particles to move toward the inner curve to reduce the radius of curvature [88]. Towards the end of this section, the secondary vortices at the hub start to move towards the top middle of the passage.

At the exducer section, the rotor passage is curved in the tangential direction. This curvature causes the low momentum fluid at the hub and shroud to swipe towards the SS where the curvature radius is minimum. Also, the radial component of the Coriolis acceleration causes a movement of the low energy fluids at the PS and SS from hub to shroud.
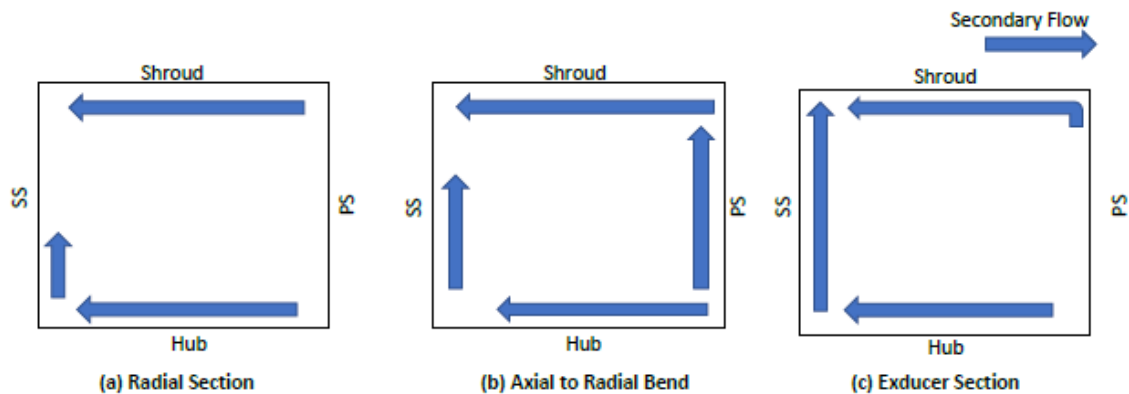
Figure 5.8: Secondary flow motion along turbine rotor passage

In this section, the secondary vortices accumulate in middle and top parts of the passage close to the suction surface. Figure 5.8 illustrates the motion of the low momentum flows at the different sections of the rotor passage [89].

5.5.2 Riblets Operating Mechanism

To understand the operating mechanism of riblets, the flow structure is compared between ribbed and smooth hub rotor passage. In this section, the smooth hub surface was compared with surface with 5 riblets of h_{rel} 2.5%. Figure 5.9 shows the secondary-flow motion at the hub surface at 40% cross plane.
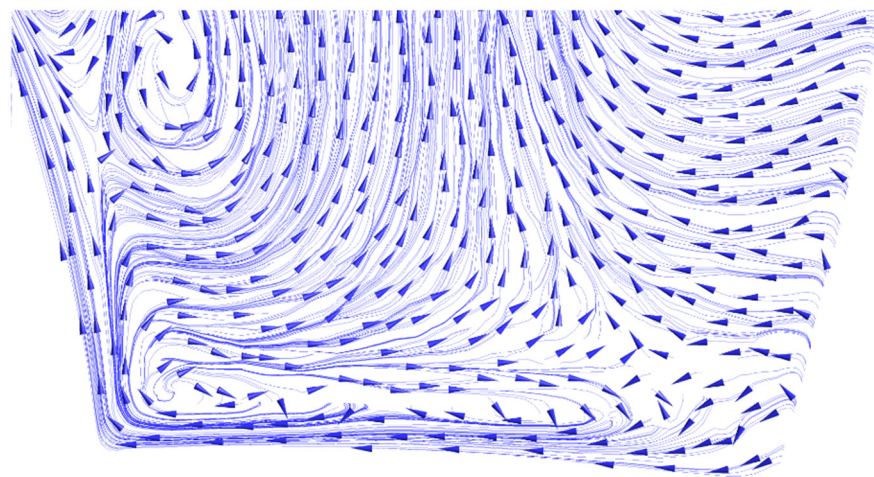
(a) smooth hub
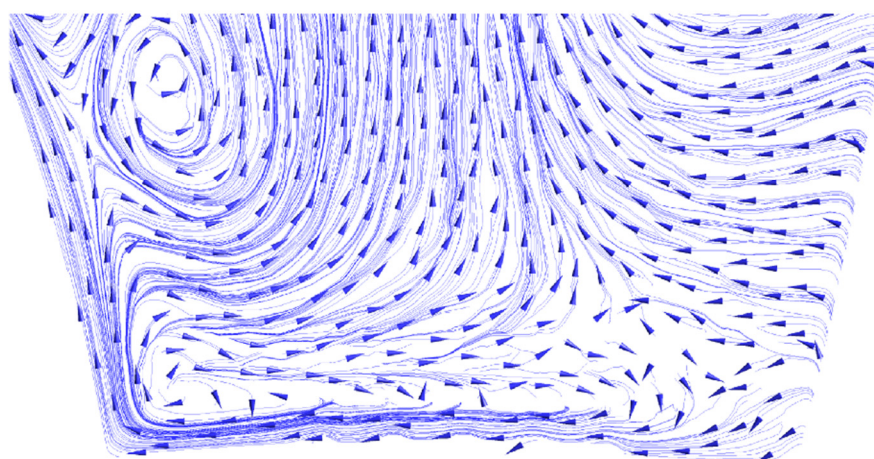
(b) ribbed hub

Figure 5.9: Effect of riblets on cross stream motion of the low energy fluids near the hub surface

It can be noticed that the cross-stream flow interacts with the riblets at the hub surface impeding it movement and generating secondary vortices that prevent the streamwise vortex from moving inside riblets valley. This will retain the slow fluids inside riblets valley thus the momentum exchange in the boundary layer is reduced. The interaction between the stream wise vortex and the low momentum fluid close to the hub causes high local shear at the rotor hub surface. By introducing riblets to the wall, this vortex is shifted from the wall to interact with the riblets tips.

This interaction generates secondary vortices which weaken the streamwise vortex by interfering with the cross-stream motion of the low momentum fluids at the hub surface and keeps the streamwise vortex away from the wall. This reduction of the cross-flow fluctuation and shifting the streamwise vortex away from the wall reduces the turbulent momentum transfer which results in reducing skin friction. The limiting streamlines (velocity streamlines at a distance normal to the wall approaching zero) at the hub surface in figure 5.10b shows the strong relative motion of the low energy fluids at the hub surface. Introducing riblets to the hub surface (figure 5.10a) form an obstacle which retards the cross-stream motion and tries to align them in the streamwise direction.

In figure 5.11, the Q-criterion method [90] was used to visualise the streamwise vortex over smooth and ribbed hub surfaces at 40% cross plane. As it can be seen; the interaction between the cross flows and the riblet tips generates small vertical structures at the pressure side of the riblet cusp. Those vortices block the cross stream motion of the secondary flows, retain the low velocity fluid within the riblets valley and prevent the passage vortex movement inside the valley.

(a) Hub with Riblets   (b) Smooth Hub
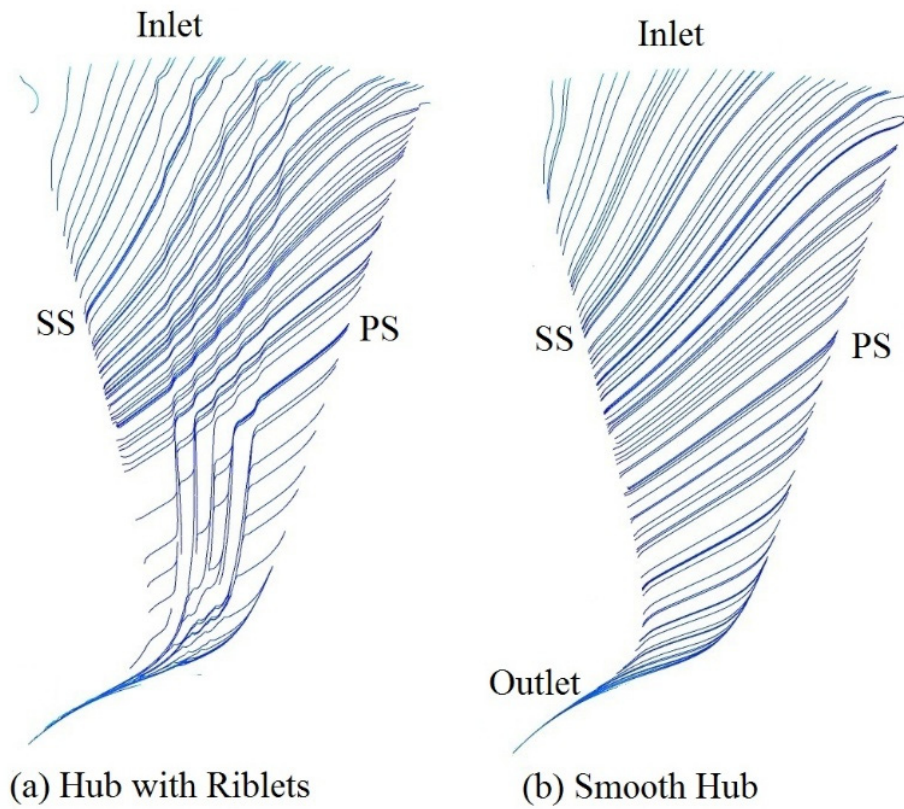
Figure 5.10: Limiting streamlines at the rotor hub

(a) smooth hub

(b) hub with riblets
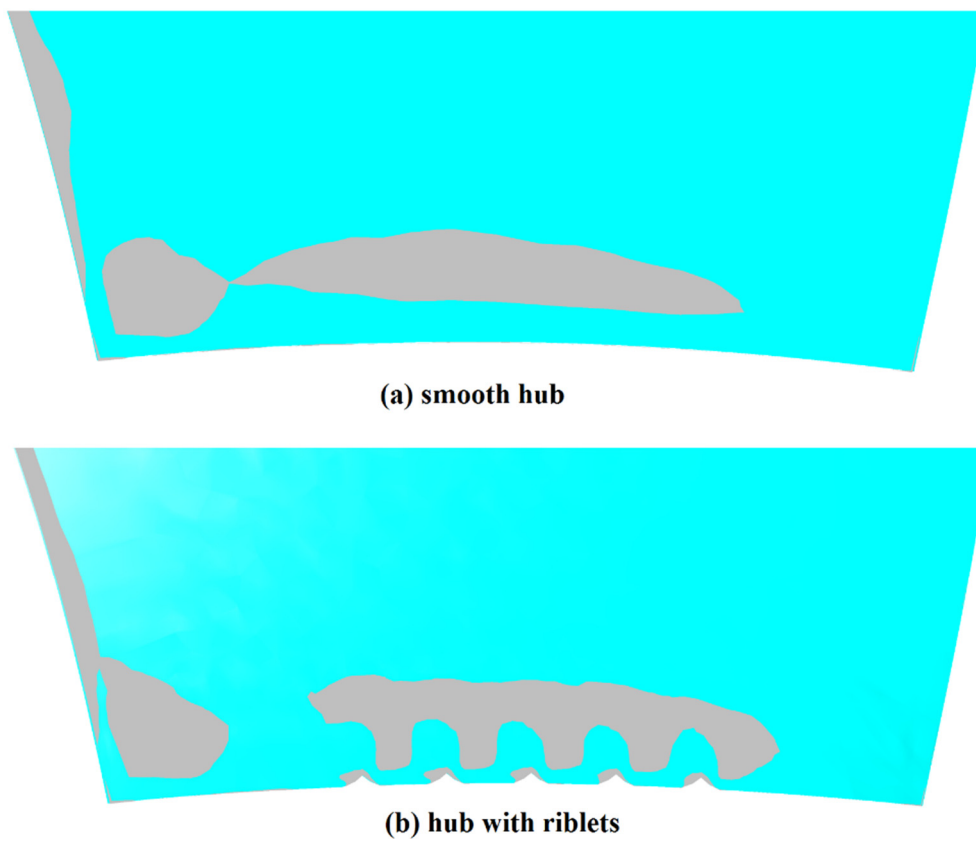
Figure 5.11: Stream-wise vortex structure over hub surface

The mass averaged vorticity normalised by multiplying by (Inlet blade height (b)/ Inlet flow velocity) is presented in figure 5.12.
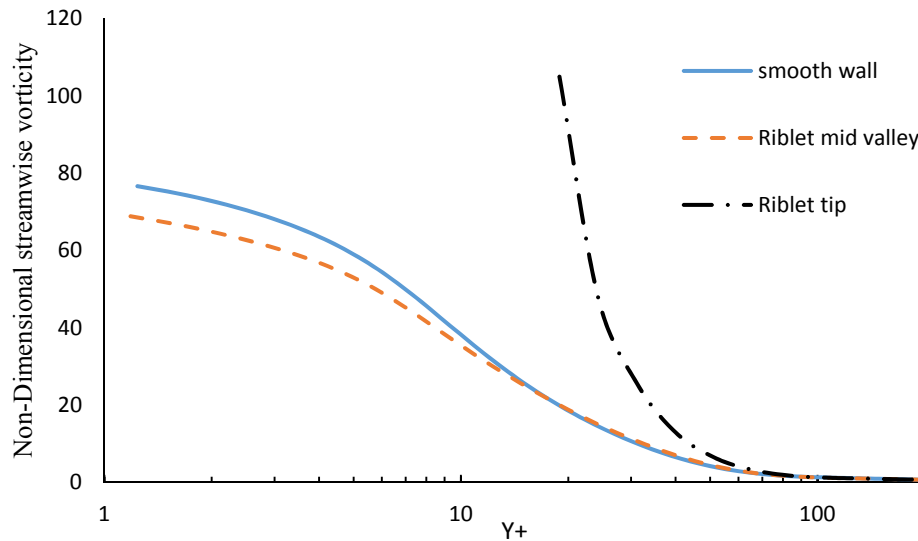
Figure 5.12: Mass averaged streamwise vorticity at 40% stream-wise location

The vorticity value shows a noticeable reduction inside the riblets valley compared to the smooth surface which confirms that riblets weaken the streamwise vortex close to hub surface. However, the vorticity at the outer region of the riblets valley is slightly higher because of the secondary vortices generated at the riblets tip. At the tip region, the vorticity reaches its maximum value in the region where the secondary vortices are located. Nonetheless the secondary vortex close to riblet tip does not have a significant effect on increasing skin friction as the vortex size is relatively small and it interacts with very small area at the peak of the riblet.

To evaluate the effect of increasing the vorticity at riblets tips on skin friction, the wall shear was calculated along the hub surface at the 40% plane. Figure 5.13 reveals that increasing the vorticity at riblets tips increases the wall shear at small areas around the tips, while the wall shear inside the riblets valley is reduced keeping the average shear below that for the smooth surface. Close to the pressure side of the valley, the drag friction is higher than the rest of the valley because of the secondary vorticial structures.

Thus, increasing the height of the rib will generate stronger secondary structures which penetrate into the valley resulting in higher friction drag than smooth surfaces.
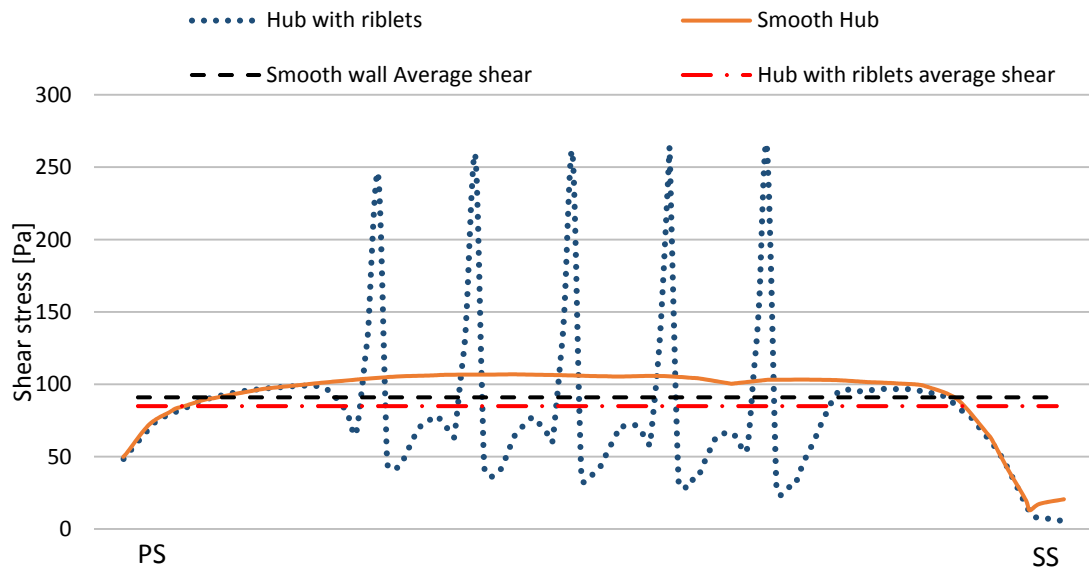
Figure 5.13: Wall shear at the hub surface calculated at 40% stream-wise location

The turbulent kinetic energy profiles over smooth hub, riblets valley and riblet tip are plotted in figure 5.14. It is obvious that introducing the riblets to the hub surface damps the velocity components fluctuations leading to reduction in turbulent kinetic energy. Chun *et al.* [91], Lee *et al.* [92] and Duan [93] have spotted similar drop in turbulent kinetic energy when riblets were introduced to flat plate surfaces.
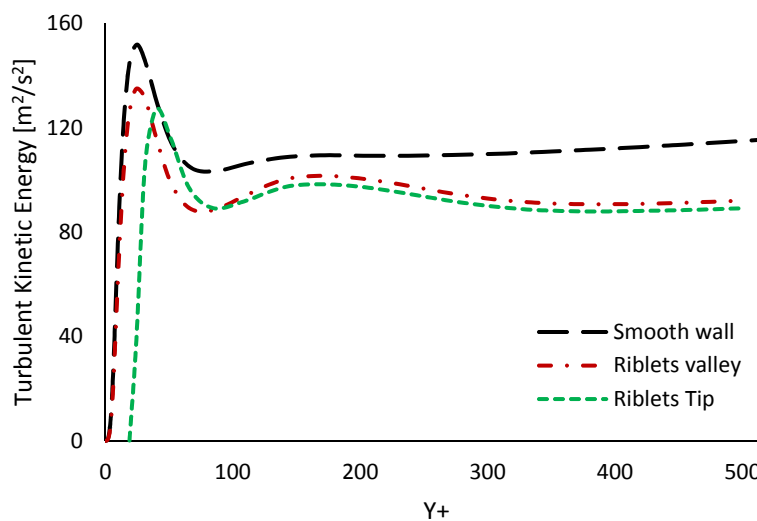
Figure 5.14: Comparison of turbulent kinetic energy for both smooth rotor and rotor with riblets

5.5.3 Riblets Geometry Effect

In this section, the effect of different riblets geometries (refer to table 5.2) on drag reduction is examined and compared with the smooth wall results. Figure 5.15 compares the area averaged shear at the hub surface for the riblets with different height and spacing. The results reveal that the spacing between riblets has a minor effect on the wall shear stress reduction and the key parameter that affects the riblets performance is their height. The highest drag reduction was achieved using riblet with relative height 2.5%, whilst increasing riblet height to 5% has a negative impact, where drag increases at the hub surface. Walsh [94], Chen *et al*. [91] and Bechert *et al*. [95] [72] showed that effect of Reynolds number on the performance of riblets on the drag reduction could be expressed in terms of non-dimensional riblet height and riblet spacing expressed in wall units $h^+ = \frac{h u_\tau \rho}{\mu}$, $s^+ = \frac{s u_\tau \rho}{\mu}$ respectively, where μ is the dynamic viscosity, ρ is the density and u_τ frictional velocity defined as $\sqrt{\tau_s/\rho}$ (τ_s is wall shear stress). According to those studies riblets reduce drag for normalised spacing $s^+ < 30$ and normalised height $h^+ < 25$ wall units.
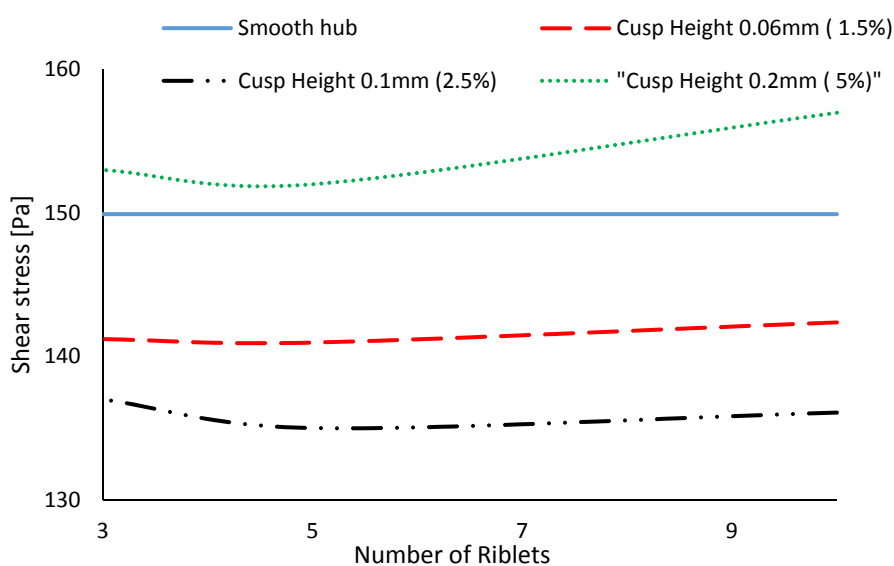
Figure 5.15: Wall shear stress comparison between different riblets geometries

Figure 5.16 presents the change in drag ($\Delta\tau$ defined in equation 5.2) for riblets with different spacing s^+ and constant height ($h_{rel} = 2.5$, $h^+ = 19.3$).

$$\Delta\tau = (\tau_r - \tau_s)/\tau_s \qquad\qquad (5.2)$$

Where, τ_s and τ_r are the wall shear stresses at the smooth and ribbed hub surfaces respectively. The graph shows that the spacing s+ has a negligible effect on riblets performance, it shows also that riblets can reduce drag for high values up to 300 wall units. This conflicts with the values in literature and the value presented here is mainly due to the type of the flow. Most of the available experimental data that limits riblet spacing to 30 wall unit are done for external flows. This is directly related to the streamwise vorticity at body surface, where size of the streamwise vortices for external flows is about 30 wall units in diameter. Therefore, increasing the space between riblets to more than that will provide the freedom for the streamwise vortex to move freely in the area between them. This will cause increment in area exposed to high speed cross flow which in turn increases skin friction [92]. On the other hand, the streamwise vortex at the turbine hub occupies almost the whole passage width, therefore increasing the spacing s^+ didn't change the performance of the riblets (see figure 5.11).
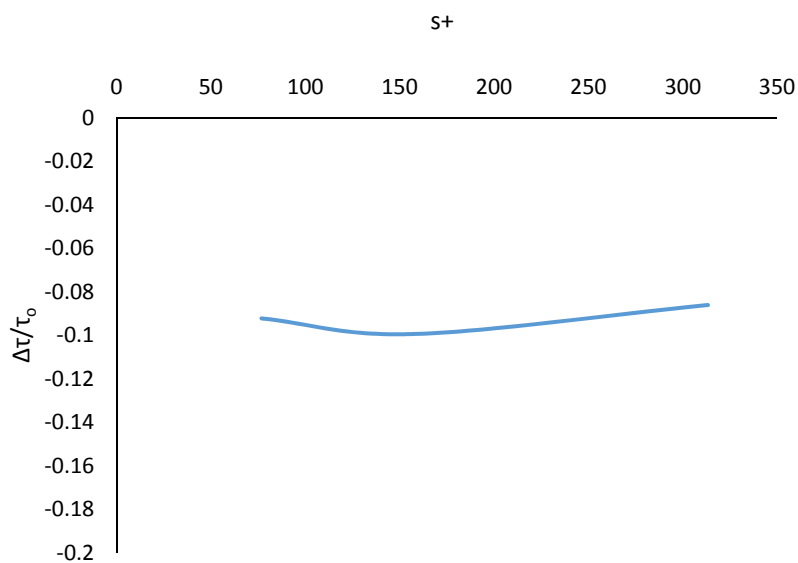
Figure 5.16: Drag reduction for different riblets spacing

Figure 5.17 presents the change in drag for different riblets height h^+ at constant rib spacing $(s = 0.039r_{hub}, s^+ = 158)$. Wall shear using riblets is reduced until reaching the rib height $(h^+ = 19.3)$ where the wall shear is minimum, while increasing riblets height further leads to increase the wall shear. A similar trend for riblets performance within internal flows was spotted by Lei *et al*. [85], where the drag reduction was found to be related to riblet height. Increasing riblets height increases the generation of secondary vortices which increases the down washing motion of the high-speed fluids around riblet tip causing more drag.
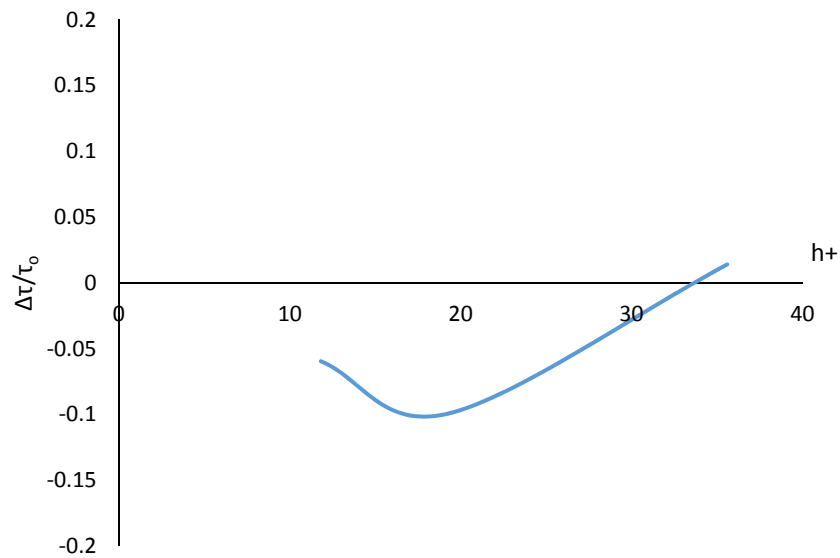
Figure 5.17: Drag reduction for different riblets height

Figure 5.18 shows the mass averaged streamwise vorticity along the turbine passage. The graph shows that increasing the height of the riblets increases the streamwise vorticity along the passage. This explains the performance results in figure 5.19 where the turbine with riblets of height $h_{rel} = 1.5\%$ has a higher efficiency than $h_{rel} = 2.5\%$ even the latest shows better performance in reducing drag.
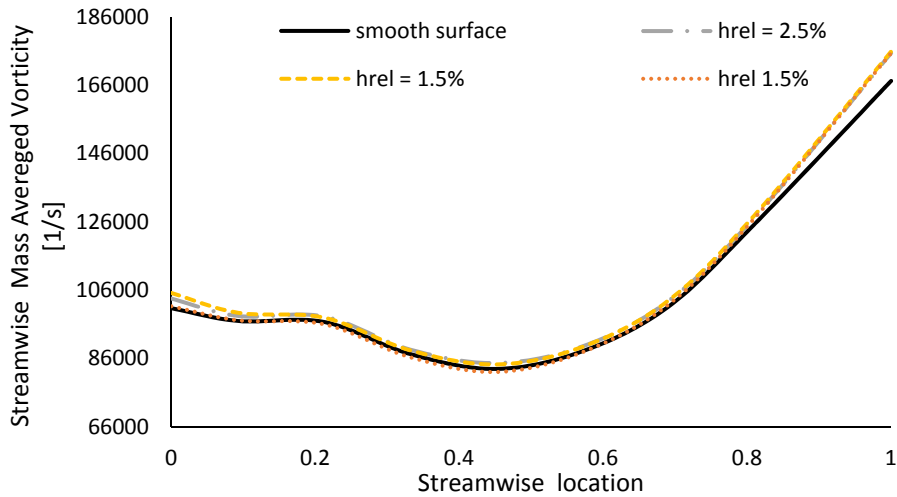
Figure 5.18: Mass averaged streamwise vorticity along rotor passage
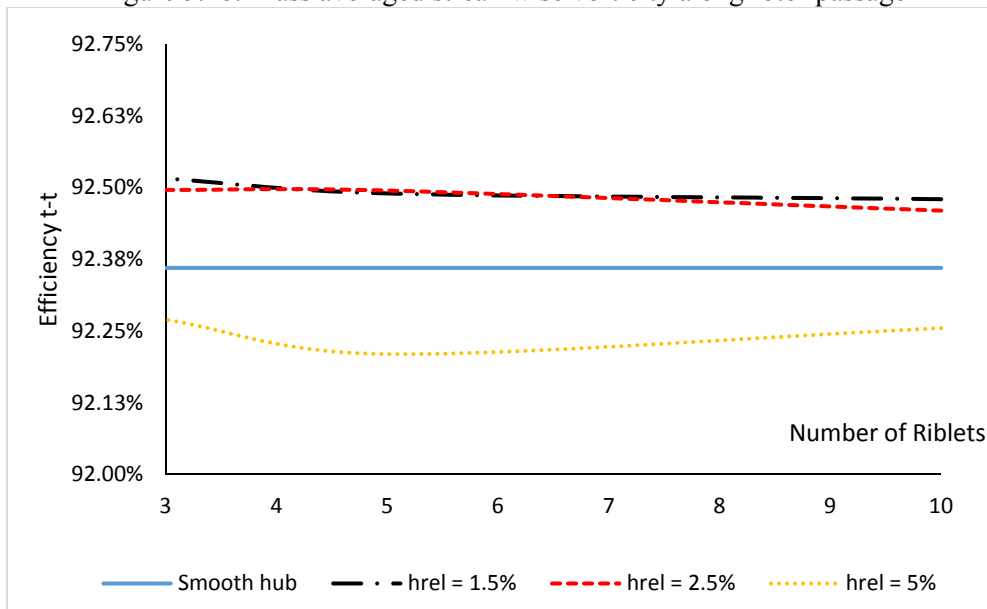
Figure 5.19: Turbine performance for different riblets geometry

Conclusion

In this chapter, the effects of engineered riblets on radial turbine performance were analysed numerically. It was found that riblets reduce the cross-stream motion of the low momentum fluids leading it to move from pressure to suction side of the rotor passage and separate the streamwise vortex from interaction with hub surface. This entrains low speed fluid in the riblets valley which in turn reduces the momentum transfer in the boundary layer causing reduction in wall shear stress.

The spacing between riblets was found to be of secondary effect on their performance in drag reduction as the streamwise vortex occupies most of the passage length. Riblets height was found to be the main parameter affecting drag reduction, where the maximum drag reduction found to occur with riblets with h_{rel} = 2.5%. Introducing riblets to hub surface is beneficial for drag reduction while it increases the streamwise vorticity in the rotor passage and the maximum performance was achieved for the turbine with the shortest riblets (hrel = 1.5%).

.

Chapter 6

6. Turbine Testing

To validate the turbine design and the performance prediction method explained in chapter 3, the designed turbine was tested experimentally. This chapter presents the test rig layout, MGT arrangement, instrumentation and the discussion of interpretation of the test results.

6.1 MGT Arrangement

The design of large gas turbines is a mature process which was developed through the second half of the last century. Meanwhile, designing a micro gas turbine is still a challenging process, where the key issues related to downsizing the gas turbine are:

- Low performance for the turbomachinery components
- High rotational speeds
- High rate of thermal energy transferred from the turbine side
- Cooling requirements for the High Speed Generator (HSG) and the bearings
- Rotor dynamic stability
- Sealing the various components of the MGT

Small size radial turbomachines have lower performance than large size machines, the reasons behind this discrepancy were addresses by Rodgers [5] as follow:

- Reynolds number effect:

  Hiett and Johnston [48] tested different turbines with range of Reynolds numbers, they found that the efficiency decreases with Reynolds number. And the relation between the efficiency and Reynolds number can be written as:

$$\eta_{tt} = 1 - \frac{1}{Re^{0.16}} \qquad (6.1)$$

- Tip clearance effects and manufacturing tolerances:

  Ideally rotors should not have a tip gap, however it is not possible to have a shrouded rotor because of the high stress on the wheel. For large rotors, a tip gaps of 1.7% of blade span height can be achieved [96], while these values are not achievable for small rotors because of the high cost and machining complexity. During the design stage of the turbine and the compressor housing, a tip clearance of 3% of span was considered, however during MGT assembly the rotor was rubbing the shroud, therefore the tip gap was increased to 7%. As explained in chapter two, 1% increase in the tip gap could lead to 1.6% drop in total efficiency of the turbine.

- Limited turbine inlet temperature:

  For small machines the turbine inlet temperature is not only limited by the rotor material but also by the amount of cooling needed for the bearings and the HSG and the recuperator material for a recuperated cycle.

Therefore, the design of the MGT has to cope with all of these issues to produce an efficient, reliable and economically viable machine. Figure 6.1 shows a cutaway of the designed MGT for OMSoP project. The MGT assembly design was a team work of three PhD students and a Post-doctoral researcher. The author contributed toward the

aerodynamic and the mechanical design of the turbomachinery components, MGT housing, sealing and cooling system design.

Different shaft-bearing arrangements were studied by an OMSoP team member and the results were published in [97]. Placing the HSG between the turbine and compressor penalises the energy required for cooling the bearings and the stator to achieve a rotor dynamic stable shaft over the wide operating range. Three high precision ball bearings were used, one bearing at the turbine side and two at the compressor side arranged in a tandem way which increases the radial and axial loading of the bearings.

The thermal expansion of the shaft is expected to reduce the axial preload of the bearings; therefore, a single turn wavy spring was added to the compressor side bearings to avoid the premature failure of the bearings. For the turbine side, the bearing holder was used to load the bearing. The bearings were cooled and lubricated using oil recirculation method which normally used for high temperature and high speed operation. In this method, the oil is injected through holes in the outer race of the bearing and then collected in a separate oil tank to settle and drop its temperature before it is recirculated in the system again. To cool the back side of the turbine, cooling oil was recirculated through a passage at the back plate of the turbine housing. To track the sun, the solar dish has to rotate about its axis and to tilt up and down from the horizontal axis, therefore the MGT is expected to run at different tilting angles. To collect the lubrication and cooling oil at different tilting angles, a cartridge was added at the bottom of the HSG.

The oil system design, the MGT assembly and the high speed balancing for the shaft, the mechanical design of the seals and the components around the high speed alternator and connecting the MGT to the electric drive was done by Dynamic Boosting Systems (DBS) Ltd.
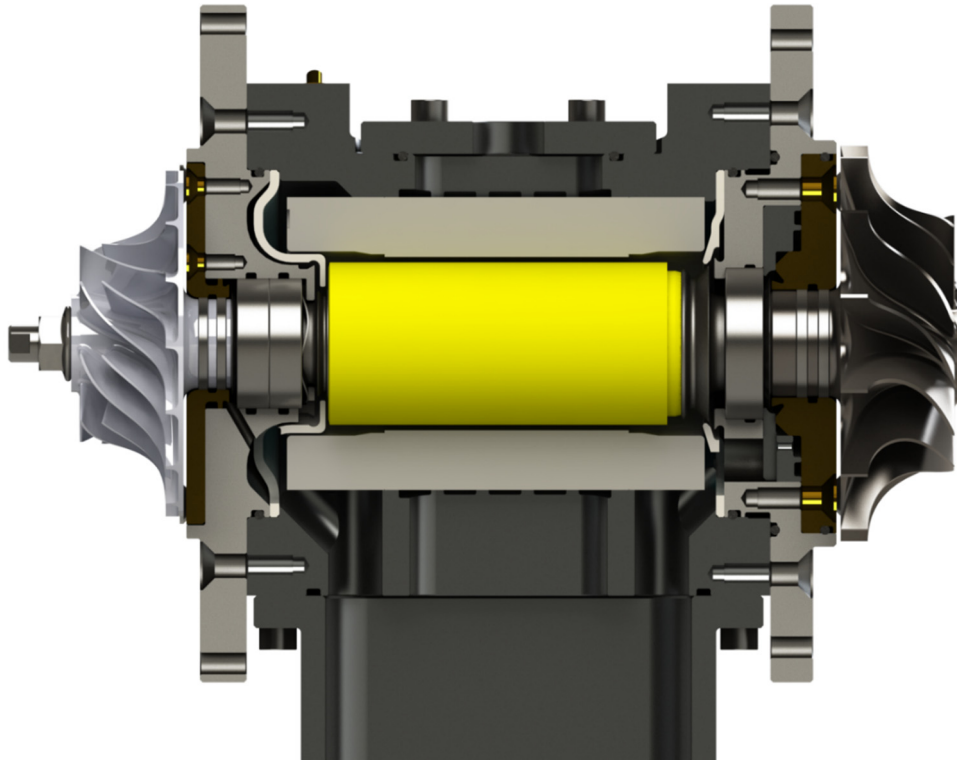
Figure 6.1: MGT configuration

Piston ring seals were used to seal both turbine and compressor ends, where the large

resistance within the small gap between the ring and the bore limits the leakage flow to or

from the compressor and the turbine. The main disadvantages of this type of seals are:

higher mechanical losses and low life expectancy. During the start-up of the MGT, the

shaft is rotating at low speeds and the windage force is not enough to set the ring sleeve

into its position. This cause a bad rubbing between the sleeve and the shaft, which cause

friction losses and reduce its life. To eliminate the mechanical losses and to increase the

sealing life, labyrinth seals are usually used in such high speed applications. However,

they suffer from greater leakage percentage and they require larger space for effective

performance.

6.2 Test Rig

The gas turbine test rig layout is shown in figure 6.2. The turbine was tested using high

pressure air supplied by a high pressure screw compressor which is able to deliver 1.5

kg/s of air at 10 bar and temperature of 23 ºC. The high pressure air is then regulated using a pneumatic controlled pressure regulator. An electric heater is used to raise the temperature of air before entering the turbine volute to avoid frosting at the turbine discharge.

The turbine entry air pressure and flow rate were adjusted using a manually controlled pressure regulator that controls the main pressure regulator. The electric heater operates at three power modes 6, 12 and 18 kW therefore the temperature of the entry flow can be increased by increasing the power output of the heater. The generated power from the turbine was dissipated in the centrifugal compressor and the HSG. The compressor outlet was fully opened to dissipate the greatest amount of power. The Alternating Current (AC) generated from the HSG was rectified to Direct Current (DC) and dissipated in programmable DC load bank. The speed of the turbine was controlled by changing the voltage across the resistive load.

6.3 Measurement and Instrumentation

The main objective of the turbine test is to characterise the turbine performance over a range of pressure ratios and flow rates. For this purpose, the flow temperature and pressure at turbine entry and discharge, the mass flow rate and the turbine speed are needed. This section discusses each measurement and the instruments used in the test.

6.3.1 Temperature Measurement

The maximum flow temperature that can be achieved out of the electric heater is 250 ºC, therefore all the temperature measurements were taken using T-type thermocouples. This type offers the highest accuracy among the common thermocouple and its response time is small. The accuracy of the thermocouples used in the test is ±1 ºC.
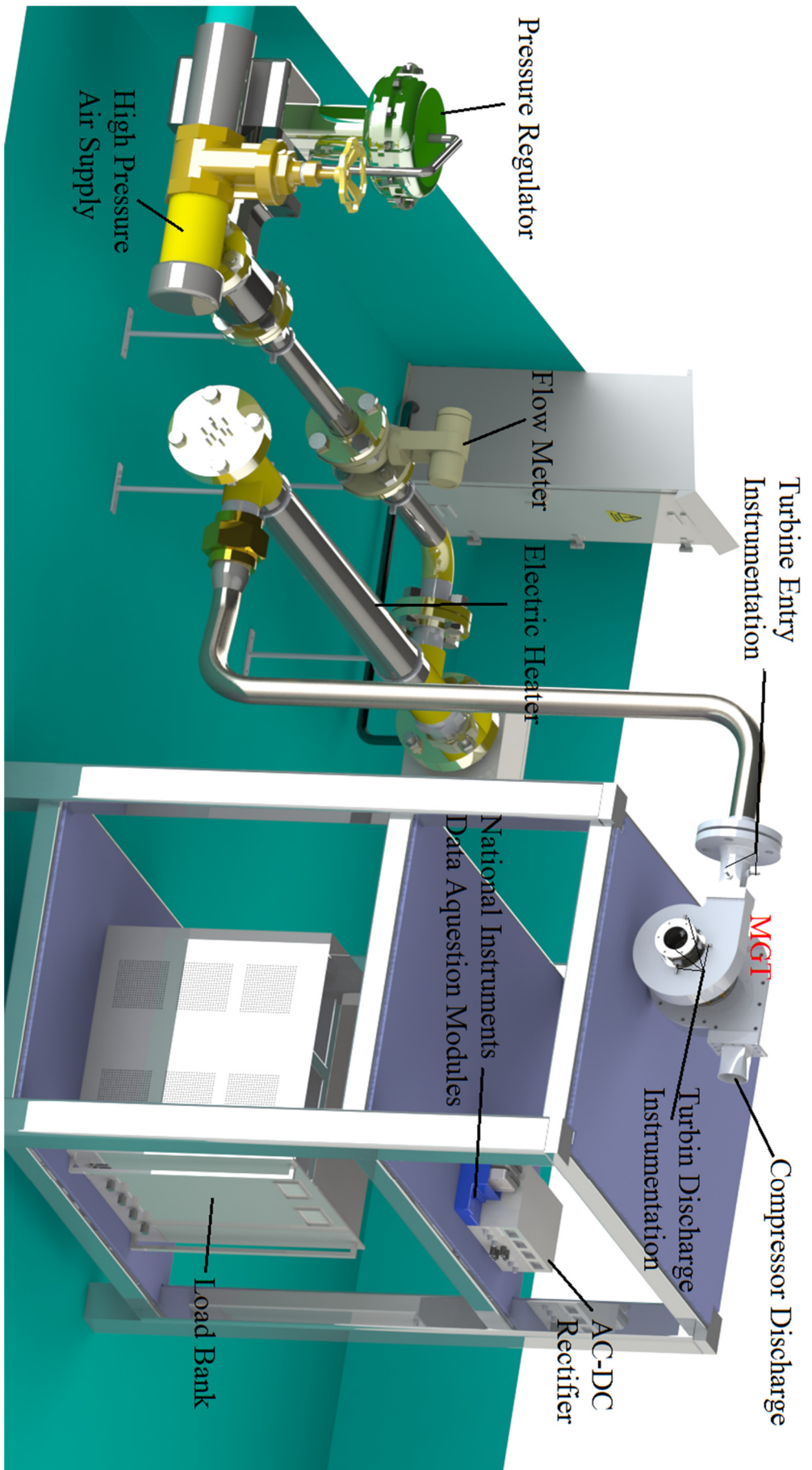
Figure 6.2: MGT test rig

143

The room temperature was measured using a bare wire thermocouple positioned close to the MGT. The air temperature after the flowmeter and at the turbine inlet and exit were measured using total temperature probes located approximately at the centre of the pipes. At the turbine exit the air temperature varies along the span as the temperature is inversely proportional with the radius, therefore the air temperature was calculated as the average value of the reading of three probes distributed along the span as shown in figure 6.3.

All the measurements were logged to a computer through a National Instruments (NI) 9211 Data Acquisition (DAQ) module. This module has four channels and an integrated circuit for cold junction compensation. This module has a high accuracy in reading the temperature (± 0.02 ℃) when it operates at the room temperature (23 ℃).
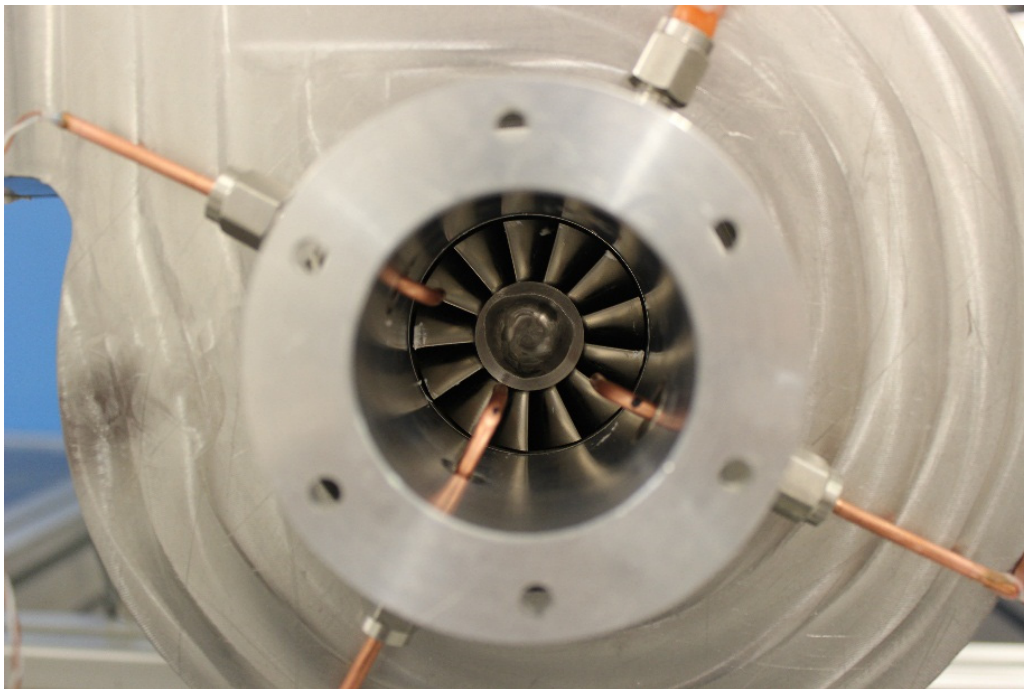
Figure 6.3: Thermocouples arrangement around at the turbine discharge

Controlling the data logging operation through the DAQ was done using the commercial software (LabVIEW) from NI. This software uses the graphical programming language to manipulate, save and monitor the data read by the DAQ. All the calibration data for the

instruments used in the test was implemented in the software and the final reading was displayed to monitor the measurements during the test. The test interface was designed to give the experimentalist the flexibility to save the measured data to an excel sheet at any desired point.

6.3.2 Pressure Measurement

During the test, the operating air pressure was measured at three stations: at the turbine inlet and exit and after the flow meter. The first two are needed to calculate the turbine efficiency, and the third one is to calculate the mass flow rate.

After the flow meter, the static pressure was measured using 3 mm tube attached to the wall of the pipe. At the turbine inlet, the total pressure was measured using a total pressure probe aligned with the pipe centre line. For both measurements, current output gauge pressure transducer with operating range from 0-3.4 bars. The accuracy of these transducers is ± 850 Pa. The static pressure at the turbine exit was measured using a 3mm tube located at the wall of the exit pipe, which is connected to a differential pressure transducer. This gauge measures the pressure difference between the turbine exit and the atmosphere with accuracy of ±24 Pa. The atmospheric pressure was measured using a standard barometer with resolution of ±250 Pa. The outputs of all the transducers were logged to the computer through NI 9203 DAQ. This module has eight channels to read 4-20 mA signals with accuracy of ±0.02 mA when operates at the room temperature. Like the thermocouples, the calibration data were inserted in LabVIEW to process and save the measurements.

6.3.3 Other Measurements

Apart from the temperature and pressure measurements, the turbine rotational speed and air mass flow rate are necessary to construct the turbine characteristics maps. Rosemount

8800d vortex flow meter was used to measure the air flow rate. The output signal of this device is 4-20 mA and its accuracy is $\pm$ 9.5e^{-4} m^3/s. like the pressure transducers; the output signal of the flow meter was logged to the computer using NI 9203 DAQ.

By measuring the frequency of the output signal of the two poles high speed generator the rotational speed was determined. The frequency was measured using (Tektronic TDS-2002) oscilloscope, with accuracy of $\pm$ 0.1 Hz.

During the test, the HSG stator and shaft bearings temperature and the MGT vibration level were monitored. Also, the output power of the high speed generator was measured and recorded for future referencing but will not be presented here.

6.4 Uncertainty analysis

Uncertainty analysis was carried out for the calculation of the turbine efficiency, corrected mass flow rate and expansion ratio which were used to plot the turbine characteristics. Due to the absence of the calibration tools; all the instrumentations used in the experiment were calibrated by the suppliers. Table 6.1, shows the maximum error expected in each measured quantity. The uncertainty analysis carried using the method recommended by Taylor [98], where both the uncertainty and the fractional uncertainty are required. For any measured quantity Z, it is presented in the form:

$$Z = z_{mgrd} + \delta z \qquad (6.1)$$

Where z_{mgrd} is the measured value of Z, and δz is the uncertainty in the measurement. Equation 6.1 also can be written as:

$$Z = z_{mgrd}\left[1 \mp \frac{\delta z}{|z_{mgrd}|}\right] \qquad (6.2)$$

In this equation, the ratio of the uncertainty to the measured quantity is called the fractional uncertainty.

146

Table 6-1: Expected uncertainty in the instrumentation devices

Quantity	Measuring tool	Uncertainty +/-
Volume flow rate	Rosemount 8800D	9.50E-04 m^3/s
Static pressure (flow meter exit)	Gauge pressure transducer	850 Pa
Total temperature (flow meter exit)	T-type thermocouple	1 ℃
Total temp (turbine inlet)	T-type thermocouple	1 ℃
Total pressure (turbine inlet)	Gauge pressure transducer	850 Pa
Total temp (turbine inlet)	T-type thermocouple	1 ℃
Static pressure (turbine exit)	Differential pressure transducer	251.15 Pa

The desired quantities of the test were not achieved using direct measurement, but rather derived using the basic mathematical models. Therefore, the propagation of uncertainty caused from adding/subtracting, multiplying/dividing multiple terms and raising terms to certain power is explained.

Addition and subtraction:

If the quantity A is the sum of the two measurements X and Y, where $X = x_{mgrd} + \delta x$ and $Y = y_{mgrd} + \delta y$, then the value of A is reported as:

$$A = \left[x_{mgrd} + y_{mgrd} \right] \mp \delta A \qquad (6.3)$$

The uncertainty δA can be calculated as the square root of the quadratic sum of the uncertainties of X and Y:

$$\delta A = \sqrt{\delta x^2 + \delta y^2} \qquad (6.4)$$

The same approach is used to quantify the uncertainty resulted from subtracting two measured values. Further, the uncertainty of adding/subtracting multiple items, can be calculated by taking the root of the squares of their uncertainties.

Multiplication and division:

If the quantity B is the result of multiplying the two measured values X and Y, then the value of B be reported as:

$$B = \left[x_{mgrd} \cdot y_{mgrd} \right] \mp \delta B \qquad (6.5)$$

The fractional uncertainty ($\delta B / |x_{mgrd} \cdot y_{mgrd}|$) can be calculated as the square root of

the quadratic sum of the fractional uncertainties of X and Y, this also holds for division

and multiple variables cases.

$$\frac{\delta B}{|x_{mgrd} \cdot y_{mgrd}|} = \sqrt{\left(\frac{\delta x}{x_{mgrd}} \right)^2 + \left(\frac{\delta y}{y_{mgrd}} \right)^2} \qquad (6.6)$$

Functions:

If the quantity C is a function of the measured value X then the uncertainty in the value of

C is:

$$\delta C = \left| \frac{dC}{dX} \right| \cdot \delta x \qquad (6.7)$$

Where dC/dX is the derivative of the function C with respect to X. Also, if C is a

function of multiple measured values X, ... ,Z, the uncertainty in C is given as:

$$\delta C = \sqrt{\left(\frac{dC}{dX} \cdot \delta x \right)^2 + \cdots + \left(\frac{dC}{dZ} \cdot \delta Z \right)^2} \qquad (6.8)$$

6.5 Turbine Test

The aim of this test was to run the turbine at the wide operating range, however this was

not possible due to the limitations on controlling the output power of the turbine. As

previously described the test was performed with a fully opened compressor to withdraw

the maximum mass flow, thus it can consume the largest amount of power. However, the

maximum power consumption is a function of impeller speed to the power of two, where

the CFD calculations show that the compressor maximum power consumption at 50,000

rpm is 400 W. Similarly, the power that can be consumed in the HSG is linearly related to

the rotor speed, where it is rated to generate 7 kW at 160,000 rpm. Thus at 50,000 rpm the

maximum power that can be dissipated is 2.1 kW. With this limited power dissipation, it was not possible to cover a broad range of operation conditions during the turbine testing. To characterise the turbine performance at low air temperature, the non-dimensional speed ($N/\sqrt{To1}$) was kept constant and pressure ratio was changed to generate data points on (efficiency Vs. Pressure ratio) and (corrected mass flow Vs. pressure ratio) graphs. The maximum speed achieved during the test was 50,000 RPM, therefore the intention was to generate the maximum number of point along the non-dimensional speed ratio [2747 $\mp$ 1.5%], to enable comparison with the CFD results for the hot gas conditions at 90,000 rpm. During the test, there was a high risk to overspeed the turbine, therefore, a solenoid actuator was fitted to the air regulator which can be activated to shut the supply air by an emergency push button.

To generate the desired data, the MGT was run for one minute at each point to ensure stable readings from the measuring devices.

6.6 Test Results

The efficiency of the turbine for the whole test range is presented in figure 6.4. On the same graph, the CFD predictions for the efficiency of the turbine operating at entry temperature of 1073 K and rotational speed of 90,000 rpm is plotted. The pressure ratios covered during the test range from 1.4 to 1.53. This was due the lack of control over the turbine load as discussed in section 6.5. During the test, the non-dimensional speed was kept constant while the air entry temperature and the rotational speed were changed to cover the broadest possible operating range.

Referring to figure 6.4, the turbine efficiency reached 82.5% for the turbine running conditions: pressure ratio of 1.46, air entry temperature of 332 K and non-dimensional speed of 2733. Jones [75] achieved an efficiency of 86% at the design point conditions,

where the turbine entry temperature is 1056 K and the pressure ratio is 3. However, the tip clearance for his turbine is 4% and 1% in the axial and radial directions respectively compared to 7% for the present turbine. As explained in section 6.1, one percent increment in the radial clearance leads to 1.6% reduction in the turbine efficiency, therefore such difference in efficiency is expected with this large tip gap. In addition, Reynolds number for the existing turbine is lower than Jones' turbine which is expected to lower the efficiency further.
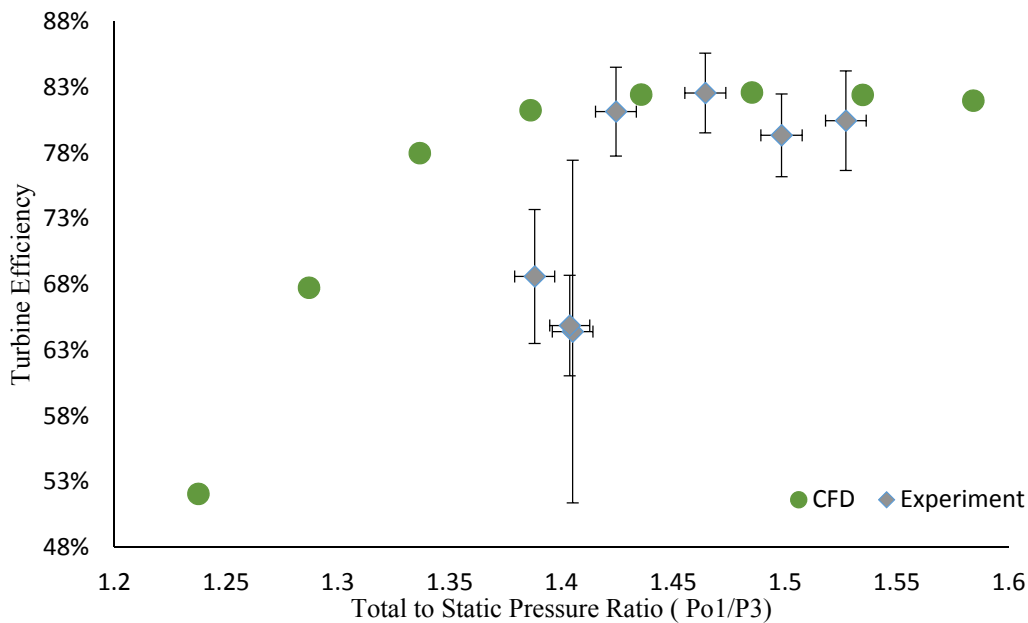
Figure 6.4: Turbine Efficiency versus Pressure Ratio

The CFD results match well with the experimental results for the pressure ratios between 1.42–1.53 bar, where all the data fall within the uncertainty range of the test points. For the lower pressure ratios, the CFD predictions deviate significantly from the test results. One of the probable reasons for this is the fact that turbine was run at low entry temperature for those points. With fixed uncertainty value for the T-type thermocouple, this would amplify the errors for the low temperature measurement. This can be seen clearly at the pressure ratio of 1.4, where the air temperature is 296 and 278 K at the

turbine inlet and exit respectively. The error in the efficiency for this point reached ±20%

due to the error in estimating the temperature especially the lower one.

To get confidence in the interpretation that the measurement uncertainty is the source of

the results mismatch, the efficiency of the turbine was plotted against the velocity ratio in

Figure 6.5. This ratio is derived by dividing the specific work output of the turbine by the

isentropic specific work, under the assumption of zero incidence angle at the leading edge

and zero swirl angle at the trailing edge. Operating the turbine at velocity ratio between

0.68-0.71 found to achieve the best performance [63].
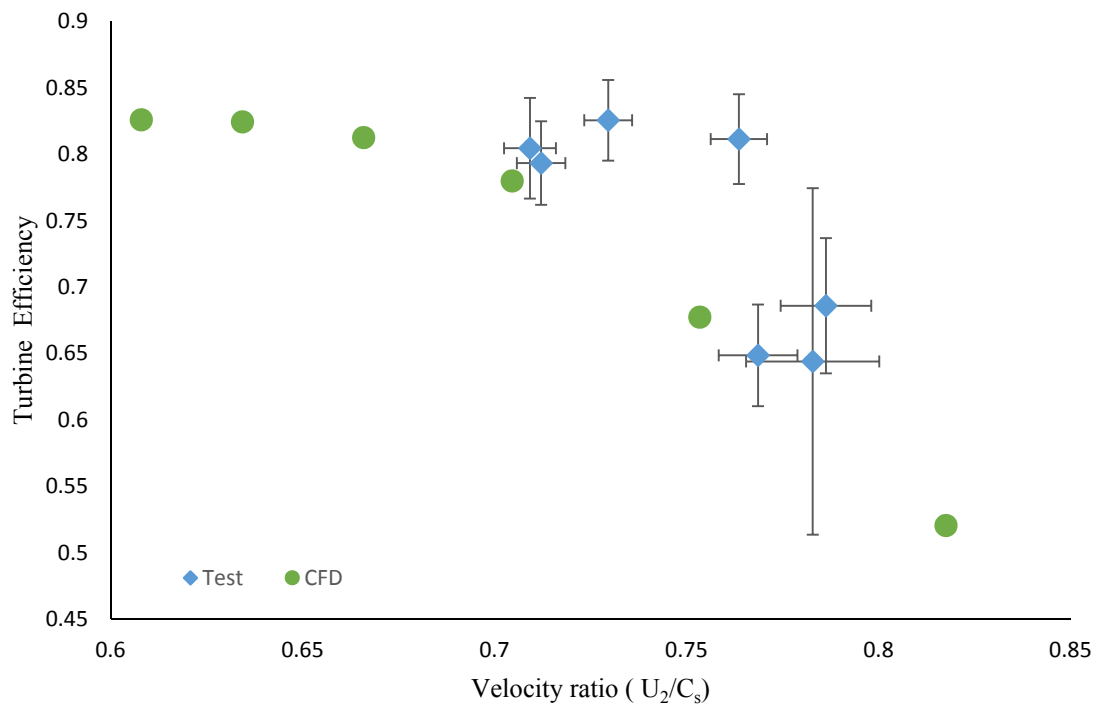
Figure 6.5: Turbine efficiency versus velocity ratio

Referring to figure 6.5, the CFD results shows that the best performance occurs at

velocity ratio of 0.61, while the highest efficiency achieved during the test was at a

velocity ratio of 0.73. This deviation indicates that the predicted velocity triangles and the

actual ones are not matching, which could be a result of the error in achieving the right

non-dimensional speed during the test. Also, the different boundary layer development

resulting from the surface roughness and the machining accuracy can cause such difference in the flow angles compared to the smooth wall CFD predictions.

All the mentioned reasons could lead to this difference, however more data covering wider operating range are needed to confirm these justifications.

Another important characteristic of the turbine is plotted in figure 6.6, where the machine swallowing capacity is plotted against the pressure ratio. In the figure the corrected mass flow parameter was used instead of mass flow to generalise the characteristics of the machine to be used with different operating conditions for the micro gas turbine. This plot is important to identify the turbine requirements at each operating condition and to match them with the compressor capacity. Unfortunately, the test range did not cover wide range of pressure ratio to identify the chocking limit of the turbine. The CFD predictions for the mass flow match well with the test data within the measurement uncertainty.
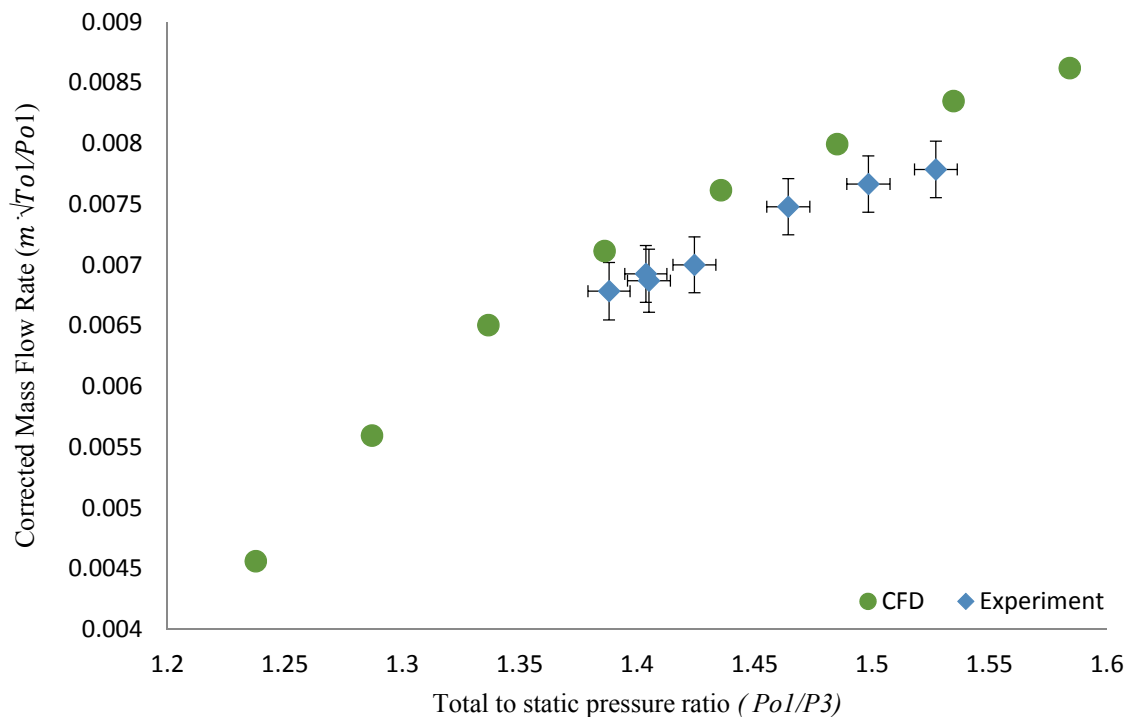
Figure 6.6: Corrected mass flow rate versus pressure ratio

Conclusions

As a result of this work, a test rig was built with ability to characterise the performance of the turbomachinery components of the MGT. A successful test was performed on a radial turbine, where the characteristic maps were generated for speed the line of 90,000 rpm. Further testing was needed to validate the compressor performance, however, the MGT was to move to ENEA for the solar system assembly and testing. The results show a good matching between the test data and the CFD predictions, which gives more confidence on the validity of the proposed design and performance prediction procedures.

Chapter 7

7. Conclusions and Recommendations for Future Work

7.1 Conclusions

The main objective of this research, was to explore methods to be applied to the turbomachinery components of a micro gas turbine to enhance their efficiency and the predictability of their performance over the whole operating range of the MGT, with specific application in concentrated solar power. To achieve this goal, the specific objectives were defined as:

- To understand the effects of implementing engineered features to the turbine rotor hub on the flow characteristics within the rotor passage. For this purpose, cusp shaped riblets were considered as they are practically achievable.

- To determine the best size and arrangement of the riblets which maximize the efficiency of the turbine.

- To develop an accurate and fast method to predict the performance of the radial turbines and the centrifugal compressors allowing for efficient design process.

- To contribute to the overall design and testing of the solar dish micro gas turbine system.

These objectives have been repeated here to comment on each one based on the work accomplished within this research to achieve it.

7.1.1 The Effect of riblets on the performance of radial turbines

Chapter five started with demonstrating the ability of the riblets at the end walls to alleviate the secondary flows within different types of turbomachinery ducts. Based on this review, it was found out that riblets can be used to limit the generation of secondary flows within the radial turbine rotor passages. Therefore, cusp shaped riblets were added to the rotor hub and their effect on the turbine aerodynamics were analysed numerically using CFD. It is understood from the literature that the main geometrical parameters that affect the riblets performance are the height of the riblets and the spacing between them. Therefore, riblets with different heights and spacing were introduced to the hub surface of the turbine rotor that was designed in chapter three. The turbine stage was then analysed at design point conditions. To generalise the results of this study, the height of the riblets was non-dimensionlised by referring it to the rotor inlet passage height, and the spacing between riblets were defined in terms of the angle in the radial-polar plane of the rotor.

It was found that riblets reduce the cross-stream motion of the low momentum fluids from the pressure side to the suction side of the rotor passage by forming a barrier in the face of the low energy flow. The secondary flow vortices generated from the interaction of the cross flow with the riblets work as a separator that reduce the interaction between the streamwise vortex and the hub surface. This entrains low speed fluid in the riblets valley which in turn reduces the momentum transfer in the boundary layer causing reduction in wall shear stress.

The spacing between riblets was found to be of secondary effect on their performance in drag reduction as the streamwise vortex occupies most of the passage length. Riblets height was found to be the main parameter affecting the drag reduction, where the maximum drag reduction found to occur with riblets with $h_{rel} = 2.5\%$. Introducing riblets to hub surface is beneficial for drag reduction, however it was found to increases the streamwise vorticity within the rotor passage. Therefore, the best turbine performance was achieved using the shortest riblet with a relative height of 1.5%.

7.1.2 Performance Prediction of Radial Turbomachines

To achieve this goal, a radial turbine and a centrifugal compressor had to be developed to apply the performance prediction method. Within the third chapter a methodology for radial turbine design was explained, and this method was successfully employed to generate a turbine that fits a 6 kWe MGT requirements. Similarly, in chapter four, a methodology for designing a centrifugal compressor was demonstrated and applied to generate a compressor that fits the same MGT.

Turbomachinery designers normally avoid adding the back-face clearance to the computational domain and treat the rotating wheels' walls as smooth surfaces to remove geometrical and numerical complexity of the numerical domain. In both chapters, a method to modify the CFD predictions of the compressor and turbine performance was proposed. In this method, the performance of each machine is firstly predicted using the CFD results. Thereafter the losses due to the back-face clearance and the surface roughness of the impeller are calculated using the loss correlations available in the open literature and the results are used to refine the CFD predictions. To validate this method, it was applied to a turbine geometry from the open literature, where the results obtained matched well with the experimental performance data for that machine.

7.1.3 MGT Test Rig Development

In the literature, test rig data for small size radial turbomachines are scarce. Also, the available data do not include the detailed geometry of these machines to be reproduced. Therefore, the intention was to develop a test rig to test the performance of the MGT components which can be used to validate the performance prediction method over a wide range of operating conditions. Also, it can be used to test the effectiveness of the riblets on improving the turbine performance on the actual machine. Chapter six contains a description for the main elements of the test rig and addresses the work done toward building this rig.

The test rig was operated by warm compressed air provided by the lab compressor, which can deliver 1.5 kg/s at 10 bar. A successful test was performed on a radial turbine, where the characteristic maps were generated for the 90,000 rpm speed line and a maximum pressure ratio of 1.5. The test was performed for low pressure ratio range because of the limited ability to dissipate the power that is generated from the turbine.

An uncertainty calculations were performed on the collected experimental data to enable a more realistic comparison between the test results and the performance predictions generated using the proposed model in chapter three. The results revealed a good matching between the test data and the CFD predictions, which gives more confidence on the validity of the proposed design and performance prediction procedures.

7.2 Recommendations for Future Work

During this research, some issues arose that require further work to be done in the future. This section will highlight the main issues and the future plan toward answering them.

7.2.1 The Effect of Riblets on the Performance of radial Turbomachines

From the results gained in chapter five, it appears that riblets have the ability to enhance the turbine performance at the design point conditions. This can justify the use of such features in turbines that run at the design point all the time. However, for a turbine that runs across a wide range of operating conditions further analysis is required. Operating the turbine at off-design results in changing the flow incidence angle which could lead to a flow separation within the passage. Therefore, the intention to extend this study to include the off-design conditions of the turbine which will help to generalise the results and make it applicable for all turbines application.

From the literature review it was learned that the experimental studies for the flow within turbine rotor are scarce, therefore, studying the effect of riblets on the flow aerodynamics is not an easy task. This raised the need for a simplified geometry that can mimic the flow within the rotor passage. A 90◦ duct is found to have the potential to replicate some of the flow behaviours within the rotor which is a result of the passage curvature.

Figure 7.1a shows a test rig that was built during the research period with cooperation with another PhD student at City University. This rig is operated using the shop air in the lab, where the air is regulated using a manual regulator valve. The air firstly passed through a settling chambers to remove any flow disturbances. The conditioned air then enters the test section through a bell mouth at the end of the settling chamber. In figure 7.1b the test section is shown, which was designed with a removable side wall that can be replaced with different ones with different riblets geometries. This section was built out of Perspex to enable an optical access to allow an optical access for the flow visualisation techniques.

The experimental tests will start by running the test rig at different conditions and a pressure difference measurements would be performed between the inlet and the outlet of

the curved section. The second stage of the test is to use Particle Image Velocimetry (PIV) techniques to visualise the flow at different sections along the curved section, which enables a more detailed analysis for the flow characteristics within the duct. The success in performing these tests will open the gate for more analysis to be done on employing riblets in other applications like reducing the tip clearance losses by limiting the motion of the scrapping flow motion at the shroud.

(a)

(b)
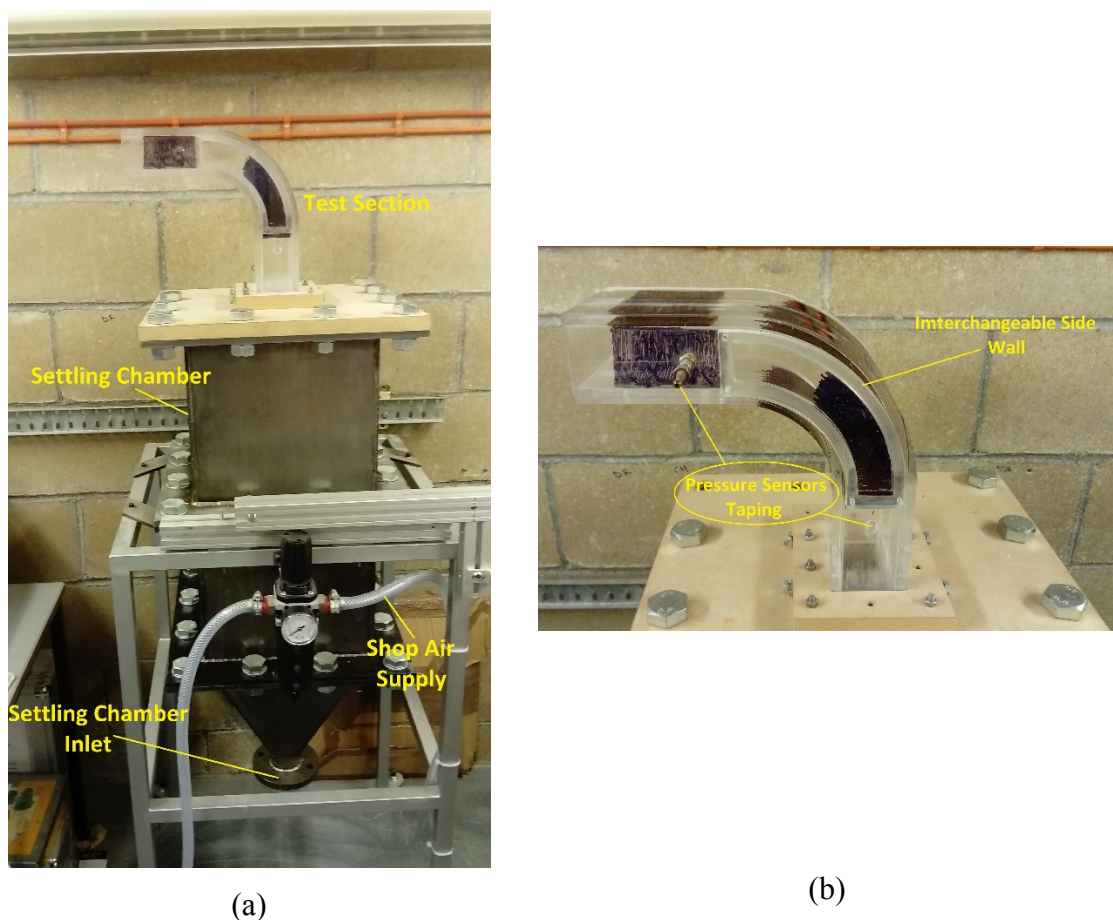
Figure 7.1: a- Test rig, b- Test section

7.2.2 Improving the MGT Test Rig

Despite the successful test of the turbine and achieving the performance data needed for validating the proposed performance prediction method, number of improvements are needed for this test rig.

- Design a combustor to fit the MGT in order to operate the MGT over a wider range to produce a full performance map which can be compared against predictions.

- Build the required instrumentation around the compressor to characterise its performance to validate the predictions cited in chapter four.

- Run the MGT at the design point, to allow for a validation for the thermal management method used in the MGT, sealing performance and to examine the rotor dynamics stability.

- Apply a proper insulation to the volute to prevent the heat transfer from the turbine to the environment. During the test, the volute was not insulated which will cause some of the heat to be transferred to the surrounding which increase the enthalpy drop measured at the exit of the turbine. This drop in the temperature of the air will affect the accuracy of calculating the efficiency of the turbine.

- At the exit of the turbine, a total temperature probes were used to measure the total gas temperature, however using those probes will encounter error called velocity error which can be described in equation 7.1.

$$E_{velocity} = T_t - T_j = (1 - \alpha)\frac{V^2}{2c_p} \qquad (7.1)$$

Where

T_t actual gas total temperature

T_j thermocouple reading

α recovery coefficient

V flow velocity

In real flows when the flow brought to rest near the thermocouple junction the kinetic energy of the flow cannot be recovered completely as a thermal energy as part of this

kinetic energy will be dissipated because of the fluid viscosity. The amount of this loss depends largely on the temperature probe geometry and the flow Prandtl number [99].

In the efficiency calculations the recovery coefficient was assumed to be 1, which will induce some degree of error. This assumption needs further investigation to determine the right value and apply it for the calculation of the turbine performance.

- At the exit of the turbine the temperature probes where aligned with the rotor axis, which is to some extent is right, however at the rotor exducer the flow is expected to have some degree of swirl which might affect the accuracy of the temperature measurements. In the future experiments the flow direction needs to be verified to set the probes in the right direction or pare wires can be used with the prober recovery factor calculations as they suffer from low recovery coefficient.

References

[1]   S. Project, "Solar Hybrid Gas Turbine Electric Power System," European Commission , Luxembourg, 2005.

[2]   S. Project, "Solar-Hybrid Power and Cogeneration Plants," European Commisssion, 2010.

[3]   S. Project, "Solar Up-scale Gas Turbine System," European Commission, 2014. [Online]. Available: http://cordis.europa.eu/project/rcn/90333_en.html. [Accessed 20 04 2017].

[4]   M. A. Boles, Thermodynamics: An Engineering Approach 6th edition, London: McGraw-Hill, 2007.

[5]   C. Rodgers, "5-25 kWe Micro-Gas turbines design aspects," in *ASME Turbo Expo*, Munich, 2000.

[6]   A. Whitefield and N. C. Baines, Design of Radial Turbomachines, John Wiley, 1990.

[7]   CERTS, "Behaviour of Capstone and Honeywell Micro turbine generators during Load changes," California, 2001.

[8]   C. Rodgers, "Microturbine Rotational Speed Selection," in *ASME TURBOEXPO*, San Antonio, 2013.

[9]   I.-R. E. Systems, "Environmental Technology Verification Report," 2003.

[10]   A. Ensola, "Technical report for micro turbine Turbic T100," Turbec Spa, 2006.

[11]   S. A. Shakariyants, M. Oostveen and W. P. Visser, "Development of a 3 kW micro turbine for CHP applications," *J. Eng. Gas Turbine Power,* vol. 133, p. 8, 2010.

[12]   J. Alzaili and N. I. Sayma, "Challenges in the Development of Micro Gas Turbines for Concentrated Solar Power Systems," in *8th International Gas Turbine Conference*, Brussels, Belgium, 2016.

[13]   A. Whitefield, "Preliminary design and performance prediction techniques for centrifugal compressors," *Journal of Power and Energy,* 1990.

[14]   H. W. Oh, E. S. Yoon and M. K. Chung, "An Optimum Set of Loss Models for Performance Pprediction of Centrifugal Compressors," *IMechE,* vol. 211, no. 4, pp. 331-338, 1997.

[15]   O. Conrad, K. Raif and M. Wessels, "The calculation of Performance Maps for Centrifugal Compressors with Vane Island Diffusers," in *ASME Gas Turbine Conference*, New Orelans, Luisiana, 1980.

[16]   J. E. Coppage, F. Dallenbach, H. B. Eichenberger, G. E. Hlavaka, E. M. Knoernschild and N. VanLee, "Study of Supersonic Radial Compressor for Refregeration and Pressurization Systems," WADC report, 1956.

[17]   W. Jansen, "A method for Calculating the Flow in a Centrifugal Impeller When Entropy Gradients are Present," in *Royal Society Conference on Internal Aerodynamics (Turbomachinery)*, 1967.

[18]   D. Japikse, Centrifugal Compressor Design, Concepts Eti, 1996.

[19]   H.-L. Wang, G. Xi, J.-Y. Li and M.-J. Yan, "Effect of the tip clearance variation on the performance of a centrifugal compressor with considering impeller deformation," *Journal of Power and Energy,* 2011.

[20]   L.-M. Gao, S.-J. Wang and G. XI, "Inf luence of Tip Clearance on the Flow Field and Aerodynamic Performance of the Centrifugal Impeller," *Chines Journal of Aeronautics,* vol. 15, 2002.

[21]   R. S. Abhari and S.-S. Hong, "Effect of tip clearance on impeller discharge flow and vaneless diffuser performance of a centrifugal compressor," *journal of Power and Energy,* 2012.

[22]   Y. Jung, M. Choi, S. Oh and J. Baek, "Effects of a nonuniform tip clearance profile on the performance and flow field in a centrifugal compressor," *International Journal of Rotating Machinery,* vol. 2012, p. 11, 2012.

[23]   A. Jaantinen and T. Turunen-Saaresti, "Influence of the different design parameters to the centrifugal tip clearance loss," *ASME Journal of Turbomachinery,* vol. 135, 2013.

[24]   Y.-S. Kang, H.-J. Emu and S.-H. Kang, "Tip clearance effect on through-flow and performance of a centrifugal compressor," *KSME International Journal ,* vol. 18, pp. 979-989, 2004.

[25]   J. W. Daily and R. E. Nece, "Chamber dimension effects on induced flow and friction resistance of enclosed rotating disc," *ASME Journal of Basic Engineering,* pp. 217-232, 1960.

[26] S. Anish and N. Sitaram, "Computational investigation of impeller–diffuser interaction in a centrifugal compressor with different types of diffusers," *IMechE Journal of Power and Energy,* vol. 223, pp. 167-178, 2009.

[27] J. D. Staintz, "One-Dimensional Compressible Flow in Vaneless Diffuser of Radial and Mixed Flow Centrifugal Compresors, Including Effects of Friction, Heat Transffer and Area Change," NACA TN 2610, California, 1952.

[28] R. C. Dean and Y. Senoo, "Rotating Wakes in Vaneless Diffuser," *ASME Journal of Basic Engineering,* vol. 82, pp. 563-574, 1960.

[29] J. P. Johnston and R. C. Dean, "Losses in Vaneless Diffuser in Centrifugal Compressors and Pumps," *ASME Journal of Engineering,* vol. 88, pp. 49-62, 1966.

[30] D. Eckardt, "Instantaneous measurements in the jet-wake discharge flow of a centrifugal compressor impeller," *ASME Journal of engineering power,* pp. 337-346, 1975.

[31] S. Kang and C. Hirsch, "Numerical simulation and theoretical analysis of the 3d viscous flow in centrifugal impellers," Vrije Universiteit Brussels, Brussles, 2001.

[32] H. Mustafa, D. Japikse, N. C. Baines and M. Zelesky, Axial and Radial Turbines, USA: Concepts NREC, 2003.

[33] S. L. Dixon and C. A. Hall, Fluid Mechanics and Thermodynamics of Turbomachinery, USA: Elsevier, 2010.

[34] R. H. Aungier, Turbine Aerodynamics: Axial-Flow and Radial Inflow Turbine Design and Analysis, New York: ASME Press, 2006.

[35] H. E. Rohlik, "Analytical determination of radial inflow turbine design geometry for maximum efficiency," NASA, Washington, 1968.

[36] C. A. Wasserbauer and A. J. Glassman, "Fortran program for predicting off-design performance of radial inflow turbines," NASA, 1975.

[37] C. Rodgers, "Advanced Radial Inflow Turbine Rotor Program Design and Dynamic Testing," NASA Lewis Research Center, San Diego, California, 1976.

[38] P. L. Meitner and A. J. Glassman, "Off-Design Performance Loss Model for Radial Turbines With Pivoting Variable-Area Stators," NASA Lewis Research Center, Cleveland, Ohio, 1980.

[39] S. M. Futral and C. A. Wasserbauer, "Off-Design Performance Prediction with Experimental Verification for a Radial-inflow Turbine," NASA Lewis Research Center, Cleveland, Ohio, 1965.

[40] A. Dadone and F. Pandolfi, "A Method for Evaluating the Off-Design Performance of A Radial Inflow Turbine and Comparison with Experiments," *int. j. mech. sci.,* pp. 241-252, 1969.

[41] N. C. Baines, "A meanline prediction method for radial turbine efficiency," in *IMECHE*, 1998.

[42] I. Huntsman, R. Dambach and H. P. Hodson, "An experimental study of tip clearance flow in a radial inflow turbine," in *ASME* , Stokholm, 1998.

[43] Q. Deng, J. Niu and Z. Feng, "Tip Leakage Flow in Radial Inflow Rotor of Microturbine with Varying Blade-Shroud Clearance," in *ASME TURBOEXPO*, Montreal, 2007.

[44] H. Simon, "Numerical simulation of the flow through the rotor of a radial inflow turbine," in *ASME Turbo Expo*, Orlando-Florida, 1997.

[45] Q. Deng, J. Niu and Z. Feng, "Study on the leakage flow characteristics of radial inflow turbines at rotor tip clearance," *Science in China Series E: Technological Sciences,* vol. 51, 2008.

[46] P. A. Jacob, C. Ventura, A. S. Ronalds and E. Sauret, "Preliminary design and performance estimation of radial inflowturbines: an automated approach," *ASME Journal of fluids engineering,* vol. 134, no. 3, 2012.

[47] C. Rodgers, "A Cycle Analysis Technique for Small Gas Turbines," in *Proc Inst Mech Eng*, San Diego, Calif., U.S.A, 1968.

[48] G. F. Hiett and I. H. Johnston, "Experiments concerning the aerodynamic performance of inward flow radial turbines," *IMechE,* vol. 178 , pp. 28-42, 1964.

[49] H. Tamaki, I. Morita , M. Unno and T. Kawakubo, "Numerical analysis on aerodynamic effects of impeller back cavity and disk shape of radial turbine," IHI, Japan, 2010.

[50] J. Dai, N. Ijichi, H. Tange, H. Shibata, H. Tamaki and S. Yamaguchi, "Comparison of internal flow field between experiment and computation in a radial turbine impeller," *JSME international Journal,* vol. 47, pp. 48-56, 2004.

[51] J. H. Yeo and N. C. Baines, "Pulsating flow behavior in a twin-entry vaneless radial inflow turbine," in *4th International Conference on Turbocharing and Turbochargers*, London, 1990.

[52] N. H. Wooley and A. P. Hantton, "Viscous flow in radial turbomachine flow passage," in *Institute of mechanical engineer*, 1973.

[53] S. T. Kitson, "Aerodynamic investigation of radial turbines using computational methods," VKI, Radial Turbines, 1992.

[54] I. Huntsman and H. P. Hodson, "Laminar flow rotor for a radial inflow turbine," *Journal of Propulsion and Power,* vol. 11, pp. 1170-1178, 1995.

[55] Q. Deng, L. Jun and Z. Feng, "Aerothermodynamic design and numerical simulation of radial inflow turbine impeller for a 100 kW microturbine," in *ASME Turbo Expo*, Nevada USA, 2005.

[56] E. Kalogeropoulos, Experimental Investigation of Roughness Effect on Centrifugal Compressor Performance, Sussex: University of Sussex, 2000.

[57] C. Rodgers, "The Characterstics of Radial Turbines for Small Gas Turbines," in *ASME Turbo Expo*, Georgia, USA, 2003.

[58] C. Rodgers, "Effects of Blade Number on the Efficiency of Centrifugal Compressor Impellers," in *ASME Turbo Expo*, San Diego, 2000.

[59] C. Osborne, P. Runstadler and W. Stacy , "Aerodynamic and Mechanical Design of 8:1 Pressure Ratio Centrifugal Compressor," NASA CR-134782, 1975.

[60] C. Rodgers , "The Performance of Centrifugal Compressor Diffuser," in *ASME GT* , New York, 1982.

[61] J. Runstadler and W. Peter, "Pressure Recovery Performance of Straight-Channel, Single-Plane Divergence Diffuser at High Mach Numbers," USAAVLABS, Virginia, 1969.

[62] A. H. Benisi, M. Mojaddam and M. R. Movahhedy, "Optimal Design of the Volute for a Turbocharger Radial Flow Compressor," *IMechE J Aerospace Enginnering,* vol. 229, p. 993–1002, 2015.

[63] H. Saravanamutto, G. Rodgers, H. Cohen and P. Straznicky, Gas Turbine Theory, Harlow, England: Pearson Education Limited, 2009.

[64] T. Verstraete, Z. Alsalhi and R. A. Braembussche, "Multidiciplinary Optimization of a Radial Compressor for Microgas Turbine Applications," *ASME journal of turbomachinery,* vol. 132, no. 3, p. 031004, 2010.

[65] B. W. Botha and A. Moolman, "Determining the Impact of the Different Losses on Centrifugal Compressor Design," *R & D Journal,* vol. 3, pp. 23-31, 2005.

[66] Q. Z. Hamdan and M. S. Ebaid, "Optimization Techniques for Designing an Inward Flow Radial Turbine Rotor," *IMechE,* vol. 218, pp. 655-667, 2004.

[67] M. J. Atkinson, Design of Efficient Radial Turbines for Low Power Applications, University of Sussex, 1998.

[68] I. Watanabe, I. Ariga and T. Mashimo, "Effects of dimensional parameters of impellers on performance characteristics of a radial-inflow turbine," *ASME Journal of engineering of power,* pp. 81-102, 1971.

[69] K. R. Pullen, N. C. Baines and S. H. Hill, "The Design and Evaluation of a High Pressure Ratio Radial Turbine," in *International Gas Turbine and Aeroengine Congress and Exhibition* , Cologne, Germany, 1992.

[70] A. J. McDonald and R. W. Fox, "An Experimental Investigation of Incompressible Flow Conical Diffuser," *Int. J. Mech. Sci.,* vol. 8, pp. 125-139, 1965.

[71] A. T. McDonald and R. W. Fox, "An Experimental Investigation of Incompresible Flow in Conical Diffusers," *Int. J. Mech. Sci.,* vol. 8, pp. 125-139, 1966.

[72] J. E. Bardina, P. G. Huang and T. J. Coakley, "Turbulence Modeling Validation, Testing, and Development," Ames Research Center, Moffett Field, California, 1997.

[73] C. E. Weeks, Evaluation of a Gamma Titanium Aluminide for Hypersonic Structural Applications, Georgia: Georgia Institute of Technology, 2005.

[74] J. Suhrmann, D. Peitsch, M. Gugau, T. Heuer and U. Tomm, "Validation and Development of Loss Models for Small Size Radial Turbines," in *ASME Turbo Expo*, Glasgow, UK, 2010.

[75] A. Jones, "Design and Test of a Small, High Pressure Ratio Radial Turbine," in *ASME int. gas turbine congress*, Netherlands, 1994.

[76] M. Walsh, "Riblets as a Viscous Drag Reduction Technique," *AAIA Journal,* vol. 21, pp. 485-486, 1983.

[77] K. Oehlert and J. Seume, "Exploratory Experiments on Machined Riblets on Compressor Blades," in *ASME Fluids Engineering Division*, Miami, 2006.

[78] C. Fang , C. Zhang and T. Ping, "An Experimental Investigation of Loss Reduction with Riblets on Cascade Blade Surface and Isolated Airfoils," in *ASME Gas Turbine Division*, New York, 1990.

[79] B. Bhushan and B. Dean, "The Effect of Riblets in Rectangular Duct Flow," *Applied Surface Science,* vol. 258, no. 8, pp. 3936-3947, 2012.

[80] Z. Q, X. Miao, L. Wang, J. H and H. Qi, "Application of Riblets on Turbine Blade End-wall Secondary Flow Control," *Journal of Propulsion and Power,* vol. 31, pp. 1578-1585, 2015.

[81] M. Govardhan, A. Rajender and J. Umang, "Effect of Streamwise Fences on Secondary Flows and Losses in a Two- dimensional Turbine Rotor Cascade," *Journal of Thermal Science,* vol. 15, p. 296—305, 2006.

[82] J. Zhong, J. Han, Y. Liu and F. Tian, "Numerical Simulation of Endwall Fence on the Secondary Flow in Compressor Cascade," in *ASME Turbo Expo*, Berlin, Germany, 2008.

[83] K. Kim, J. Cho, J. Kim and E. Jeong, "Controlling the Secondary Flows Near Endwall Boundary Layer Fences in a 90° Turning Duct Using Approximate Optimization Method," *Journal of Mechanical Science and Technology,* vol. 25, pp. 2025-2034, 2011.

[84] X. Miao, Z. Sun, Q. Zhang and C. Atkins, "End-wall Seconary Flow Control Using Engineering Residual Surface Structure," in *ASME Turbo Expo*, Seoul, 2016.

[85] D. Lei and L. Cao, "Effects of Residual Ribles of Impeller's Hub Surface on Aerodynamic Performance of Centrifugal Compressors," *Engineering Applications of Computational Fluid Mechanics,* vol. 9, pp. 99-113, 2005.

[86] A. Jones, "Design and Test of a Small, High Pressure Ratio Radial Turbine," in *ASME int. gas turbine congress*, Netherlands, 1994.

[87] Z. Sun, C. Guo, H. Chen and C. Tan, "Aerothermal Investigation of Backface Clearance Flow in Deeply Scalloped Radial Turbines," *Journal of Turbomachinery,* vol. 135, 2013.

[88] E. M. Greitzer, C. Tan and M. B. Graf, Ineternal Flow: Concepts and Applications, Cambrige University Press, 2007.

[89] M. Zangeneh-Kazemi, W. Dawes and W. R. Hawthorne, "Three Dimensional Flow in Radial-Inflow Turbines," in *Gas Turbine and Aeroengines Congress*, Amsterdam, 1988.

[90] V. Kola´rˇ, "Vortex Identification: New Requirements and Limitations," *International Journal of Heat and Fluid Flow,* no. 28, p. 638–652, 2007.

[91] H. Chun, O. El-Samni and H. Yoon, "Drag Reduction of Turbulent Flow over Thin Rectangular Riblets," *International Journal of Engineering Science,* vol. 45, pp. 436-454, 2007.

[92] S. J. Lee and S. H. Lee, "Flow Field Analysis of Turbulent Boundary Layer Over A Riblet Surface," *Experiments in Fluids Springer,* vol. 30, pp. 153-166, 2001.

[93] L. Duan, "Effects of Ribelts on Skin Friction in High-Speed Turbulent Boundary Layers," in *AIAA 50th* , Nashville, 2012.

[94] M. Walsh, "Turbulent Boundary Layer Drag Reduction Using Riblets," *AAIA,* 1980.

[95] D. W. Bechert, M. Bruse and W. Hage , "Experiments with Three-Dimensional Riblets as an Idealized Model of Shark Skin," *Experiments in Fluids,* vol. 28, pp. 403-412, 2000.

[96] P. Simonyi, R. Roelke, R. Stabe, B. Nowlin and D. DiCicco, "Aerodynamic Evaluation of Two Compact Radial Inflow Turbine Rotors," Lewis Research Center, Cleveland, 1995.

[97] A. Arroyo, M. Mclorn, A. Sayma, M. Fabian and M. White, "Rotor-Dynamics of Different Shaft Configurations for A 6 kW Micro Gas Turbine for Concentrated Solar Power," in *ASME Turbo Expo*, Seoul, 2016.

[98] J. R. Taylor, An Introduction to Error Analysis: The Study of Uncertainties in Physical Measurements, University Science Books, 1982.

[99] T. Arts, H. Boerrigter, M. Carbonaro, D. Olivari and G. Degrez, Measurement Techniques in Fluid Dynamics, Sint-Genesius-Rode, Belgium: von Karaman Institue, 1994.

[100] F. J. Wallace, "Theoretical assessment of the performance characteristics of inward radial flow turbines".," *IMechE,* pp. 931-942, 1963.

[101] A. Glassman and P. Meitner, "Off-Design Performance Loss Model for Radial Turbines With Pivoting Variable-Area Stators," NASA Technical Report, 1980.

[102] R. S. Benson, "A review of methods for assesing loss coefficients in radial gas turbines," *International Journal of Mechanical Science,* vol. 12, pp. 905-932, 1970.

[103] O. E. Balje, "Turbomachines- A Guide to Design, Select and Theory," John Wiley, New York, 1981.

[104] N. BAines and X. Qui, "Performance Predicition for High Pressure Ratio Radial Inflow Turbines," in *ASME Turbo Expo*, Montereal, 2007.

[105] M. White, The Design and Analysis of Radial Inflow Turbines Implemented within Low Temperature Organic Rankine Cycle, London: City, University of London, 2015.

[106] B. Bhushan and B. Dean, "the Effect of Riblets in Rectangular Duct Flow," *Applied Surface Science,* vol. 258, no. 8, pp. 3936-3947, 2012.

[107] Y. A. Çengel and M. A. Boles, Thermodynamics : an Engineering Approach, New York: McGraw-Hill Education, 2015.

[108] C. Rodgers, "Radial turbines- blade number and reaction effects," in *ASME Turbo Expo*, Munich, 2000.

[109] D. W. Bechert, M. Bruse and W. Hage, "Biological Surfaces and their Technological application Laboratory and Flight Experiments on drag Reduction and Separation Control," *AIAA,* 1997.
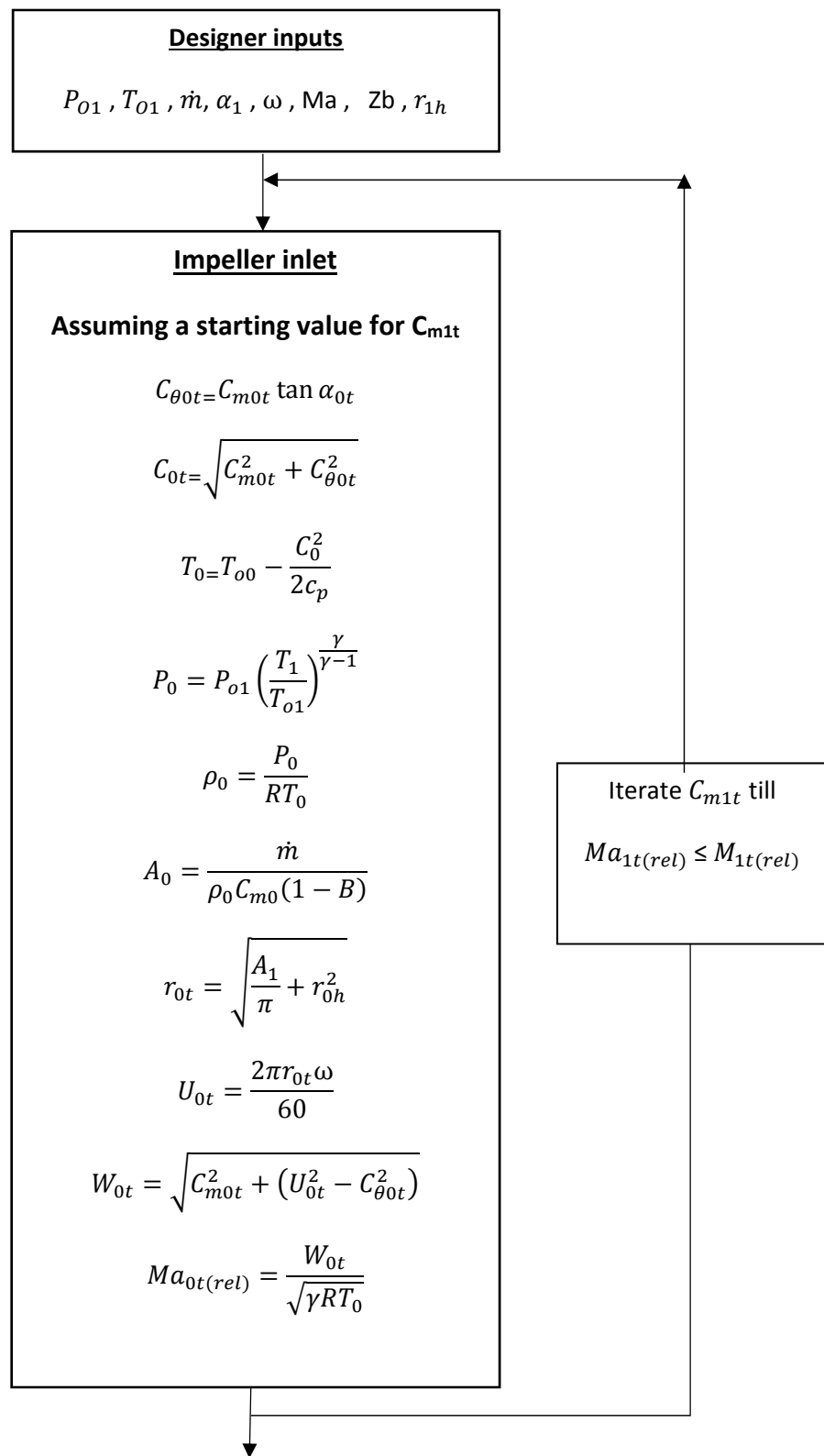
A. Appendix A Compressor Impeller Design Correlations

Figure A.1: Inducer design calculations

Impeller discharge calculation
Designer inputs: r_{3turb}, β_{sweep}, PR

$r_1 = r_{3turb}/1.15$

$P_{o1} = PR \times P_{00}$

$\Delta h_{0s} = \dfrac{\gamma R T_{00}}{\gamma - 1}\left(PR^{\frac{\gamma-1}{\gamma}} - 1\right)$

$\Delta h_0 = \dfrac{\Delta h_{0s}}{\eta_{tt}}$

$C_{\theta 1} = \dfrac{U_0 \times C_{\theta 0} + \Delta h_0}{U_1}$

$\sigma = 1 - \dfrac{\sqrt{\cos\beta_{sweep}}}{Z_r^{0.7}} = \dfrac{C_{\theta 1}}{C_{\theta 1(no-slip)}}$

$C_{m1} = \tan\beta_{sweep} \times (U_1 - C_{\theta 1(no-slip)})$

$C_1 = \sqrt{C_{\theta 1}{}^2 + C_{m1}{}^2}$

$W_1 = \sqrt{(U_1 - C_{\theta 1})^2 + C_{m1}^2}$

$\beta_1 = -\cos^{-1}\left(\dfrac{C_{m1}}{W_1}\right)$

$\alpha_1 = \tan^{-1}\left(\dfrac{C_{\theta 1}}{C_{m1}}\right)$

$T_{01} = T_{00} + \Delta h_0\left(\dfrac{1}{c_p}\right)$

$T_1 = T_{01} - \left(\dfrac{C_1{}^2}{2c_p}\right)$

$\dfrac{P_{01}}{P_1} = \left(\dfrac{T_{01}}{T_1}\right)^{\gamma/(\gamma-1)}$

$\rho_1 = \dfrac{P_1}{R T_1}$

$A_1 = \dfrac{\dot{m}}{\rho_1 C_{m1}}$

$b_1 = \dfrac{A_1}{\pi} D_1$

$Z = 0.6 \times r_1$

$Ma_1 = \dfrac{C_1}{\sqrt{\gamma R T_1}}$

$Ma_{1rel} = \dfrac{W_1}{\sqrt{\gamma R T_1}}$

Figure A.2: Inducer design calculations

B. Appendix B Turbine Rotor Design Correlations

Given
$T_{o1}, P_{o1}, \dot{m}, P_{turb}$
Designer Choice
$\psi, \phi, \omega, \zeta, \dfrac{r_{4h}}{r_3}, \alpha_4, \dfrac{Z}{r_3}$
Assumed value
η_{st}, η_{rotor}

(Rotor Inducer Calculations)

$$\Delta h_o = \frac{P_{turb}}{\dot{m}}$$

$$U_3 = \sqrt{\frac{\Delta h_o}{\psi}}$$

$$C_{m4rms} = U_3 \times \phi$$
$$C_{m3} = \zeta \times C_{m4rms}$$
$$C_{\theta 3} = U_3 \times \psi$$
$$\alpha_3 = \tan^{-1}\left(\frac{C_{\theta 3}}{C_{m3}}\right)$$
$$\beta_3 = \tan^{-1}\left(\frac{C_{\theta 3} - U_3}{C_{m3}}\right)$$
$$W_3 = \sqrt{C_3{}^2 + U_3{}^2 - 2.U_3 C_3 \cos(\tfrac{\pi}{2} - \alpha_3)}$$
$$T_{o3} = T_{o1}$$
$$T_3 = T_{o3} - \frac{C_3{}^2}{2c_p}$$

$$P_3 = P_{o1} \times \left(1 - \left[\frac{1 - \frac{T_3}{T_{o1}}}{\eta_{st}}\right]\right)^{\frac{\gamma}{\gamma-1}}$$

$$P_{o3} = P_3 \times \left(\frac{T_{o3}}{T_3}\right)^{\frac{\gamma}{\gamma-1}}$$

$$A_3 = \frac{\dot{m} \times R \times T_3}{P_3 \times C_{m3}}$$

$$r_{3t} = \left(\frac{U_3}{\omega}\right)$$

$$b_3 = \frac{A_3}{2 \times \pi \times r_3}$$

Iterate ψ until
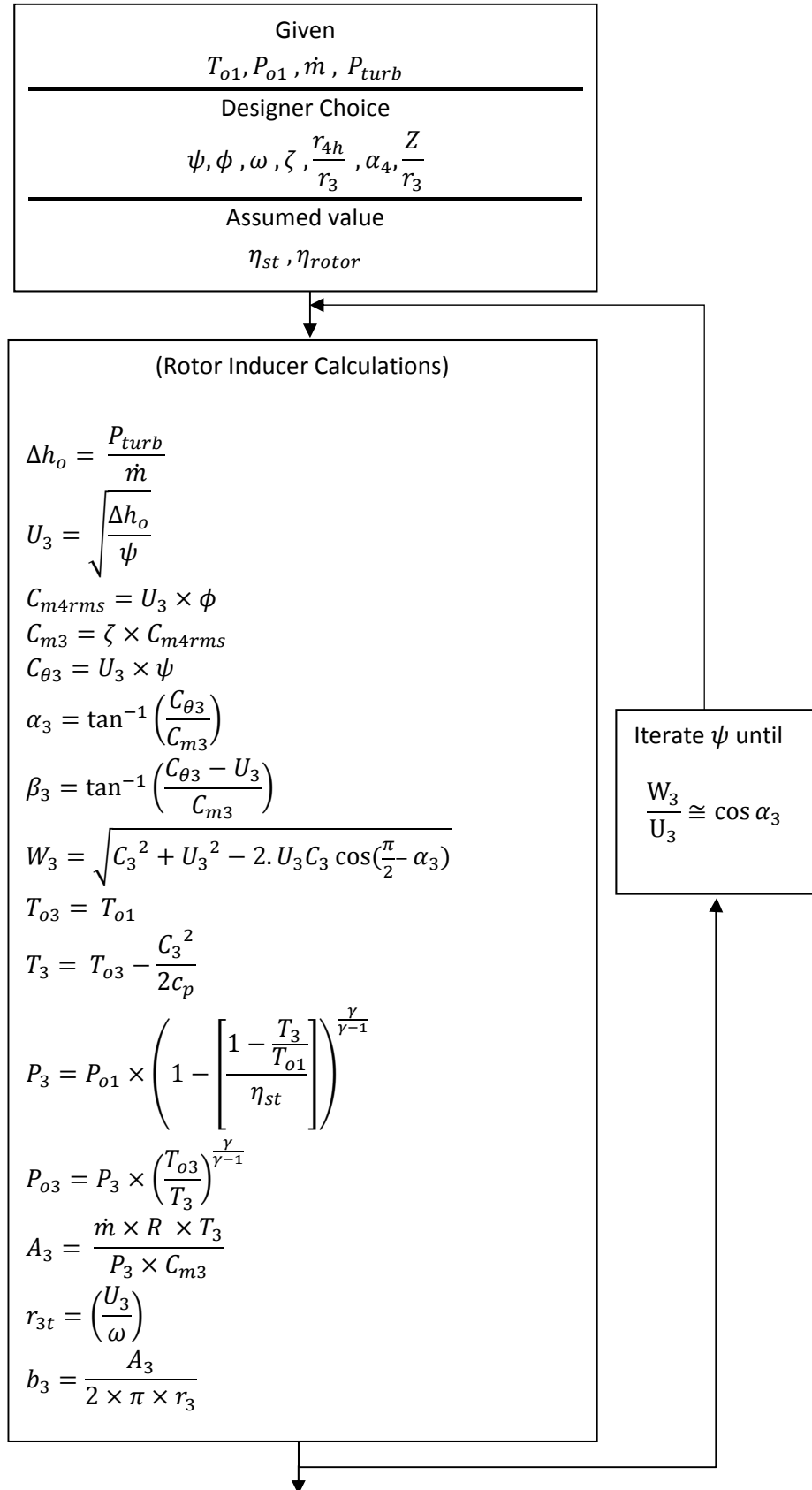
$$\frac{W_3}{U_3} \cong \cos \alpha_3$$

Figure B.1: Rotor inducer calculations

(Rotor Exducer Calculations)

$$T_{o4} = T_{o1} - \frac{\Delta h_o}{c_p}$$

$$T_4 = T_{o4} - \frac{C_4{}^2}{2c_p}$$

$$P_4 = P_{o1} \times \left(1 - \left[\frac{1 - \frac{T_{o4}}{T_{o1}}}{\eta_{rotor}} \right] \right)^{\frac{\gamma}{\gamma-1}}$$

$$P_{o4} = \frac{P_4}{\left(\frac{T_4}{T_{o4}} \right)^{\frac{\gamma}{\gamma-1}}}$$

$$A_4 = \frac{\dot{m} \times R \times T_4}{P_4 \times C_{m4}}$$

$$\rho_4 = \frac{P_4}{R \times T_4}$$

$$r_{4h} = \frac{r_{4h}}{r_3} \times r_3$$

$$r_{4t} = \sqrt{\frac{\left(A_4 + \frac{r_{4h}{}^2}{\pi} \right)}{\pi}}$$

$$r_{4rms} = \sqrt{\frac{r_{4t}{}^2 + r_{4h}{}^2}{2}}$$

$$U_{4rms} = r_{4rms} \times \omega$$

$$W_{4rms} = \sqrt[2]{C_{4rms}{}^2 + U_{4rms}{}^2}$$

$$\beta_{4rms} = \tan^{-1}\left(\frac{U_{4rms}}{C_{m4rms}} \right)$$

$$N_b = \frac{\pi}{30}(110 - \alpha_3)\tan(\alpha_3)$$

$$Z = \frac{Z}{r_{t3}} \times r_3$$

Figure B.2: Rotor exducer calculations